

AD _____

Award Number: W81XWH-11-1-0251

TITLE: Characterization of an E3 Ubiquitin Ligase that Degrades Neurofibromin in Vitro and Vivo

PRINCIPAL INVESTIGATOR: Dr. Yuan Zhu

CONTRACTING ORGANIZATION: The University of Michigan
Ann Arbor, MI 48109

REPORT DATE: April 2012

TYPE OF REPORT: Annual

PREPARED FOR: U.S. Army Medical Research and Materiel Command
Fort Detrick, Maryland 21702-5012

DISTRIBUTION STATEMENT: Approved for public release; distribution unlimited

The views, opinions and/or findings contained in this report are those of the author(s) and should not be construed as an official Department of the Army position, policy or decision unless so designated by other documentation.

REPORT DOCUMENTATION PAGE

*Form Approved
OMB No. 0704-0188*

Public reporting burden for this collection of information is estimated to average 1 hour per response, including the time for reviewing instructions, searching existing data sources, gathering and maintaining the data needed, and completing and reviewing this collection of information. Send comments regarding this burden estimate or any other aspect of this collection of information, including suggestions for reducing this burden to Department of Defense, Washington Headquarters Services, Directorate for Information Operations and Reports (0704-0188), 1215 Jefferson Davis Highway, Suite 1204, Arlington, VA 22202-4302. Respondents should be aware that notwithstanding any other provision of law, no person shall be subject to any penalty for failing to comply with a collection of information if it does not display a currently valid OMB control number. **PLEASE DO NOT RETURN YOUR FORM TO THE ABOVE ADDRESS.**

1. REPORT DATE (DD-MM-YYYY) 01-04-2012			2. REPORT TYPE Annual		3. DATES COVERED (From - To) 1 APR 2011 - 31 MAR 2012	
4. TITLE AND SUBTITLE Characterization of an E3 Ubiquitin Ligase that Degrades Neurofibromin in Vitro and Vivo			5a. CONTRACT NUMBER			
			5b. GRANT NUMBER W81XWH-11-1-0251			
			5c. PROGRAM ELEMENT NUMBER			
6. AUTHOR(S) Dr. Yuan Zhu E-Mail: yuanzhu@umich.edu			5d. PROJECT NUMBER			
			5e. TASK NUMBER			
			5f. WORK UNIT NUMBER			
7. PERFORMING ORGANIZATION NAME(S) AND ADDRESS(ES) The University of Michigan Ann Arbor, MI 48109			8. PERFORMING ORGANIZATION REPORT NUMBER			
9. SPONSORING / MONITORING AGENCY NAME(S) AND ADDRESS(ES) U.S. Army Medical Research and Materiel Command Fort Detrick, Maryland 21702-5012			10. SPONSOR/MONITOR'S ACRONYM(S)			
			11. SPONSOR/MONITOR'S REPORT NUMBER(S)			
12. DISTRIBUTION / AVAILABILITY STATEMENT Approved for Public Release; Distribution Unlimited						
13. SUPPLEMENTARY NOTES						
14. ABSTRACT Neurofibromatosis type 1 (NF1) patients are predisposed to various clinical complications, including benign and malignant tumors in both the peripheral nervous system and central nervous system. Furthermore, Nf1 patients are at high risks for non-tumor related symptoms such as neurocognitive and motor deficits, structural brain defects and bone abnormalities. The proposed studies attempt to provide important insights into one of the critical questions in the field of NF1 – molecular mechanisms regulating neurofibromin degradation. The objectives of this proposal are to utilize a newly established mouse model to (1) elucidate a positive feedback loop in the FBXW7/NF1/ERK axis in vivo and to (2) seek novel therapeutic strategies for NF1 haploinsufficient lesions various clinical manifestations. To test this model, we propose two hypotheses: (1) Neurofibromin is an SCFFbxw7 substrate in vivo and (2) a high level of Erk activation is a specific context contributing to Nf1 haploinsufficient diseases. We propose the following two specific aims to test these hypotheses.						
15. SUBJECT TERMS neurofibromin, ubiquitin, SCF ligase, cognitive dysfunction, Fbxw7, neural stem cells, radial glial cells, intermediate progenitor cells, cerebral cortex, deep- and upper-layer neurons						
16. SECURITY CLASSIFICATION OF:			17. LIMITATION OF ABSTRACT UU	18. NUMBER OF PAGES 93	19a. NAME OF RESPONSIBLE PERSON USAMRMC	
a. REPORT U	b. ABSTRACT U	c. THIS PAGE U			19b. TELEPHONE NUMBER (include area code)	

Table of Contents

	<u>Page</u>
Introduction.....	1
Body.....	2-9
Key Research Accomplishment.....	10
Reportable Outcomes.....	10-11
Appendices.....	

Introduction

Neurofibromatosis type 1 (NF1) patients are predisposed to various clinical complications, including benign and malignant tumors in both the peripheral nervous system and central nervous system. Furthermore, Nf1 patients are at high risks for non-

tumor related symptoms such as neurocognitive and motor deficits, structural brain defects and bone abnormalities. The proposed studies attempt to provide important insights into one of the critical questions in the field of NF1 – molecular mechanisms regulating neurofibromin degradation. The objectives of this proposal are to utilize a newly established mouse model to (1) elucidate a positive feedback loop in the FBXW7/NF1/ERK axis *in vivo* and to (2) seek novel therapeutic strategies for NF1 haploinsufficient lesions various clinical manifestations. **To test this model, we propose two hypotheses: (1) Neurofibromin is an SCF^{Fbxw7} substrate *in vivo* and (2) a high level of Erk activation is a specific context contributing to Nf1 haploinsufficient diseases. We propose the following two specific aims to test these hypotheses.**

Body

Task 1. To determine whether Fbxw7 controls neurofibromin protein levels *in vivo*

Task 1-1: To determine the role of Fbxw7 in neural stem cell function during development

To investigate the role of *Fbxw7* in neural stem cells during development, we targeted *Fbxw7* conditional mutation in radial glia cells (RGCs) by employing a Cre transgenic strain controlled by human GFAP promoter (hGFAP-cre), which is activated in >95% of RGCs from embryonic day 13.5 (E13.5). For simplicity, the resultant *Fbxw7* mutant mice with the genotype of hGFAP-cre+; *Fbxw7*^{flox/flox} were hereafter referred to as *Fbxw7*^{-/-M}. Through analysis of this mouse model, we demonstrated that *Fbxw7* inactivation have a major impact in neural stem cells during development. We first identified that the *Fbxw7*^{-/-M} neocortex display a significantly decreased cortical thickness in rostral and caudal region (Figure 1A'). The cortical thickness roughly correlates with the number of cortical neurons. Therefore, we analyzed the cortical neurons in control and *Fbxw7*^{-/-M} neocortices.

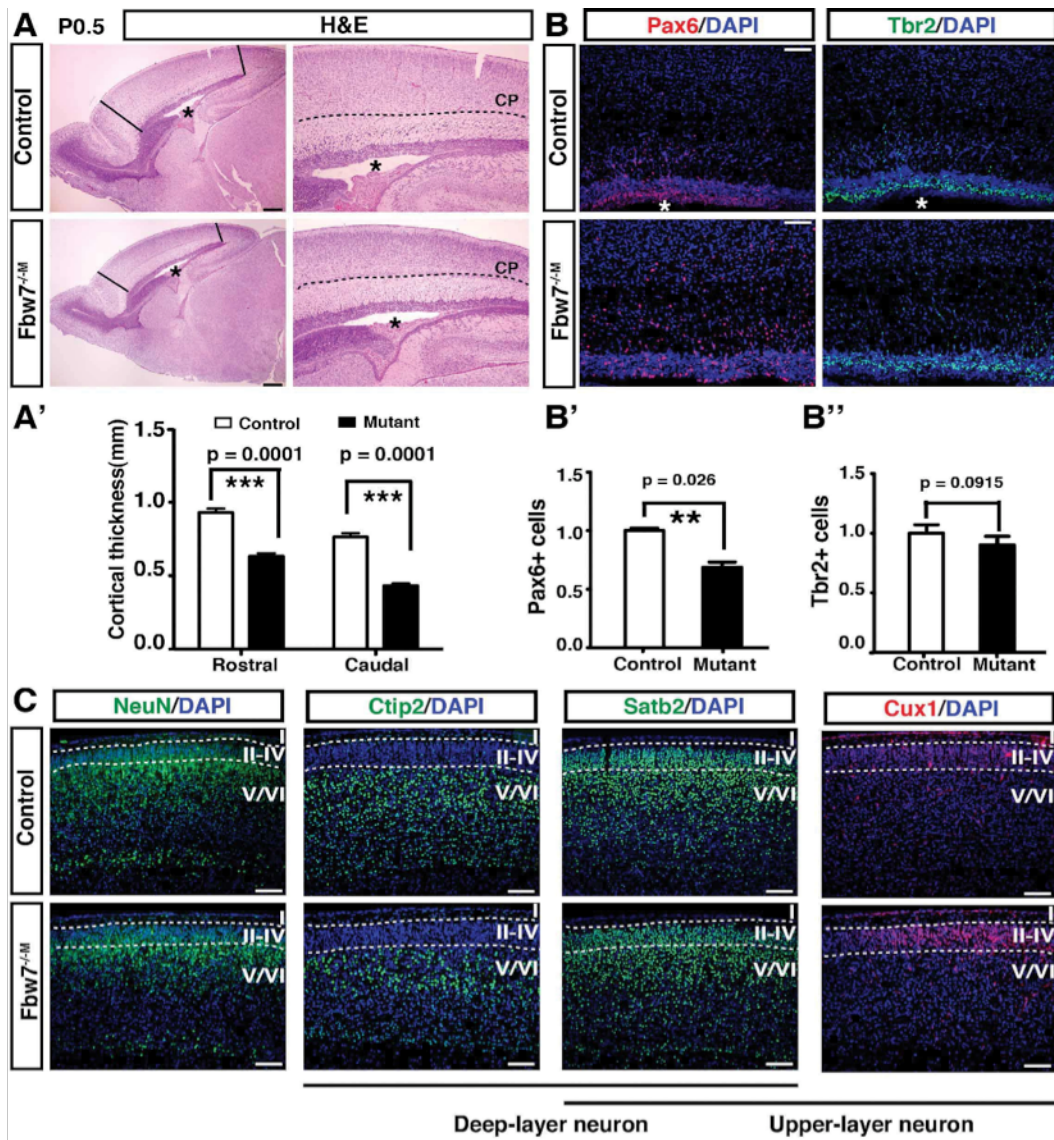


Figure 1. *Fbxw7* mutant cortex exhibited a reduction of VZ stem cells and deep-layer neurons at postnatal day 0.5 (P0.5)

(A and A') Sagittal sections of control and *Fbxw7*^{-/-M} brains at P0.5 were stained with hematoxylin & eosin (H&E) and quantified. Black solid lines in the rostral and caudal regions of the neocortex indicate the location where the thickness was measured. (B-B'') Immunostaining of Pax6 and Tbr2 were performed on control and *Fbxw7*^{-/-M} brain sections. The ratios of Pax6⁺ and Tbr2⁺ and cells in P0.5 neocortices were measured and shown as a relative change versus control. (C) NeuN and cortical layer-specific marker (Ctip2, Satb2, and Cux1) staining were performed on sections of control and *Fbxw7*^{-/-M} neocortices at P0.5. DAPI labels nuclei. n = 3 was used for per genotype. All quantification data are presented as mean ± SEM. Asterisk indicates the existence of statistical significance when mutants were compared with controls: ** p < 0.01. *, lateral ventricle; VZ, ventricular zone; SVZ, subventricular zone; CP, cortical plate; Scale bars: 50 μm

As revealed by NeuN staining, the total number of cortical neurons was visibly reduced in *Fbxw7*^{-/-M} neocortices (Figure 1C). As revealed by Ctip2⁺ and Satb2⁺, deep-layer neurons, which are derived from VZ stem cells in early to mid stages of cortical neurogenesis, were reduced in the *Fbxw7*^{-/-M} neocortex at P0.5. In contrast, Cux1⁺ and Satb2⁺ upper-layer neurons, which are derived from SVZ progenitor cells in mid to late stages of cortical neurogenesis, were not impaired by inactivation of *Fbxw7* (Figure 1C). Of note, Satb2 is expressed in both deep- and upper-layer neurons. To examine if alteration in stem cell pool contributes to the reduction in cortical neurons, we analyzed ventricular zone (VZ) and subventricular zone (SVZ) stem and progenitor cells at postnatal day 0.5 (P0.5). The *Fbxw7* mutant brain exhibited a significant reduction of VZ stem cells, revealed by Pax6 staining (Figure 1B, B'). However, the number of Tbr2⁺ SVZ progenitors in mutant brains was relatively unaffected (Figure 1B, B''). These results are consistent with the observation that RGC-derived deep-layer neurons are reduced, but SVZ-derived upper-layer neurons remain relatively normal in the *Fbxw7* mutant cortex (Figure 1B). Together, our observations demonstrate that inactivation of *Fbxw7* causes a reduction of deep-layer neurons during the embryonic cortical development and consequently leads to decreased cortical thickness.

To investigate whether the impact of *Fbxw7* inactivation in neural stem cells during neonatal and postnatal brain development, we analyzed whether *Fbxw7* inactivation impacts on proliferating cells at P0.5. We quantified the number of proliferating cells marked by Ki67 and identified that the number of Ki67⁺ cells was significantly reduced in the *Fbxw7*^{-/-M} neocortices compared to that of control (Figure 2A, A'' and A'''). However, the frequency of progenitor cells in S phase (mitotic index) was not significantly different between the control and mutant neocortices (Figure 2A'). These observations suggest that the loss of a stem or progenitor cell population(s), rather than a proliferation defect, contributes to the reduced proliferation observed in the *Fbxw7*^{-/-M} neocortices. More specifically, the number of Ki67⁺ cells in the VZ and intermediate zone (IZ) was significantly decreased but not in the SVZ of the *Fbxw7*^{-/-M} neocortex compared to that of control (Figure 2A''''). Consistent with this finding, the *Fbxw7*^{-/-M} neocortices at P0.5 showed a significant decrease the number of Pax6⁺ cells but not in

$Tbr2^+$ cells (Figure 1B' B''). Moreover, $Fbxw7^{-/-M}$ neocortices displayed a significant reduction in the Oligodendrocyte transcription factor 2 ($Olig2^+$) glia lineage cells (glia progenitor and oligodendrocytes), which are predominantly present in the IZ at P0.5. It is well established that after the completion of cortical neurogenesis in the cerebral cortex at E17.5, gliogenesis ensues and persists into postnatal stages. A greater reduction in the number of $Olig2^+$ cells was observed in the caudal region than rostral region of $Fbxw7^{-/-M}$ neocortices (Figure 2B, White boxed area). In contrast to reduced glial lineage cells, neuronal lineage cells marked by Distal less home box 2 (Dlx2) were increased in the rostral migratory stream (RMS) and anterior SVZ (aSVZ) in $Fbxw7^{-/-M}$ neocortices at P0.5 (Figure 2B). Consistently with this observation, the $Fbxw7^{-/-M}$ neocortices at P8 clearly displayed a significantly decreased number of $Olig2^+$ cells (arrowheads) in and concurrently increased number of Dlx2 $^+$ cells in the corpus callosum (CC) of the caudal region (Figure 2C, C'). These data suggest that inactivation of $Fbxw7$ increases the output of cells in neuronal lineage with concurrent reduction of cells in glial lineage in neonatal brains. We also compared astrogenesis between control and mutant cortices at P8 by performing GFAP immunostaining, but did not find an overt difference in the expression level. Strikingly, $Fbxw7$ inactivation increased the number of the ependymal cells as evidenced by GFAP (rabbit-polyclonal antibody) staining in the CC of the caudal region at P8 brain (Figure 2D, Insets). We also further confirmed that the lining of ependymal cells, demonstrated by S100 β staining, was not restricted to the lateral ventricle (LV) wall but elongated to the CC of caudal region in $Fbxw7^{-/-M}$ neocortices compared to control (Figure 2E and 3B, arrowheads). Moreover, Nf1 immunostaining demonstrated that a robust level of Nf1 was expressed in ependymal cells in CC of caudal region of $Fbxw7$ mutant brain compare to control (Figure 2F). These results indicate that inactivation of $Fbxw7$ leads to ectopic generation of ependymal cells and neural progenitor cells in CC of caudal region of the brain. Moreover, We observed that $Fbxw7^{-/-M}$ neocortices at P60 displayed enlarged LV and separation between the CC and hippocampus (Figure 3D). Therefore, we are examining whether this phenotypes caused by the ectopic expression of ependymal cells in $Fbxw7^{-/-M}$ neocortice. We also are currently investigating the molecular and cellular mechanisms underlying of these phenotypes in the $Fbxw7^{-/-M}$ neocortices during embryonic and postnatal brain

development. Taken together, Nf1 level regulated by *Fbxw7* is essential for proliferation and differentiation of neural stem cells during brain development (See task 2).

In summary, these results are most consistent with the model wherein loss of *Fbxw7* leads to accumulation of neurofibromin, which suppresses Ras/Erk signaling pathway in embryonic neural stem cells – RGCs. Consistent with this model, previous results showed that decreased Erk signaling suppresses RGC proliferation and consequently reduces RGC-mediated deep-layer neurogenesis, but not SVZ-mediated upper-layer neurogenesis. Together, these results provide strong evidence at the phenotypic level that *Fbxw7* loss leads to phenotypic consequences, which is consistent with accumulation of neurofibromin and suppression of Ras/Erk signaling pathway.

Future directions: (1) We will determine at the molecular level whether loss of *Fbxw7* leads to accumulation of neurofibromin in RGCs during embryonic stages. We have generated preliminary data showing that both total neurofibromin and phosphorylated neurofibromin were increased upon *Fbxw7* loss. This year, we will systematically determine accumulation of total and phosphorylated neurofibromin, and activation status of Ras/Erk/MAPK, PI3K/Akt and mammalian target of rapamycin complex1 (mTORC1) in *Fbxw7*-deficient RGCs. We will also try to establish immunohistochemical staining protocol to determine accumulation of neurofibromin in *Fbxw7*-deficient tissues *in situ*. (2) We will determine the mechanism by which *Fbxw7* inactivation leads to reduction in deep-layer neurons caused by altering cell cycle exit and/or increasing apoptosis of VZ stem cells at earlier developmental stages (E13.5, E15.5, E17.5). (3) We will continue to study the role of *Fbxw7*-regulation of neurofibromin in fate-specification of neural stem cells and empendymal cell differentiation.

Task 1-2: Whether mono and bi-allelic inactivation of Nf1 could rescue the brain abnormalities observed in the *Fbxw7* mutant brain.

After establishing that Nf1 level regulated by *Fbxw7* is essential for proliferation and differentiation of neural stem cells, we examined whether reduced or loss of Nf1 expression could rescue brain phenotypes observed in the *Fbxw7*^{-M} brain. We generated *Fbxw7/Nf1* double mutant mice by establishing the cross between hGFAP-cre+; *Fbxw7*^{flx/flx}; *Nf1*^{flx/+} and *Fbxw7*^{flx/flx}; *Nf1*^{flx/+} mice. We analyzed two *Fbxw7/Nf1* double mutant (DM1 & 2) strains, *Fbxw7*^{-/-}*Nf1*^{+/+DM1} and *Fbxw7*^{-/-}*Nf1*^{+/+DM2}. The life span of *Fbxw7*^{-/-}*Nf1*^{+/+DM2} mice was 25 days; however, *Fbxw7*^{-M} and *Fbxw7*^{-/-}*Nf1*^{+/+DM1} mice could live past one year. Our preliminary data suggest that partial or complete inactivation of Nf1 completely rescued the cortical thickness in *Fbxw7*^{-M} at P0.5 (Figure 3A and A'). Furthermore, *Fbxw7*^{-/-}*Nf1*^{+/+DM1} and *Fbxw7*^{-/-}*Nf1*^{+/+DM2} neocortices did not display abnormal ependymal cells and neuroblasts at P8 and P20 (Figure 3B, C). We are examining to investigate whether these two double mutants could rescue the abnormal ependymal cells and neuronal lineage cells generation in the caudal region of *Fbxw7*^{-M} mice using specific markers we used. At P60, *Fbxw7*^{-M} brain exhibited the enlarged LV and separation of between CC and hippocampus. Although we could not examine *Fbxw7*^{-/-}*Nf1*^{+/+DM2} brains at P60 due to lethality; however, *Fbxw7*^{-/-}*Nf1*^{+/+DM1} mice (3 out 5) completely rescued the abnormalities of *Fbxw7*^{-M} mice, which are enlarged LV and separation between CC and hippocampus (Figure 3D). Based on these data, reduction or ablation of *Nf1* in *Fbxw7* deficient brain rescues the brain abnormalities of *Fbxw7*^{-M} mice. We are also planning on investigating whether *Nf1* single mutant brains exhibit a lack of the ependymal cells. **Taken together, Nf1 regulated by Fbxw7 is essential for proliferation and differentiation of neural stem cells during development.**
Therefore, we demonstrated that Fbxw7 controls the Nf1 protein level in vivo.

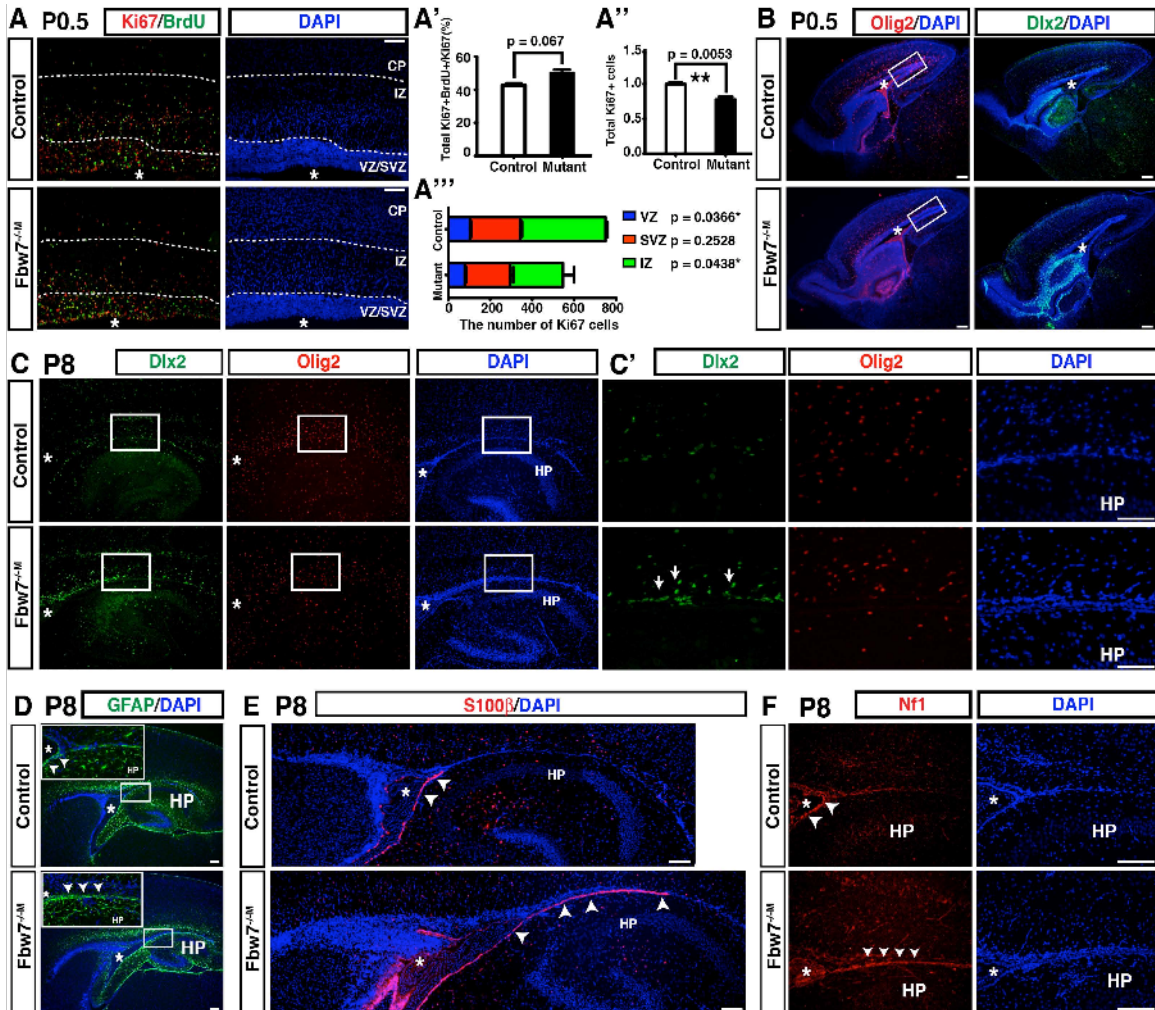


Figure 2. Inactivation of *Fbxw7* leads to increased number of ependymal cells and neuronal lineage cells in corpus callosum (CC) of the caudal region

(A) Proliferation was examined by performing BrdU/Ki67 staining in control and *Fbxw7*^{-/-M} neocortices at P0.5. (A'). The percentage of Ki67⁺/BrdU⁺ cells among total Ki67⁺ cells was not significantly different between control and *Fbxw7*^{-/-M} neocortices. The ratio of total Ki67⁺ cells in the *Fbxw7*^{-/-M} neocortices was measured and shown as a relative change versus control (A''). Total number of Ki67⁺ cells was quantified in the VZ, SVZ and IZ in control and *Fbxw7*^{-/-M} (A'''). The number of Ki67⁺ cells in VZ and IZ was significantly decreased in the *Fbxw7*^{-/-M} neocortices. (B) Olig2 demonstrated a reduction of glia progenitor cells in the *Fbxw7*^{-/-M} neocortices compare to control. Dlx2⁺ cells were increased in the RMS and anterior SVZ of *Fbxw7*^{-/-M} neocortices. (C and C') The caudal region of the *Fbxw7*^{-/-M} neocortices displayed an increase of Dlx2⁺ cells and decrease of Olig2⁺ cells. High magnification images of white boxed area are shown in C'. Arrows indicate Dlx2⁺ expressing cells in caudal region of the *Fbxw7*^{-/-M} neocortices (D) GFAP staining demonstrated that astrogenesis was not significantly impaired in the *Fbxw7*-deficient neocortices at P8. High magnification vies of boxed areas are shown in insets. Arrowheads indicate GFAP⁺ ependymal cells in caudal region of the *Fbxw7*^{-/-M} cortex. (E) Double-labeling of S100 β and DAPI illustrates ectopically increased number of ependymal cells in the caudal region of the *Fbxw7*^{-/-M} cortex. Arrowheads indicated S100 β ⁺ cells. (F) A robust level of Nfl was accumulated in the caudal region of the *Fbxw7*^{-/-M} neocortices. Arrowheads indicate Nfl-expressing cells. DAPI labels nuclei. n = 3 was used for per genotype. All quantification data are presented as mean \pm SEM. Asterisk indicates the existence of statistical significance when mutants were compared with controls: specifically, * p < 0.05, ** p < 0.01. *, lateral ventricle; VZ, ventricular zone; SVZ, subventricular zone; IZ, intermediate zone; HP, hippocampus; Scale bars: 50 μ m

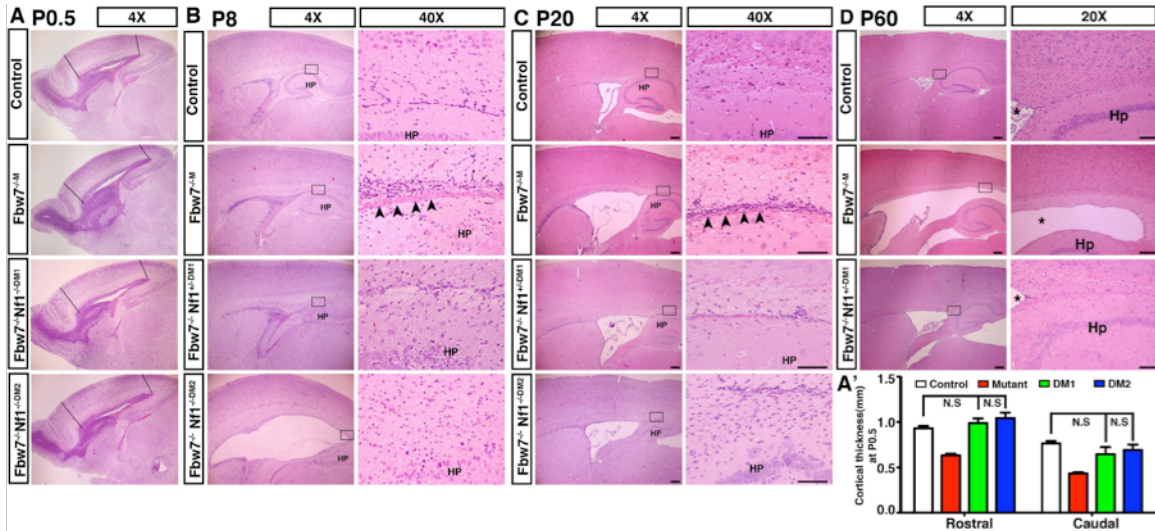


Figure 3. Reduction or ablation of *Nf1* in *Fbxw7*-deficient brains rescued the *Fbxw7* mutant brain phenotypes.

(A and A') Sagittal sections of control, *Fbxw7*^{-M}, *Fbxw*^{-/+}*Nf1*^{+/-DM1} and *Fbxw*^{-/+}*Nf1*^{+/-DM2} brains at P0.5 were stained with H&E and quantified. Black solid lines in the rostral and caudal regions of neocortices indicate the location where the thickness was measured (A'). (B and C) Postnatal control, *Fbxw7*^{-M}, *Fbxw*^{-/+}*Nf1*^{+/-DM1} and *Fbxw*^{-/+}*Nf1*^{+/-DM2} brain sections at P8 and P20 were stained with H&E. High-magnification images of boxed areas in (C) are shown in the right panel. (D) H&E staining of control, *Fbxw7*^{-M}, and *Fbxw*^{-/+}*Nf1*^{+/-DM1} brains at P60. High-magnification images of boxed areas in (D) are shown in right panel. *, lateral ventricle; HP, hippocampus; Scale bars: 50 μm

Task 2. To determine whether a high level of Erk activation is a specific context that diminishes neurofibromin protein levels in *Nf1* heterozygous cells leading to haploinsufficiency *in vitro* and *in vivo*.

Task 2.1: To determine whether high level of Erk activation lead to over-degradation of neurofibromin in *Nf1* heterozygous cells *in vivo*

We are planning to examine whether inhibition of Erk and/or *Fbxw7* can reverse learning deficits in the conditional *Nf1* heterozygous mouse model. Since numerous *Fbxw7* substrates are oncproteins, which regulate cell cycle progression result in neonatal lethality, we are establishing a new conditional *Nf1/Fbxw7* mouse model with mutations specifically in post-mitotic neurons using SynapsinI-cre (SynI-cre). Meanwhile, we attempted to set up the experimental condition for the contextual fear-conditioning assay. We performed an initial training step using control (n = 15) and *Nf1* heterozygous mice (*Nf1*^{+/-}, n = 16). We performed the experiment as described in our proposal. In brief,

control and *Nfl*^{+/−} mice were placed in a conditioning chamber for 40s, after that they were given a single foot shock (0.4mA, 2s). Mice were trained with one-day trial for five consecutive days. We expected that the freezing time would show in control mice longer than *Nfl*^{+/−} mice. However, as shown Figure 4, freezing time in both group significantly increased until 4th day, but there were no difference between control and *Nfl*^{+/−} mice. Both group already reached the highest freezing time at 4th day due to the high electronic constant-current shock. We are currently modifying foot shock condition to establish an optimal condition and resume the assay.

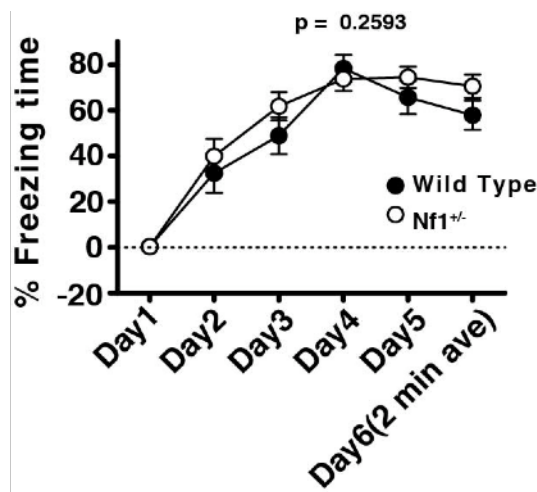


Figure 4. Contextual fear conditioning test in *Nfl*^{+/−} mice

Nfl^{+/−} mice (n = 16) and control mice (n = 15) were trained with a contextual fear-condition protocol using one trial per day for five consecutive days. The mice were places in a conditioning chamber for 40s, and subsequently given a single foot shock (0.40mA, 2s).

Key research accomplishments

We have made significant progress in the experiments proposed in Aim 1 and have established behavioral assays for the proposed experiments in Aim 2. Specifically,

1. We have investigated that *Fbxw7* has an important role in proliferation and differentiation of neural stem cells in embryonic as well as postnatal brain development.
2. We have established that *Fbxw7* controls neurofibromin level in vivo.

Reportable outcomes

1. Manuscripts (see appendix):

1. Tan, M., Zhao, Y., Kim, S.J., Liu, M., Jia, L., Saunders, T.L., Zhu, Y.*, and Sun, Y.* (2011). SAG/RBX2/ROC2 E3 ubiquitin ligase is essential for vascular and neural development by targeting NF1 for degradation. *Developmental Cell*, 21(6):1062-76 (*Co-corresponding author). PubMed PMID: 22118770.
2. Wang, Y., Kim, E., Wang, X., Novitch, B.G., Yoshikawa, K., Chang, L.S. and Zhu, Y. (2012). RAS/ERK inhibition rescues fate-specification defects of Nf1-deficient neural progenitors and brain abnormalities. *Cell*, in press.

2. Platform presentation and abstracts

None

3. Mouse Model

We have developed a mouse model, which provides new insights into the role of Nf1 as gain of function in brain development.

4. Funding

We are preparing for submitting a grant to the DOD NF program this month.

Appendices

1. Tan, M., Zhao, Y., Kim, S.J., Liu, M., Jia, L., Saunders, T.L., Zhu, Y.*, and Sun, Y.* (2011). SAG/RBX2/ROC2 E3 ubiquitin ligase is essential for vascular and neural development by targeting NF1 for degradation. *Developmental Cell*, 21(6):1062-76 (*Co-corresponding author). PubMed PMID: 22118770.

2. Wang, Y., Kim, E., Wang, X., Novitch, B.G., Yoshikawa, K., Chang, L.S. and Zhu, Y. (2012). RAS/ERK inhibition rescues fate-specification defects of Nfl-deficient neural progenitors and brain abnormalities. *Cell*, in press.

SAG/RBX2/ROC2 E3 Ubiquitin Ligase Is Essential for Vascular and Neural Development by Targeting NF1 for Degradation

Mingjia Tan,^{1,5} Yongchao Zhao,^{1,5} Sun-Jung Kim,² Margaret Liu,³ Lijun Jia,¹ Thomas L. Saunders,^{2,4} Yuan Zhu,^{2,*} and Yi Sun^{1,*}

¹Division of Radiation and Cancer Biology, Department of Radiation Oncology

²Division of Molecular Medicine and Genetics, Departments of Internal Medicine and Cell and Developmental Biology

³Department of Ecology and Evolutionary Biology, College of Literature, Science, and the Arts

⁴Transgenic Animal Model Core, Biomedical Research Core Facilities

University of Michigan, Ann Arbor, MI 48109, USA

⁵These authors contributed equally to this work

*Correspondence: yuanzhu@umich.edu (Y.Z.), sunyi@umich.edu (Y.S.)

DOI 10.1016/j.devcel.2011.09.014

SUMMARY

SAG/RBX2/ROC2 protein is an essential RING component of SCF E3 ubiquitin ligase. The role of SAG during embryogenesis remains unknown. We report a critical role for SAG in controlling vascular and neural development by modulating RAS activity via promoting degradation of neurofibromatosis type 1 (NF1). Mice mutant for *Sag* died at embryonic day 11.5–12.5 with severe abnormalities in vascular and nervous system. *Sag* inactivation caused *Nf1* accumulation and Ras inhibition, which blocks embryonic stem (ES) cells from undergoing endothelial differentiation and inhibits angiogenesis and proliferation in teratomas. Simultaneous *Nf1* deletion fully rescues the differentiation defects in *Sag*^{−/−} ES cells and partially rescues vascular and neural defects in *Sag*^{−/−} embryos, suggesting that the effects of *Sag* deletion may not be solely explained by *Nf1* misregulation. Collectively, our study identifies NF1 as a physiological substrate of SAG-CUL1-FBXW7 E3 ligase and establishes a ubiquitin-dependent regulatory mechanism for the NF1-RAS pathway during embryogenesis.

INTRODUCTION

The SCF E3 ubiquitin ligase is the largest family of E3 ligases, consisting of SKP1, Cullins, F-box proteins, and a RING protein, RING box protein-1 (RBX), also known as regulators of Cullins (ROC). The substrate specificity of SCF complex is determined by the F box proteins that bind to SKP1 and Cullins through its F-box domain and to substrates through its WD40 or LRR domains (Jin et al., 2004; Zheng et al., 2002), whereas the core SCF E3 ubiquitin ligase is a complex of Cullins-RBX, in which RBX binds to E2 and facilitates ubiquitin transfer from E2 to the substrates (Wu et al., 2000). By promoting the ubiquitination of various regulatory proteins for degradation by 26S protea-

some, SCF ligases regulate many biological processes, including apoptosis, cell cycle progression, signal transduction and DNA replication (Deshaias and Joazeiro, 2009; Nakayama and Nakayama, 2006). Although a large number of F-box proteins were found in the human genome (Jin et al., 2004) that selectively target various protein substrates, there are only two family members of RING proteins in human or mouse, RBX1 and RBX2, also known as sensitive to apoptosis gene (SAG) (Duan et al., 1999; Kamura et al., 1999; Ohta et al., 1999; Tan et al., 1999; Wei and Sun, 2010). Both family members, having a functional RING domain at the carboxyl terminus, are evolutionarily conserved with a similar tissue expression pattern (Sun et al., 2001). Although either RBX1 or SAG is capable of binding to six members of cullin family (CUL 1–3, CUL4A, B, and CUL-5) and has in vitro E3 ubiquitin ligase activity when complexed with cullin-1 (Furukawa et al., 2002; Swaroop et al., 2000), RBX1 is constitutively expressed and prefers to bind with CUL2/VHL, whereas SAG is stress-inducible and preferably binds to CUL5/SOCS (Gu et al., 2007a; Kamura et al., 2004).

The role of SAG during development has been previously studied in several model organisms. The *Hrt1*, the only yeast homolog of RBX1/SAG, is a growth-essential gene whose targeted disruption causes yeast death, which can be fully rescued by either human RBX1 (Ohta et al., 1999; Seol et al., 1999) or SAG (Swaroop et al., 2000). In *Caenorhabditis elegans*, siRNA knockdown of *Rbx1* (ZK287.5) induced the death during embryogenesis as well as in adult animals (Jia et al., 2011; Sasagawa et al., 2003), whereas knockdown of *Rbx2/Sag* (R10A10.2) did not cause any significant phenotypic changes (Moore and Boyd, 2004). In *Drosophila*, disruption of *Roc1a* or *Roc1b* caused lethality or male sterility, respectively, whereas disruption of *Roc2/Sag* caused no overt developmental phenotype (Donaldson et al., 2004; Reynolds et al., 2008). These studies suggest that RBX2 homologs in *C. elegans* and *Drosophila* are functionally redundant and RBX2 loss can be compensated by its family member, RBX1 or ROC1a/1b during embryogenesis. Our recent knockout study revealed that the *in vivo* functions of *Rbx1* and *Sag* are nonredundant in mice. In *Sag* wild-type background, the *Rbx1* inactivation caused early embryonic lethality at embryonic day 7.5 (E7.5) due to proliferation defects, which is partially caused by p27 accumulation, as simultaneous deletion of p27

extended the life span of *Rbx1* deficient embryos from E6.5 to E9.5. Thus, one *in vivo* physiological function of *Rbx1* is to ensure cell proliferation by preventing p27 accumulation during the early stage of embryogenesis (Tan et al., 2009). However, the role of Sag during mouse embryogenesis is unknown.

The *NF1* tumor suppressor gene is frequently mutated in many types of sporadic human cancers including glioblastoma multiforme, malignant peripheral nerve sheath tumor and epithelial cancers in the ovary and lung (Ding et al., 2008; Parsons et al., 2008; Sangha et al., 2008; Cancer Genome Atlas Research Network, 2008; Woodruff, 1999). Individuals with *NF1* mutations are predisposed to developing a variety of benign and malignant tumors, many of which affect the peripheral and central nervous system (Cichowski and Jacks, 2001). *NF1* contains a functional domain that shows homology to the members of the RAS GTPase activating protein (GAP) family. As a GAP, *NF1* negatively regulates RAS proto-oncogene by accelerating the conversion of active RAS-GTP to inactive RAS-GDP (Le and Parada, 2007). Upon growth factor stimulation, *NF1* is rapidly degraded by the ubiquitin-proteasome pathway (Cichowski et al., 2003; McGillicuddy et al., 2009) to ensure a proper activation of RAS signals for proliferation. Previous studies on *NF1* ubiquitination and degradation only focused on its GAP-related domain (GRD). One study found that a fragment containing *NF1* GRD domain and its adjacent 80 amino acids (codons 1096–1534) was degradation-sensitive, but did not identify corresponding E3 ubiquitin ligase (Cichowski et al., 2003). A recent study reported that ETEA, a UBA and UBX domains-containing protein, bound to *NF1* GRD domain, and negatively regulated *NF1* levels (Phan et al., 2010). However, ETEA is not a bona fide E3 ubiquitin ligase. Thus, the E3 ubiquitin ligase responsible for targeted degradation of *NF1* remains unknown.

In this study, we used a knockout approach and revealed the critical roles of Sag in embryonic vascular and neural development, and endothelial differentiation of ES cells. We found that Sag disruption caused *Nf1* accumulation to inhibit Ras-MapK signals. Simultaneous *Nf1* deletion rescues the defects fully in endothelial differentiation of *Sag^{-/-}* ES cells and partially in developing vascular and nervous system of *Sag^{-/-}* embryos, suggesting *Nf1* misregulation contributes partly to the defects derived from Sag deletion. We further showed that *NF1* is a physiological substrate of SAG-CUL1-FBXW7 E3 ubiquitin ligase. Upon recognized and bound by FBXW7, *NF1* is targeted for ubiquitination and degradation by SAG E3. Thus, our study reveals the mechanisms that regulate the stability of *NF1* proteins, which might provide insights on designing novel therapy for *NF1*-related diseases.

RESULTS

The Sag Disruption Causes Embryonic Death at E11.5–12.5

To understand the *in vivo* physiological function(s) of SAG, we inactivated Sag in mice via a gene-trap approach. Mouse *Sag* (NM_011279) was mapped onto chromosome 9 with three exons and two introns (see Figure S1A available online). One ES clone (XE423) with a gene-trap vector inserted in the second intron of the *Sag* gene was identified (Nord et al., 2006) and characterized by PCR genome walking (Figure S1A). The insertion disrupts the

Sag transcript resulting in a truncated fusion mRNA that encodes partial *Sag* N-terminal sequence without the RING domain and Sag function (Sun, 1999). The confirmed ES clone was injected into C57BL/6 blastocysts to obtain chimeras, which were back-crossed with C57BL/6 mice to obtain germline transmission. Offspring carrying the *Sag* genetrap allele were identified by PCR genotyping (Figure S1B), and further confirmed by genomic Southern blot analysis (Figures S1C and S1D). Expression of Sag protein in *Sag^{+/+}*, but not in *Sag^{-/-}* embryos was detected at E10.5 (Figure S1E).

Intercrossing of heterozygous mice, which survived to term without any observable abnormalities, failed to generate *Sag*-disrupted homozygous mice among a total of 624 genotyped offspring. The ratio of wild-type mice to heterozygous mice was about 1:2, exactly as expected for a condition with homozygous lethal phenotype (Figure S1F). To define at which stage of development the *Sag^{-/-}* embryos die, we dissected uteri of pregnant mice between E9.5 and E15.5. No viable *Sag^{-/-}* embryos were detected after E13.5 days, whereas a few viable *Sag^{-/-}* embryos were detected at E11.5–12.5 with reduced frequency. At E9.5–10.5, a Mendelian ratio of 1:2:1 (+/+:+/-:-/-) was observed (Figure S1F). Thus, homozygous deletion of Sag causes embryonic lethality at E11.5–12.5.

The Sag Disruption Causes Vascular Defects in Yolk Sacs and Embryos

Dissection of *Sag^{-/-}* embryos at E10.5 revealed that *Sag^{-/-}* embryos were growth-retarded with frequent pericardial edema (Figure 1A, arrow). Furthermore, the yolk sacs of *Sag^{-/-}* embryos have dramatic reduction of blood vessels, which was confirmed by CD31/PECAM whole-mount staining for endothelial cells (Figure 1B). Compared to *Sag^{+/+}* embryos with extensive vascular network of both large and small vessels in the head region (Figure 1C), *Sag^{-/-}* embryos exhibited disrupted vasculature with missing major blood vessels and disorganized secondary branches (Figure 1D). Similar vascular defects were also found in *Sag^{-/-}* E9.5 embryos (data not shown). Hematoxylin and eosin (H&E) stained sagittal sections revealed a substantial reduction in blood vessels and the number of nucleated red blood cells within blood islands in the yolk-sac of *Sag^{-/-}* embryos (Figure 1E, top). Vascular defects in the head region were also evident with a reduction in the number of blood vessels surrounding and within the neuroepithelium (Figures 1E and 1F).

The Sag Disruption Abrogates Endothelial Differentiation of ES Cells and Inhibits Teratoma Growth and Angiogenesis

To dissect the underlying mechanisms responsible for the observed vascular defects in *Sag^{-/-}* embryos, we turned into an *in vitro* cell culture system to circumvent early lethality caused by Sag deficiency. We generated *Sag^{-/-}* embryonic stem (ES) cells from blastocysts, obtained from *Sag^{+/+}* intercrosses. *Sag^{+/+}* ES cells underwent endothelial differentiation to form cystic embryoid bodies (cEBs) (Figure 2A) with blood island structures, lined with endothelial cells (Figure 2B, arrows). In contrast, *Sag^{-/-}* ES cells completely failed to differentiate into cEBs, although they did form EBs (Figures 2A and 2B). These results suggest that Sag is required for EBs to undergo endothelial differentiation to form cEBs under *in vitro* cultured

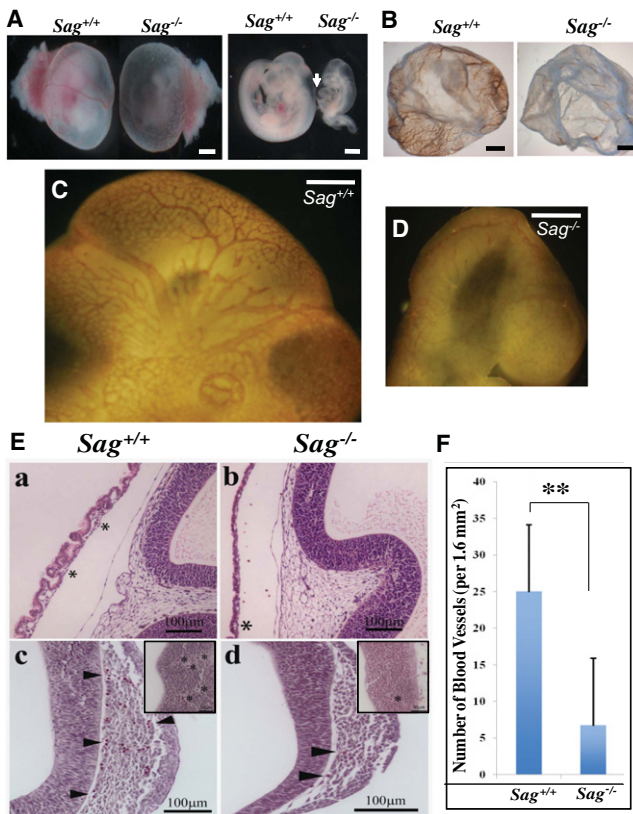


Figure 1. Sag Inactivation Disrupts Vascular Development in Yolk-Sac and Embryo Brains

(A) Appearance of mouse embryos at E10.5 with (left) and without (right) yolk-sacs. Arrow points to pericardial edema. Scale bar represents 0.75 mm.

(B) Appearance of mouse yolk sac at E10.5 after whole-mount staining with CD31. Scale bar represents 1 mm.

(C and D) Appearance of mouse embryo brain regions at E10.5 after whole-mount CD31 staining of embryos. Scale bar represents 3 mm.

(E) Reduced number of blood vessels in *Sag^{-/-}* embryos. Hematoxylin and eosin stained embryo sections of *Sag^{+/+}* (Ea, Ec) and *Sag^{-/-}* (Eb, Ed) at E10.5. * indicates network of small blood vessels with cellular contents. Arrow heads indicate blood vessels (Ec, Ed) around brain region. Insets indicate number and size of blood vessels (*) within neuroepithelium. Number of blood vessels around the entire brain region was counted (bars, SEM, n = 5 counted areas).

(F) Data were plotted. **p = 0.00269. See also Figure S1.

conditions. We next determined the growth rate and incidence of teratoma derived from ES cells upon injection into nude mice. We used two independent pairs of *Sag^{-/-}* versus *Sag^{+/+}* ES cells and found that teratomas derived from *Sag^{-/-}* ES cells grew much slower and formed significantly smaller tumors with a lower tumor incidence (AB1 teratomas developed in 2 out of 7 mice) (Figure 2C; Figure S2A). Teratomas derived from *Sag^{-/-}* ES cells also had a significantly reduced blood vessel density (Figures 2D and 2E). Immunostaining experiment revealed that these blood vessels were derived from transplanted ES cells, not from host progenitor cells, because the endothelial cells coexpressed both CD31 and β-gal (targeting vector contains β-gal cDNA) in teratomas derived from *Sag^{-/-}*, but not from *Sag^{+/+}* ES cells (Figure S2B). Furthermore, we observed a reduced proliferation rate in teratomas from *Sag^{-/-}* ES cells, compared to those from *Sag^{+/+}* ES cells (Figure 2F).

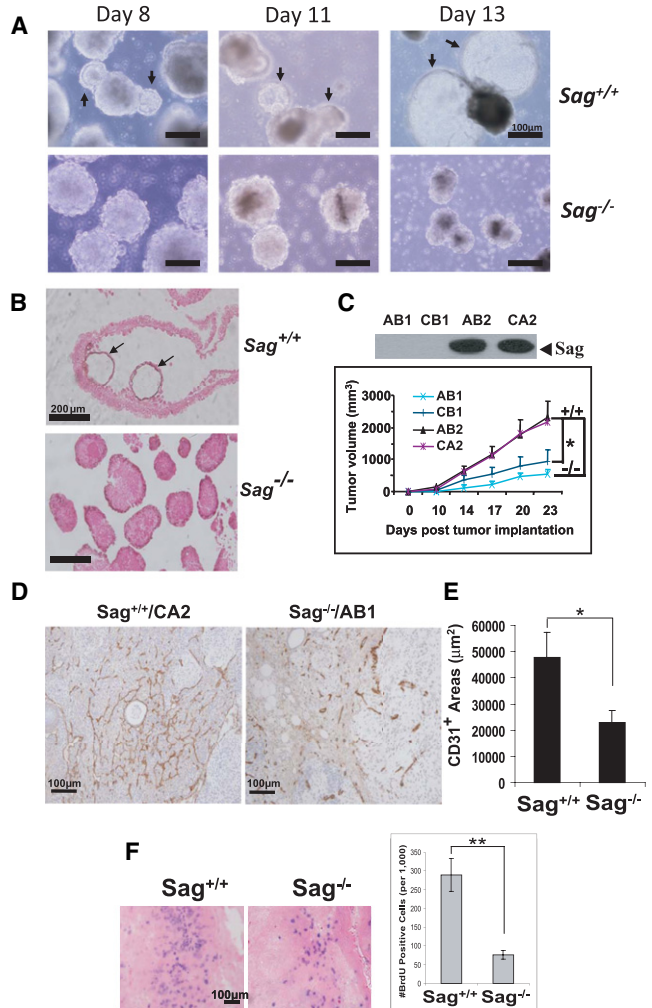


Figure 2. Sag Disruption Inhibits ES Cell Endothelial Differentiation In Vitro and Teratoma Formation In Vivo

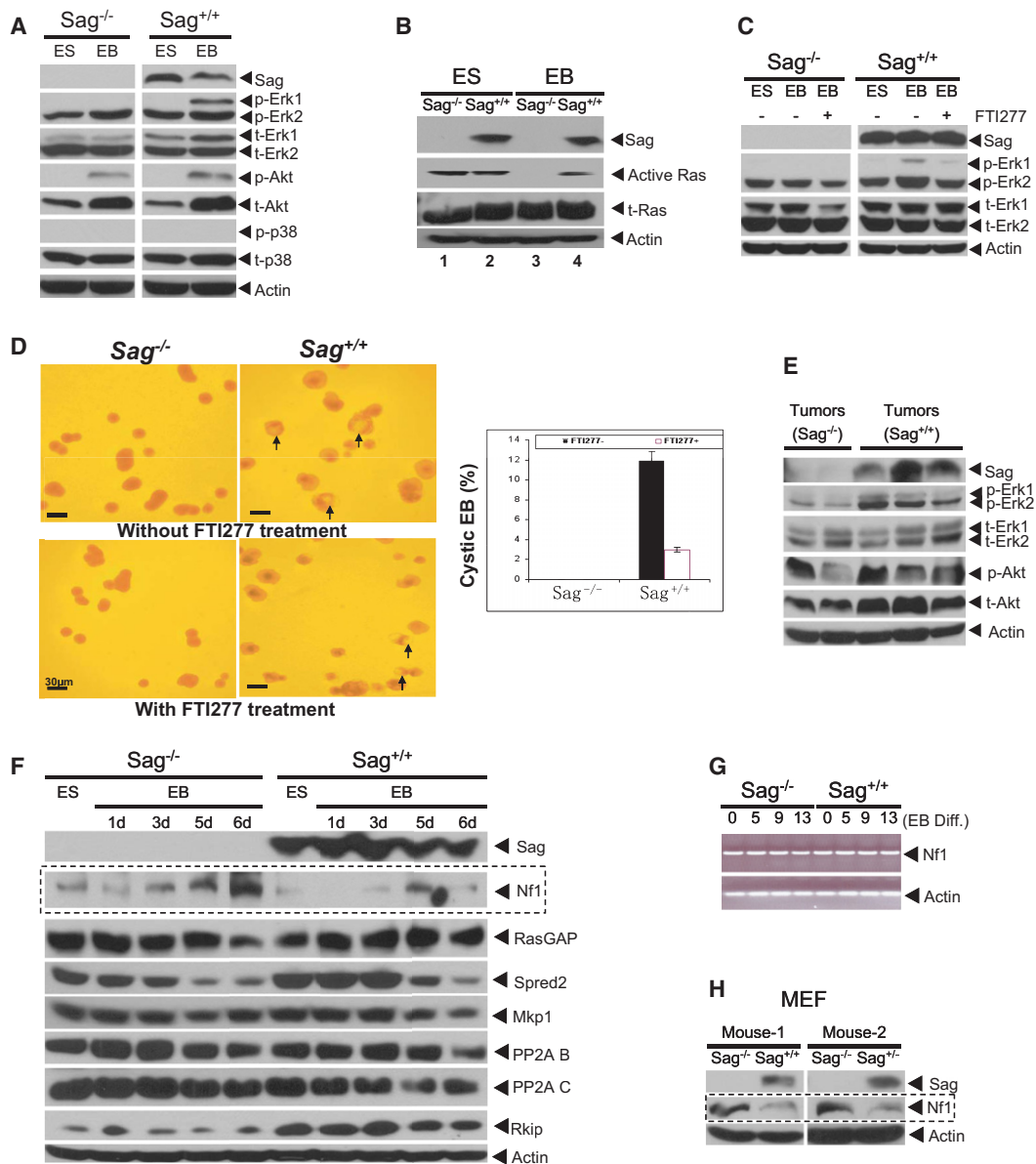
(A and B) Endothelial differentiation of embryoid bodies: ES cells underwent endothelial differentiation for indicated periods and photographed. Arrows indicate cystic EBs that occurred in *Sag^{+/+}* ES cells only (A). The EBs were whole-mounted with CD31, and counterstained with eosin (200×) (B).

(C–F) Growth and angiogenesis of teratomas. Two pairs of ES cell lines, AB2/CA2 (*Sag^{+/+}*) versus AB1/CB1 (*Sag^{-/-}*) (C, top) were injected into nude mice (seven per group). Tumor growth was monitored for 23 days. The mean tumor volume (mm³) of seven tumors (except AB1 line with two tumors generated) was plotted (mean ± SEM, *p = 0.0044, between AB1/CB1 and AB2/CA2, using an F-test from the mixed model) (C, bottom). Tumor sections were immunostained with CD31 for microvessels (D), and were quantified in multiple representative areas of at least two tumors (mean ± SEM; *p = 0.0117) (E). Mice were injected with BrdU and tumor tissues were processed for BrdU staining. BrdU positive cells (blue) were counted in multiple areas (mean ± SEM; **p = 0.0002) (F). See also Figure S2.

Thus, Sag disruption remarkably inhibits angiogenesis and growth/proliferation of teratomas in vivo.

Sag Is Required for Active Ras/MapK Signals during Endothelial Differentiation and Teratoma Proliferation

Because RAS/MAP kinase pathways are known to regulate proliferation, angiogenesis, and endothelial cell differentiation

**Figure 3. Sag Disruption Causes Inactivation of Ras/Mapks and Accumulation of Nf1**

(A and B) ES cells were cultured without LIF in static suspension to induce the formation of EBs and cystic EBs up to 13 days. The EBs were lysed for immunoblotting (IB) (A) or assayed for Ras activity (B).

(C and D) ES cells were differentiated for 13 days in the absence or presence (days 2–4) of FTI277 (1 μM), and lysed for IB (C) or photographed to show cystic EBs (arrows) (D, left). The % of cEBs in a total of ~300 EBs was plotted, mean ± SD (n = 3) (D, right).

(E) Inhibition of Erk phosphorylation. Independent teratoma tissues derived from *Sag*^{-/-} or *Sag*^{+/+} ES cells were homogenized for IB.

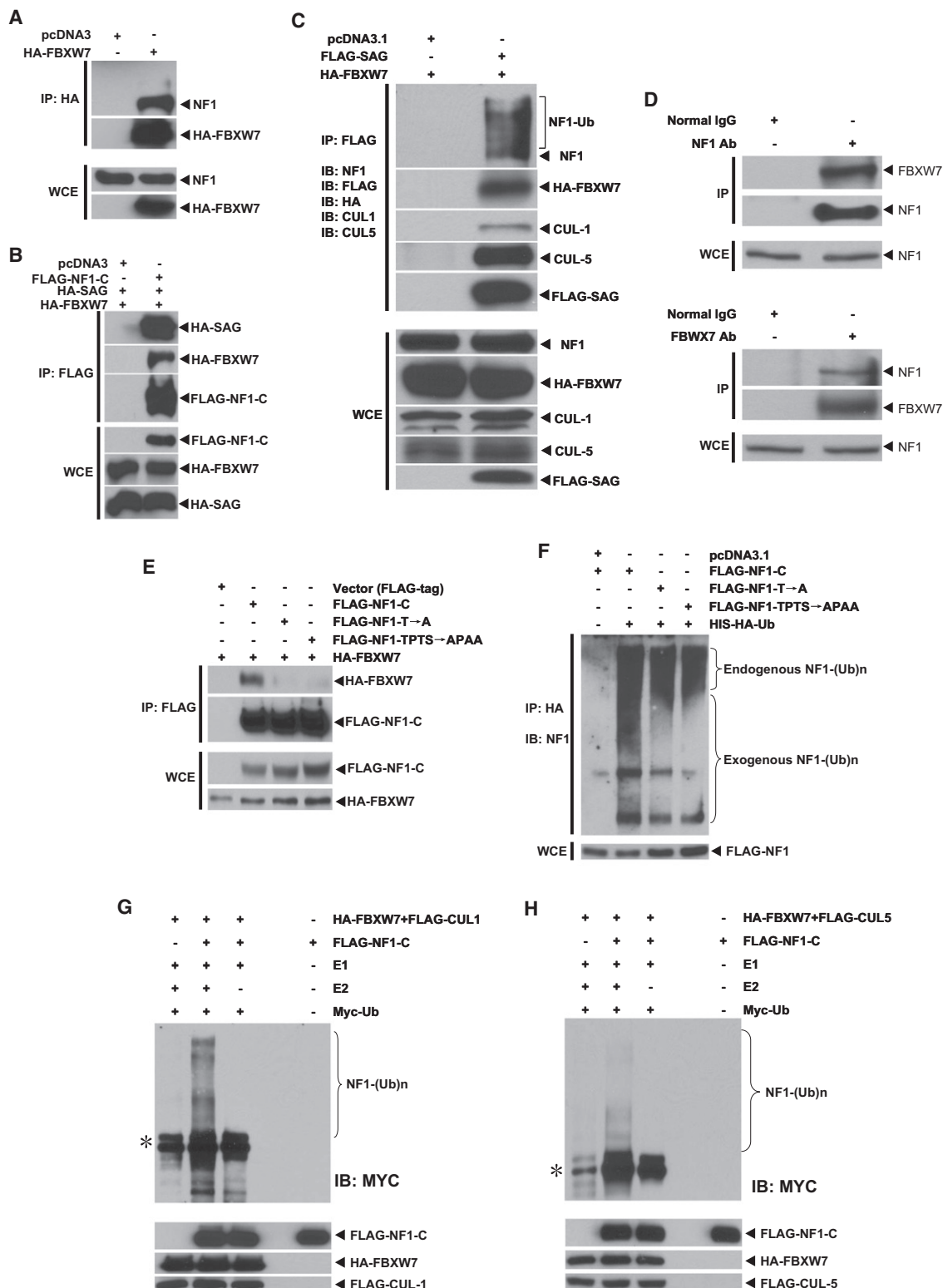
(F) Nf1 accumulation in *Sag*^{-/-} EBs. ES cells and EBs (differentiated for up to 6 days) were lysed for IB.

(G) No change in Nf1 mRNA during ES cell differentiation. ES or EBs were collected at indicated time points for RT-PCR analysis.

(H) Nf1 accumulation in *Sag*^{-/-} MEFs. Primary MEFs were prepared from E10.5 embryos for IB. See also Figure S3.

(Kawasaki et al., 2008; Kranenburg et al., 2004), we sought to determine whether the Ras signaling pathway is inactivated during *Sag*^{-/-} ES cell differentiation. As shown in Figure 3A, phosphorylation of p44/Erk1 was significantly induced during differentiation of *Sag*^{+/+} EBs, but not in *Sag*^{-/-} EBs. No difference was seen in the levels of total or phosphorylated forms of Akt and p38. A Ras activity assay further showed that Ras was active in ES cells, regardless of Sag status, but was completely

inactive in EBs derived from *Sag*^{-/-} ES cells (Figure 3B). Similar results were obtained from another independent set of ES clones (data not shown). Thus, Ras activation and Erk1 phosphorylation were maintained during cystic EB formation, whereas they were inactivated in the absence of Sag. We further found that FTI277, an inhibitor of Ras farnesyltransferase (Kawasaki et al., 2008) that inhibited p44/Erk1 phosphorylation (Figure 3C), could significantly reduce cystic EB formation from *Sag*^{+/+} ES cells

**Figure 4. FBXW7 and SAG Bind to NF1 and Promote Its Ubiquitination**

(A–C) SAG-FBXW7-NF1 forms a complex in vivo. The 293 cells were transfected and treated with MG-132 (10 μM) 4 hr prior to harvesting. Cell lysates were immunoprecipitated (IP) with bead-conjugated FLAG or HA Abs, followed by IB. The bottom panels are the direct IB using WCE (whole cell extract) as input. (D) Endogenous FBXW7-NF1 binding: Cell lysates from 293 cells were immunoprecipitated using Ab against NF1 (top) or FBXW7 (bottom), along with normal IgG control, followed by IB. Direct IB was performed using WCE.

(Figure 3D). A similar result was obtained with PD98059, a Mek inhibitor (Figure S3). Consistently, a reduced Erk phosphorylation, an indicator of Mek inactivation, was found in *Sag*^{-/-} teratoma tissues, as compared to *Sag*^{+/+} teratomas (Figure 3E). Taken together, the findings demonstrated that the inability to maintain active Ras/Erk signals, upon *Sag* disruption, contributes significantly to the failure of endothelial differentiation in vitro, angiogenesis, and possibly reduced proliferation in teratomas in vivo.

Accumulation of Neurofibromin during ES Cell Differentiation and in MEFs upon *Sag* Disruption

RAS signaling pathways are inhibited by naturally occurring inhibitory proteins or inactivating phosphatases (Karnoub and Weinberg, 2008; Kolch, 2005). These proteins, upon *Sag* disruption, would accumulate to inactivate the RAS pathway during endothelial differentiation if they were the direct substrates of SAG-SCF E3 ubiquitin ligases. We therefore examined the levels of several Ras signaling inhibitory proteins in ES cells and in EBs formed during differentiation. As shown in Figure 3F, the basal level of neurofibromin (encoded by *Nf1*) was slightly higher in *Sag*^{-/-} ES cells than that in *Sag*^{+/+} ES cells. The neurofibromin (*Nf1*) level gradually increased, reaching the peak at day 6 of *Sag*^{-/-} EB differentiation, but remained low in *Sag*^{+/+} EBs. No significant difference was observed between the two groups in the levels of p120RasGap, a family member of *Nf1* with a similar Ras inhibiting activity (Henkemeyer et al., 1995), nor of other Ras/Raf inhibitors or phosphatases of the Ras pathway tested (Dhillon et al., 2007b; Kolch, 2005), including Spred2, Mkp-1, and PP-2A (subunits B and C), except Rkip, a Raf inhibitor (Hagan et al., 2006), which showed higher levels in *Sag*^{+/+} ES cells and EBs, but was not regulated by ES cell differentiation (Figure 3F). RT-PCR analysis revealed that *Nf1* mRNA remained consistent during ES cell differentiation, regardless of *Sag* status (Figure 3G), indicating that *Nf1* accumulation upon *Sag* disruption likely results from a reduced degradation. We further measured the *Nf1* levels in mouse embryonic fibroblasts (MEF) derived from E10.5 embryos with three *Sag* genotypes and found an elevated *Nf1* level in *Sag*^{-/-} MEFs, as compared to that in *Sag*^{+/+} or *Sag*^{+/-} MEFs (Figure 3H). Taken together, our results suggested that *Nf1* could be a substrate of SAG-SCF E3 ubiquitin ligase, which accumulates upon *Sag* disruption, to inhibit Ras/Erk signals.

SAG-CUL1-FBXW7 Binds to NF1 and Promotes Its Ubiquitination

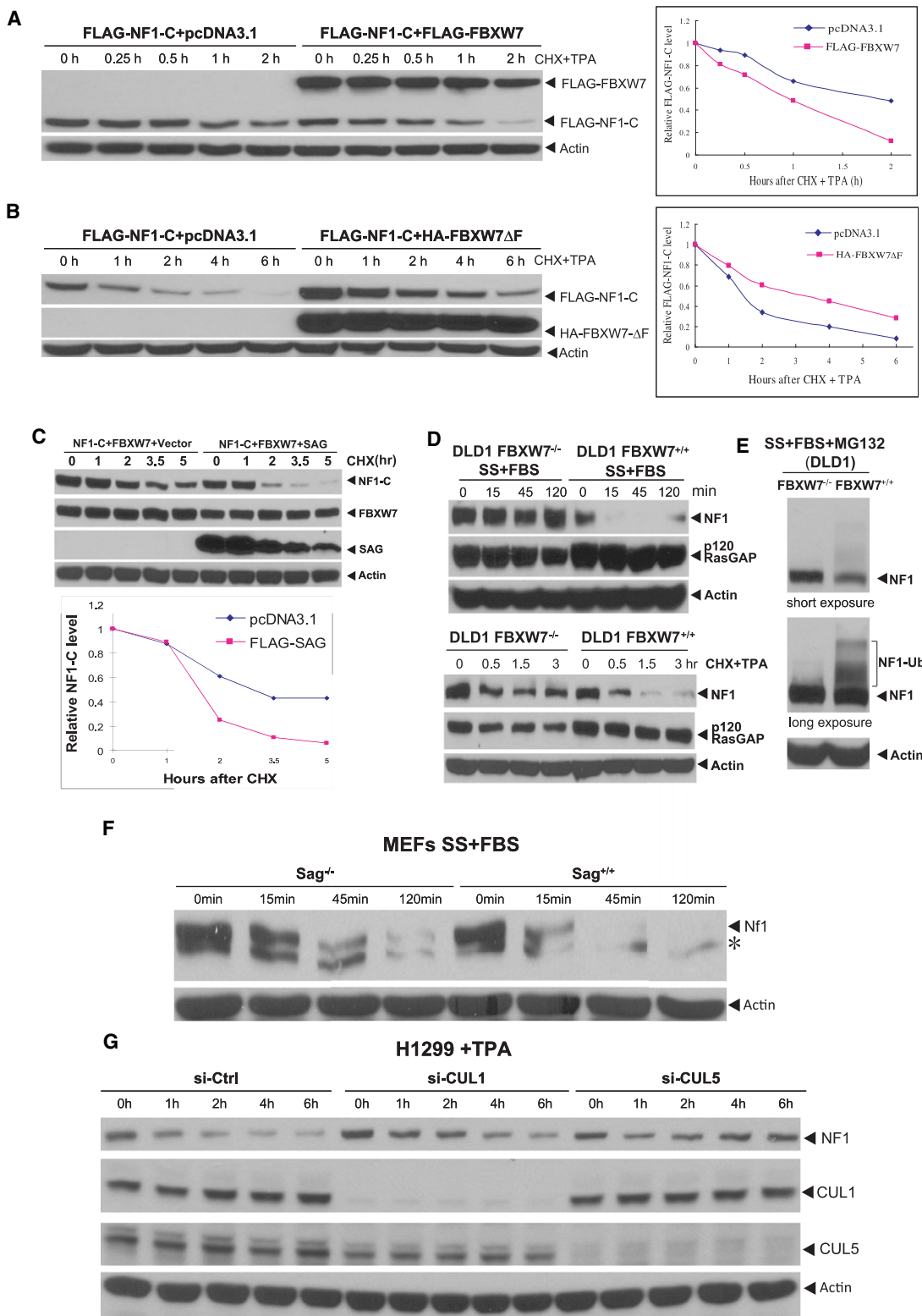
The crystal structure of SCF complex (Zheng et al., 2002) reveals that the substrate is recognized and recruited by an F-box protein to the ligase complex for ubiquitination. Thus, *Sag*-mediated *Nf1* degradation must involve an F-box protein that recognizes *Nf1* for binding. Examination of the *NF1* sequence

for the consensus binding motifs of several F-box proteins revealed an evolutionarily conserved perfect binding site for FBXW7 (also known as CDC4) (L-I/L/P-pT-P-XXXX) at the C terminus (Figure S4A), which is consistent with the binding motif found in other known substrates of FBXW7 (Figure S4B). No FBXW7 binding site was identified in p120RasGAP, a family protein not subject to proteasome-dependent proteolysis (Cichowski et al., 2003). We therefore determined the potential binding of FBXW7 and NF1. Using an immunoprecipitation assay, we found that transiently transfected FBXW7 pulled down endogenous NF1 (Figure 4A). In a reciprocal experiment, NF1-C, a C-terminal portion of NF1 (codons 2180–2840) containing the FBXW7 binding site, pulled down both FBXW7 and SAG when cotransfected, indicating in vivo binding of SAG-FBXW7-NF1 (Figure 4B). Furthermore, SAG, when cotransfected with FBXW7, pulled down FBXW7, as well as endogenous NF1 and CUL1 (Figure 4C), indicating an in vivo formation of SAG-CUL1-FBXW7 E3 ligase. More significantly, SAG cotransfection promoted FBXW7-mediated ubiquitination of endogenous NF1, as demonstrated by slower migrating bands (Figure 4C, top), which was not observed when FBXW7 was transfected alone (Figure 4A, top). In order to detect endogenous FBXW7-NF1 binding, we examined several commercially available antibody against FBXW7 and identified one from Sigma that was capable of detecting overexpressed FBXW7 (data not shown). Using this antibody, we were able to detect endogenous FBXW7-NF1 binding, as evidenced by detection of FBXW7 (likely being enriched when complexed with NF1) in NF1 immunoprecipitates (Figure 4D, top panels). Reciprocally, NF1 can also be detected in FBXW7 immunoprecipitates (Figure 4D, bottom panels).

We next determined if FBXW7-NF1 binding and NF1 ubiquitination were dependent on the FBXW7 consensus-binding motif on NF1. We generated two NF1 mutants on the FBXW7 binding motif (Figure S4C) and found that these mutations had a significant reduction in binding to FBXW7 (Figure 4E). Consequently, FBXW7-induced ubiquitination of exogenously expressed NF1-C was remarkably inhibited in these mutants, without affecting ubiquitination of endogenous NF1 (Figure 4F). We further determined NF1 ubiquitination using an in vitro purified system and found that FBXW7-CUL1 promoted NF1 ubiquitination in a manner dependent on E2 ubiquitin conjugating enzyme (Figure 4G). The involvement of CUL1 in promoting NF1 ubiquitination was further demonstrated as follows: (1) endogenous NF1 could be pulled down by exogenously expressed CUL1 (Figure S4D), (2) siRNA knockdown of CUL1 significantly inhibited NF1 ubiquitination (Figure S4E), and (3) endogenous SKP1 were present in SAG immunoprecipitates (Figure S4F). Thus, SAG-SKP1-CUL1-FBXW7 could form an active E3 ubiquitin ligase in vivo that regulates cellular levels of NF1 by promoting its ubiquitination and degradation. To a lesser extent, CUL-5 appears to be also involved in NF1 degradation (Figures

(E and F) NF1-FBXW7 binding and NF1 ubiquitination: FLAG-tagged NF1-C and its two mutants were cotransfected into H1299 cells. Cells were treated with MG-132 (10 μM) 4 hr before harvesting for (E) IP with FLAG and IB with FLAG or HA, or for (F) IP with HA and IB with NF1 Ab to show ubiquitination of both endogenous (top) and exogenously expressed NF1-C (bottom), or with FLAG for direct IB (bottom).

(G and H) CUL1-FBXW7 or CUL5-FBXW7 promotes NF1 ubiquitination in vitro: SCF E3 was prepared by FLAG bead IP using 293 cells transfected with CUL1 and FBXW7 (G) or CUL5 and FBXW7 (H). NF1 substrate was prepared by transfecting FLAG-NF1-C into 293 cells, followed by FLAG-bead IP and 3xFLAG peptide elution. SCF E3 and NF1-C substrates were added into a reaction mixture containing ATP, Myc-Ub, E1, and E2. E2 was omitted in some reactions. The reaction mixture after 60 min incubation was subjected to IB using c-Myc-tag Ab. * denotes nonspecific bands. See also Figure S4.

**Figure 5. FBXW7 and SAG Shorten NF1 Protein Half-Life**

(A and B) FBXW7 shortens, but FBXW7ΔF extends the NF1 protein half-life: The 293 cells were transfected and treated with CHX (cycloheximide) to block new protein synthesis and with TPA to trigger degradation. Samples were harvested for IB. Densitometry quantification was performed with ImageJ.

(C) SAG further shortens NF1 protein half-life: FLAG-NF1-C was cotransfected with FBXW7, with or without FLAG-SAG into 293 cells. Cells were harvested after CHX treatment for IB and quantified by ImageJ.

4C and 4H; Figures S4D and S4E), although it generally belongs to an E3 complex with SOCS-SAG (Kamura et al., 2004).

SAG-FBXW7 Shortens NF1 Protein Half-Life and Is Required for Serum- or Mitogen-Induced NF1 Ubiquitination and Degradation

We next determined whether FBXW7 shortens protein half-life of NF1, and whether SAG could further accelerate it. The protein half-life of transfected NF1-C was ~2 hr upon TPA stimulation, which was reduced to ~1 hr when cotransfected with wt FBXW7 (Figure 5A), but extended to ~4 hr when cotransfected with an F-box deleted dominant negative FBXW7 mutant (Figure 5B). The protein half-life of two NF1 mutants was much extended under the same conditions (Figures S5A and S5B). Moreover, cotransfection of SAG with FBXW7 further shortened the protein half-life of NF1-C from 3 hr (FBXW7 alone) to ~1.5 hr (when combined) in the absence of TPA stimulation (Figure 5C). We further determined the effect of FBXW7 on protein half-life of endogenous NF1. Under normal growth conditions, endogenous NF1 is relatively stable with a protein half-life much longer than 3 hr, regardless of FBXW7 status (Figure S5C). NF1 was, however, subject to mitogen-induced reduction in an FBXW7-dependent manner. In serum-starved FBXW7^{-/-} DLD1 cells (Rajagopalan et al., 2004), serum addition had no effect on NF1 levels up to 120 min. In contrast, serum addition to starved FBXW7^{+/+} DLD-1 cells induced a rapid elimination of NF1 within 15 min, which lasted up to 120 min before it started to recover (Figure 5D, top). Likewise, the protein half-life of endogenous NF1 after exposure to TPA was about 30 min, which was extensively extended in FBXW7^{-/-} cells (Figure 5D, bottom). No change at the level of p120RasGAP was observed, regardless of FBXW7 status (Figure 5D). We further confirmed that FBXW7-dependent NF1 reduction was via the ubiquitin-proteasome pathway, because concurrent MG-132 treatment blocked NF1 degradation, along with accumulation of ubiquitinated NF1 in FBXW7^{+/+} cells, but not in FBXW7^{-/-} cells (Figure 5E). Finally, we found that both SAG and CUL1/5 were involved in controlling the NF1 turn-over. The Nf1 half-life was much extended in Sag^{-/-} MEF cells, as compared to Sag^{+/+} cells under the conditions of serum starvation, followed by serum addition to trigger Nf1 degradation (Figure 5F). Similarly, TPA-induced NF1 degradation was much delayed upon siRNA knockdown of either CUL1 or CUL5 (Figure 5G). Thus, NF1 is a physiological substrate of SAG-CUL1-FBXW7 (and possibly a SAG-CUL5-based E3 ligase) for targeted degradation.

Simultaneous Deletion of Nf1 Rescues the Vascular Defects in Sag^{-/-} ES Cells and Embryos

We next attempted to define the physiological importance of Nf1 accumulation upon Sag disruption in endothelial differentiation of ES cells and vascular development of embryos. We reasoned that if Nf1 accumulation inhibits endothelial differentiation of

EBs by inhibiting Ras/Erk activation, then simultaneous deletion of Nf1 would restore the formation of cystic EBs in the Sag^{-/-} background. We generated Sag/Nf1 double null ES clones from blastocysts obtained by the mating of Sag^{+/+} and Nf1^{+/+} mice (Zhu et al., 2005). Among 64 ES lines established, we identified a single clone (ISG8) with the Sag^{-/-};Nf1^{-/-} genotype. However, this clone did not grow well and was readily attached onto the Petri dish during suspension culture for differentiation, leading to much fewer numbers of embryoid bodies, although we did observe the formation of cEBs at a rate comparable to that of wild-type (Figure 6A) with full restoration of Ras activity (Figure S6B). We then focused our attention to three independent Sag^{-/-};Nf1^{+/+} ES cell lines and found that all three were able to undergo endothelial differentiation to form cystic EBs, although the frequency was relatively lower than that of wild-type (Figures 6A and 6C, two clones, A1 and A10 were shown). The blood island structures with endothelial lining were apparent in these rescued cEBs (Figure 6B), indicating that heterozygous loss of Nf1 is sufficient to rescue the defect in endothelial differentiation caused by Sag inactivation. We further confirmed that the Nf1 status on the Sag^{+/+} background did not affect endothelial differentiation, because both Nf1^{+/+} and Nf1^{-/-} ES cells are capable of forming cEBs (Figure S6C). We next determined if Ras activity was also rescued upon Nf1 inactivation and found that although Sag^{-/-};Nf1^{+/+} EBs showed a high level of Nf1 with a undetectable Ras activity (Figure 6D, lane 1), Sag^{-/-};Nf1^{+/+} EBs had a significant lower level of Nf1, but a high level of activated Ras, similar to that seen in wild-type EBs (Figure 6D, lanes 2 versus 3). These results suggested that loss of one Nf1 allele is sufficient to reduce abnormally high levels of Nf1 (caused by Sag disruption) to a level that permits cystic EB formation during ES cell differentiation. Taken together, our results demonstrated that Ras inactivation, as a result of Nf1 accumulation upon Sag disruption, is the major cause for the failure of Sag^{-/-} ES cells to undergo endothelial differentiation.

We then determined whether simultaneous deletion of Nf1 would rescue vascular defects in Sag^{-/-} embryos (Figure 1D) by crossing of Sag^{+/+} mice with Nf1^{+/+} mice. Although homozygous deletion of Nf1 caused embryonic lethality by E13.5 due to cardiac defects, mutant embryos appeared normal through E10.5 (Brannan et al., 1994; Jacks et al., 1994). We examined the blood vessel networks in head areas of E10.5 embryos with four genotypes, using CD31 whole-mount staining (Figure 6E). Whereas Sag^{-/-};Nf1^{+/+} brains showed reduced primary vascular networks with missing major trunk vessels, Sag^{+/+};Nf1^{-/-} brains showed relatively normal vasculature, similar to that of Sag^{+/+};Nf1^{+/+}. Significantly, the vasculature in the head areas of Sag^{-/-};Nf1^{-/-} embryos showed a partial restoration with reappearance of some trunk blood vessels (Figure 6E), even though these Sag^{-/-};Nf1^{-/-} embryos remained growth-retarded (Figures 6E and 6F). Furthermore, CD31-positive

(D and E) FBXW7-dependent degradation of endogenous NF1. DLD-1 cells with or without FBXW7 deleted were serum starved for 24 hr, followed by serum addition. Cells were then harvested for IB (D, top). Cells were treated with TPA and CHX, and harvested for IB (D, bottom). DLD-1 cells were serum starved for 24 hr, followed by serum addition in combination with MG-132. Cells were harvested 15 min later for IB (E).

(F and G) Inactivation of Sag or CUL1/5 extended Nf1 protein half-life: MEFs (Sag^{+/+} or Sag^{-/-}) were serum starved up to 48 hr, followed by serum addition. Cells were harvested at indicated periods for IB. * denotes nonspecific band (F). H1299 cells were transfected with siRNA targeting CUL1 or CUL5, along with control siRNA. Cells were treated with TPA (10 nM) 48 hr later for indicated periods and harvested for IB (G). See also Figure S5.

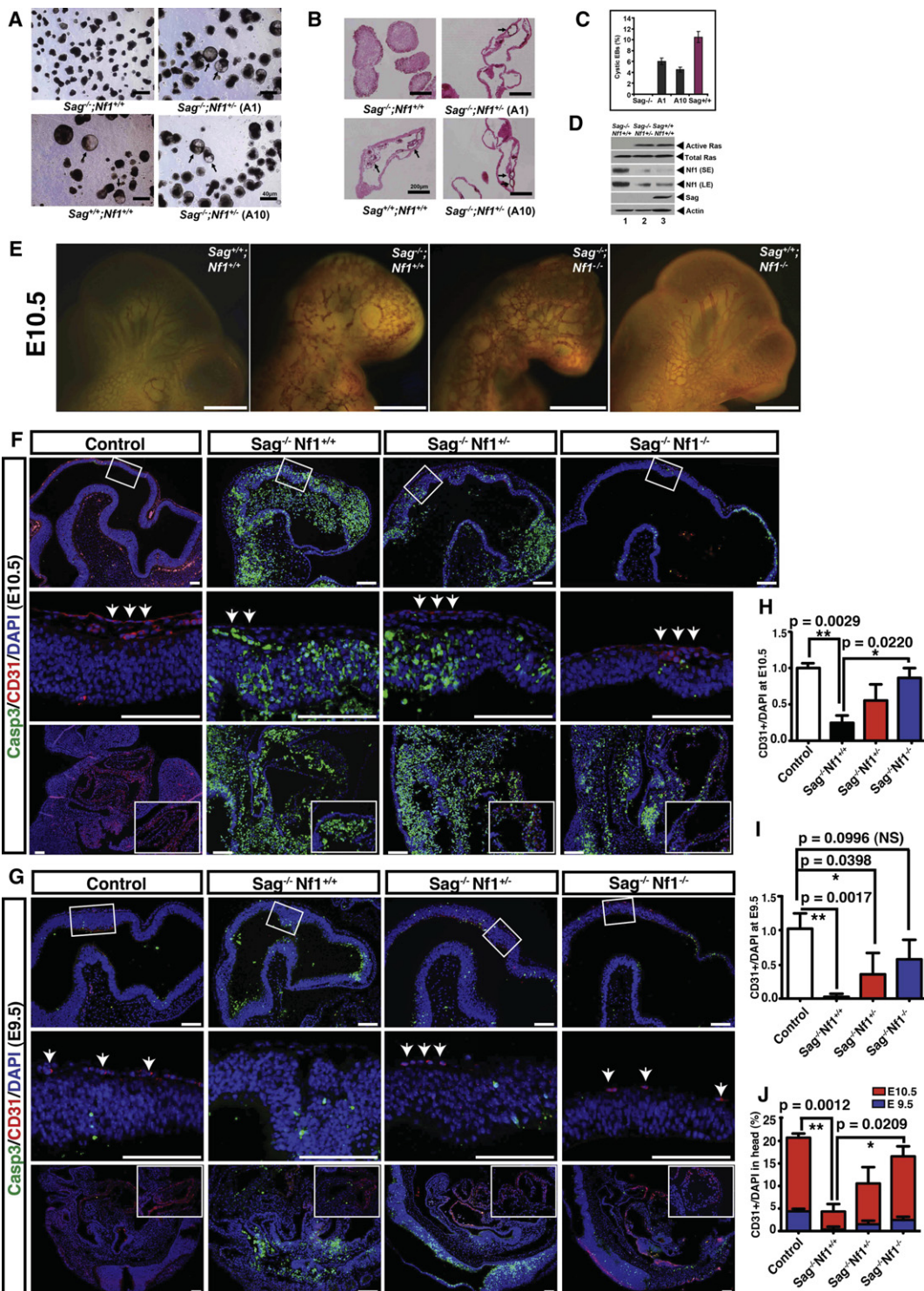


Figure 6. Rescuing *Sag*^{-/-} Defective Phenotypes by Simultaneous Deletion of *Nf1*

(A–C) Heterozygous deletion of *Nf1* rescued the differentiation defects. ES cells underwent endothelial differentiation for 12 days and were photographed to show cystic EBs (A, arrows). The EBs were whole-mounted with CD31, and counterstained with eosin (200 \times) (B). The proportion of cEBs in a total of ~300 EBs was plotted, mean \pm SD ($n = 3$) (C).

(D) Heterozygous deletion of *Nf1* rescued Ras activity. EBs formed after differentiation for 5 days were measured for Ras activity by a pull-down assay, and IB for total Ras, *Nf1*, and *Sag*. SE, short exposure; LE, longer exposure.

(E) *Nf1* deletion partially rescued vascular defects in embryonic brains: *Sag*^{+/-}; *Nf1*^{+/-} mice were intercrossed, embryos at E10.5 were dissected and subjected to CD31 whole-mount staining. Representative embryos of four genotypes were photographed. Scale bar represents 3 mm.

endothelial cells in control embryos formed a chain-like structure that covered the entire neuroepithelium, whereas only residual CD31-positive cells were found in the *Sag*^{-/-} embryos (arrows, Figure 6F). Importantly, the chain-like structure formed by CD31-positive endothelial cells was partially restored by both *Nf1* heterozygous and homozygous mutations (Figures 6F and 6H).

Consistent with our previous observation that SAG is an anti-apoptotic protein in cell culture settings (Duan et al., 1999; Sun et al., 2001), we observed that Sag disruption caused a widespread apoptosis in embryos evidenced by cleaved caspase 3 staining (Figure 6F). To rule out the possibility that excessive apoptosis observed in Sag-deficient embryos could potentially exert nonspecific effects on normal development of endothelial cells, we further analyzed control and Sag-deficient embryos at earlier stages. At E9.5, compared to controls, *Sag*-deficient embryos exhibited relatively normal morphology with only a minor increase in apoptosis within developing nervous system (Figure 6G). However, the number of CD31-positive endothelial cells was greatly reduced in *Sag*-deficient embryos (arrows, Figure 6G). Particularly, compared to control embryos, *Sag*-deficient embryos only contained <10% of CD31-positive endothelial cells in the head areas (Figure 6I). Strikingly, this defect was significantly rescued by loss of one or two alleles of *Nf1* (arrows, Figures 6G and 6I). When comparing the relative number of CD31-positive endothelial cells at E9.5 and E10.5 among control, *Sag* single, and *Sag/Nf1* double mutant embryos, we found that CD31-positive endothelial cells in all the mutant embryos, albeit at a much lower level, expanded proportionally from E9.5 to E10.5, as compared to those in controls (Figure 6J). Taken together, our studies, using both *in vitro* ES cells and *in vivo* embryos, suggest that Sag-mediated *Nf1* degradation is critical for the genesis of endothelial cells in the vascular system. This notion was further supported by the fact that CD31-positive endothelial cells in *Sag*-deficient embryos at both E9.5 and E10.5 stages did not colocalize with caspase-3 positive cells (Figures 6F and 6G), excluding the involvement of apoptosis.

***Nf1* Inactivation Partially Rescues Apoptotic, but Not Proliferative, Defects in Developing *Sag*-Deficient Neural Precursor Cells**

To further determine genetic interaction between Sag and *Nf1* *in vivo*, we studied *Nf1*-dependent Sag function in the developing nervous system, as 40%–80% of NF1 children exhibit learning deficits (Hyman et al., 2005). During development, the onset of neurogenesis in the neocortex occurs at the basal surface of the neuroepithelium at E10.5 (Farkas and Huttner, 2008; Götz and Huttner, 2005). We found that neuronal differentiation, revealed by Tuj1 expression, was not significantly different between control and *Sag*-deficient embryos with or without addi-

tional *Nf1* mutations (Figures 7A and 7B). These results indicate that *Sag*^{-/-} neural precursor cells in the neocortex undergo neuronal differentiation according to a normal developmental schedule, albeit in overall growth-retarded embryos. We next examined whether there are proliferation defects in *Sag*^{-/-} neural precursor cells. During cell cycle, neural precursor cells undergo DNA replication (S phase) in the basal part of the neuroepithelium (Farkas and Huttner, 2008), which were labeled by a single BrdU pulse (Figure 7C, upper left). The nuclei of neural precursor cells migrate apically through G2 phase to undergo M phase in apical position along the ventricle, which were revealed by an M phase marker, phospho-histone H3 (PH3) (Figure 7C, bottom left). Strikingly, little or no BrdU- or PH3-positive neural precursor cells were identified in the *Sag*^{-/-} neocortex (Figure 7C). More importantly, none of the defects in cell cycle progression was rescued by *Nf1* inactivation (Figure 7C). Thus, *Sag*-deficient neural precursor cells in the developing neocortex exhibited severe defects in entering S and M phases of the cell cycle in an *Nf1*-independent manner. Consequently, compared to control neocortex, the number of neural precursor cells labeled by Ki67 expression was significantly reduced in the *Sag*^{-/-} neuroepithelium, consistent with the fact that these cells had proliferation defects (Figures 7D and 7E). Given that *Nf1* deficiency does not rescue cell-cycle progression defects in *Sag*^{-/-} neural precursor cells, we unexpectedly observed a significant level of rescue of Ki67-positive neural precursor cells upon *Nf1* deletion (Figures 7D and 7E). We, therefore, determined whether apoptosis additionally contributed to *Nf1*-dependent reduction of neural precursor cells in *Sag*^{-/-} neocortex. Although control neocortex had little or no caspase3-positive apoptotic cells, nearly 40% of *Sag*^{-/-} cells in E10.5 neocortex were undergoing apoptosis, which was significantly rescued by *Nf1* inactivation in a dose-dependent manner (Figures 7D and 7F). In addition to the developing brain, *Nf1* inactivation also partially rescued apoptosis in the *Sag*-deficient spinal cord (arrows, Figure 7G), though apoptosis in surrounding mesoderm-derived tissues was not affected (Figure 7G). Moreover, neuronal apoptosis of *Sag*^{-/-} E9.5 embryos could also be rescued by *Nf1* deletion (Figure 6G; Figure S6D). Taken together, our observations demonstrate that during neocortical development, Sag plays critical roles in regulating apoptosis and cell cycle progression in an *Nf1*-dependent and *Nf1*-independent manner, respectively. Furthermore, *Nf1*-dependent Sag function in suppressing apoptosis is specifically required for developing nervous system, but not for surrounding mesenchymal tissues.

DISCUSSION

Despite Sag being dispensable during development in *Drosophila* and *C. elegans* (Moore and Boyd, 2004; Reynolds

(F and G) Deletion of *Nf1* partially rescued a reduction of endothelial cells in *Sag* deficient embryos at E10.5 (F) and E9.5 (G). Sagittal sections of control and mutant embryos were stained with CD31, cleaved caspase 3, and DAPI. Images were captured at low and high-magnifications for cranial neuroepithelial cells (top and middle panels) as well as for trunk areas (bottom panels). Scale bar represents 100 μm.

(H and I) Quantification of CD31 positive cells in the head areas at E10.5 (H) and E9.5 (I). The data were normalized to the total number of DAPI and represented as fold change relative to the number of CD31 positive cells in *Sag*^{+/+} *Nf1*^{+/+}, which were set to 1 (mean ± SEM, n = 3).

(J) The percentage of CD31 positive cells in head areas of control and mutant embryos at E9.5 and E10.5. The number of cells expressing CD31 was normalized to the total number of DAPI positive cells. (mean ± SEM, n = 3). See also Figure S6.

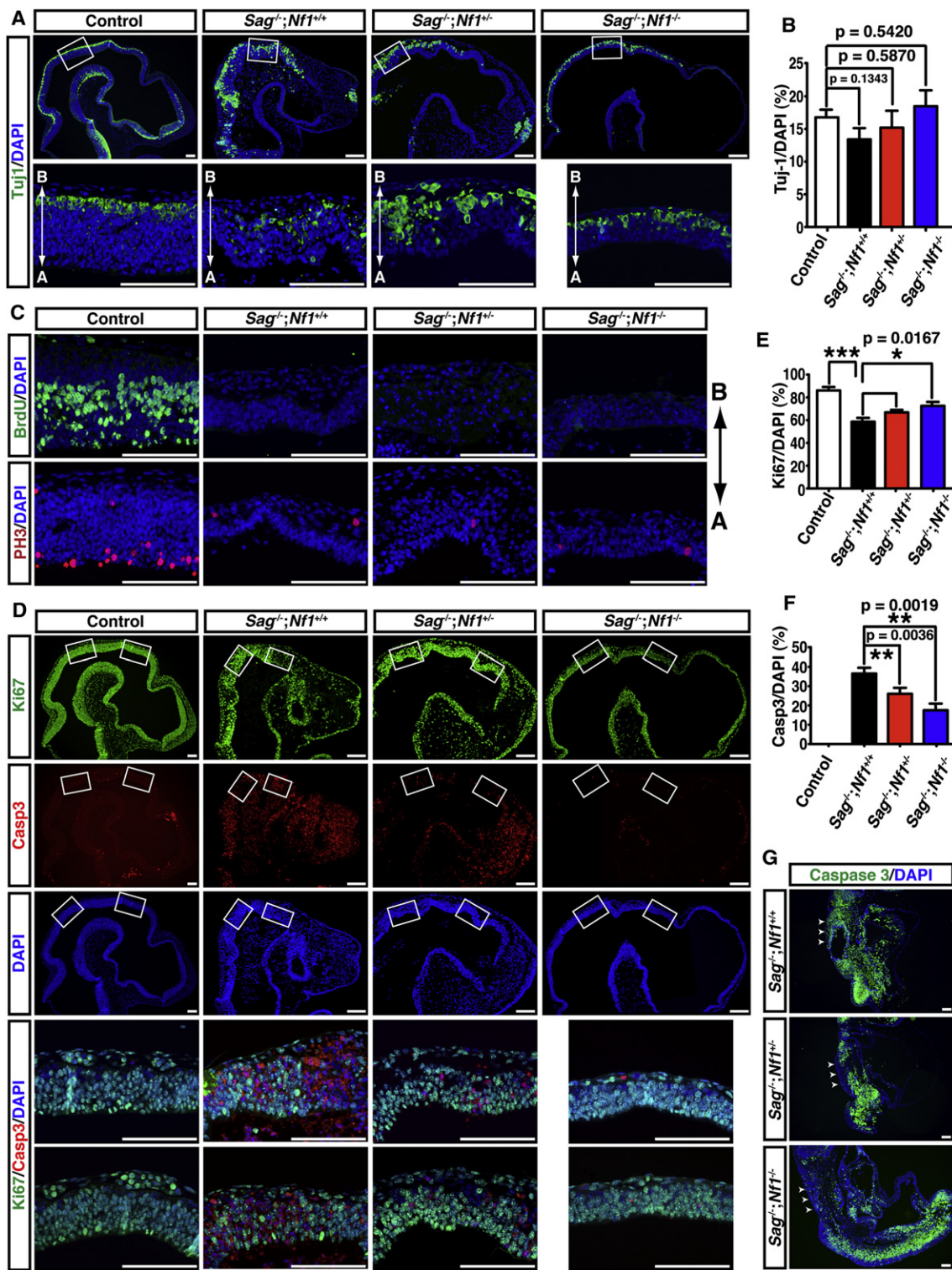


Figure 7. Inactivation of *Nf1* Partially Rescued Apoptotic Phenotype but Not Proliferation Defects in Developing Sag^{-/-} Neural Precursor Cells

(A) Neuronal differentiation detected by Tuj-1 (an early neuronal marker). Sagittal sections of embryonic brains (E10.5) with different genotypes were stained with Tuj-1 and DAPI. Scale bar represents 100 μm. A, apical; B, basal.

(B) Quantification of Tuj-1 positive cells in the neuroepithelium were normalized to total DAPI positive cells (mean ± SEM, n = 3).

(C) *Nf1* deletion failed to rescue proliferation defects in Sag^{-/-} neural precursor cells. Brain sections were stained with BrdU (an S phase marker) or Phospho-histone H3 (PH3, an M phase marker) as well as DAPI. Scale bar represents 100 μm.

et al., 2008), we demonstrate that Sag is absolutely required for mouse development. Sag disruption causes embryonic lethality at E11.5–12.5, which is associated with severe developmental defects including those in the vascular and nervous system. Because SCF E3 ligases are essential for many developmental processes (Petroski and Deshaies, 2005), it is not surprising that Sag, one of the two Rbx/Roc family members essential for E3 ligase activity, plays critical roles in many aspects of embryonic development. Although accumulation of many critical Sag/SCF-targeted substrates could contribute to severe developmental defects observed in *Sag*^{−/−} embryos, our biochemical and genetic experiments indicate a causal involvement of Nf1, which, upon accumulation as a result of Sag disruption, inactivates Ras-Mapk signals to block endothelial differentiation and induce apoptosis in the nervous system.

The RAS-MAPK signaling pathway is actively involved in cell proliferation, angiogenesis, and tumorigenesis (Dhillon et al., 2007a; Kranenburg et al., 2004) as well as endothelial specification of VEGFR2-expressing vascular progenitor cells (Kawasaki et al., 2008). Here we showed that active Ras/Erk signals are also required for endothelial differentiation of mouse ES cells. Blockade of this pathway by inhibitors of RAS (FTI-277) or MEK (PD98059) repressed ES cell differentiation into endothelial cells to form blood islands. We further showed *in vivo* that reduced Ras/Erk activation was associated with reduced angiogenesis and decreased proliferation in teratomas derived from *Sag*^{−/−} ES cells. Our mechanistic study linked Ras inactivation, upon Sag disruption, to accumulation of Nf1, a naturally occurring Ras inhibitor (Cichowski and Jacks, 2001).

Our study also defined SAG-SKP1-CUL1-FBXW7 as a physiological E3 ligase for targeted ubiquitination and degradation of NF1. First, NF1 contains an evolutionarily conserved FBXW7 binding motif at the C terminus (codons 2755–2758), which is required for FBXW7-NF1 binding and NF1 ubiquitination. Second, SAG-CUL1-FBXW7-NF1 forms a complex *in vivo* that promotes NF1 ubiquitination. Third, FBXW7 shortens NF1 protein half-life in a binding motif dependent manner, which is further promoted by SAG. Fourth, ubiquitination of exogenously expressed NF1-C is promoted by FBXW7-CUL1, but inhibited by siRNA knockdown of CUL1 or genetic deletion of FBXW7. Finally and most importantly, endogenous FBXW7 binds to endogenous NF1 under physiological conditions and SAG-CUL1-FBXW7 is required for ubiquitination and degradation of endogenous NF1 upon mitogen stimulation. Our study also demonstrates that SAG could form an active E3 complex with SKP1, FBXW7, and CUL1, in addition to well-known CUL5 (Kamura et al., 2004), for targeted degradation of NF1.

FBXW7 is a p53-dependent haploinsufficient tumor suppressor (Kimura et al., 2003; Mao et al., 2004). Similar to Sag disruption, *Fbxw7* gene ablation also causes embryonic lethality at E10.5–E11.5 with remarkable abnormalities in vascular development in the brain and yolk sac (Tetzlaff et al., 2004; Tsunematsu et al., 2004). These phenotypic similarities suggested

that Sag and *Fbxw7* might have a similar function, such as preventing Nf1 accumulation, during vascular development. However, unlike *Fbxw7* whose deletion caused accumulation of Notch-1 and Notch-4 (Masuda et al., 2010; Tetzlaff et al., 2004; Tsunematsu et al., 2004), we found that neither Notch-1 nor Notch-4 was accumulated in *Sag*^{−/−} ES, EB, or embryos (data not shown), suggesting that accumulation of Notch family proteins do not contribute to observed defects in *Sag*^{−/−} ES cells and embryos. Instead, we showed a causal involvement of Nf1 in some aspects of vascular and neural development, regulated by Sag. First, Sag is required for endothelial cell differentiation, which is Nf1 dependent. Second, Sag plays an essential role in suppressing apoptosis during embryogenesis, with a partial involvement of Nf1 in neural precursor cells in developing brains and spinal cords, but not in mesoderm-derived tissues. Third, despite the presence of a significant number of neural precursor cells in *Sag*^{−/−} neocortex, these Ki67-positive precursor cells completely lack the ability to undergo DNA replication and mitosis, which is completely independent of Nf1. It will be interesting to determine the specific stage(s) in which *Sag*^{−/−} neural precursor cells are arrested during cell cycle. These observations suggest that Nf1-independent apoptosis and cell cycle failure, potentially as a result of accumulation of other critical Sag substrates, could be the major cause for growth retarded and lethal phenotypes observed in *Sag*^{−/−}; *Nf1*^{−/−} embryos with an embryonic life not extended beyond E11.5–12.5. Nevertheless, our genetic rescue data, by demonstrating that *Nf1* inactivation rescued vascular defects, particularly at earlier developmental stages when Sag deficiency causes no overt morphological defects, strongly argue that genetic interaction between Nf1 and Sag is specific and primary to vascular development and not secondary to overall developmental retardation. Furthermore, it is worth noting that despite the presence of excessive and widespread apoptosis at E10.5, CD31-positive endothelial cells expanded proportionally from E9.5 to E10.5 in *Sag*-deficient embryos compared to controls. This observation further supports the notion that Sag/Nf1 regulatory network controls the generation of CD31-positive endothelial cells, but not subsequent proliferation or apoptosis.

In summary, our study demonstrates an *in vivo* physiological function of Sag in regulation of vascular and neural development by modulating Ras-Mapk signaling pathway through targeted degradation of Nf1. Upon induction by different stimuli (Duan et al., 1999; Gu et al., 2007a; Tan et al., 2008), SAG recruits FBXW7 and CUL1 to promote ubiquitination and degradation of NF1, thus activating RAS-ERK signals to induce differentiation and proliferation, and to suppress apoptosis during vascular and neural development, respectively (see graphical abstract). Thus, under physiological conditions, SAG regulates NF1 levels to maintain active RAS/ERK signals for effective vascular and neural development. However, under pathological condition, such as in cancer, SAG, which is overexpressed with a poor patient prognosis (Jia et al., 2010; Sasaki et al., 2001), would

(D–F) *Nf1* deletion partially rescued neural apoptosis: Sagittal sections of embryonic brains were stained with Ki67, caspase 3, and DAPI. Scale bar represents 100 μm. The number of cells expressing Ki67 and caspase3 was normalized to the total number of DAPI positive cells (**p < 0.0001, mean ± SEM, n = 3) (E and F). (G) *Nf1* deletion partially rescued apoptosis in the spinal cord, but not surrounding mesenchymal cells. Embryonic sections were stained with caspase 3 and DAPI. Arrows point to spinal cord. Scale bar represents 100 μm.

inhibit apoptosis, promote proliferation and angiogenesis (Duan et al., 1999; Gu et al., 2007b; Sun et al., 2001). SAG, therefore, could be a valid anticancer and antiangiogenesis target (Jia et al., 2010; Nalepa et al., 2006; Sun, 2006; Wei and Sun, 2010). Moreover, 40%–80% of individuals with NF1 have cognitive deficits, which are at least partially caused by loss of one allele of the NF1 gene (haploinsufficiency) in the brain (Costa et al., 2002; Cui et al., 2008; Hyman et al., 2006). Thus, targeting the SAG/FBXW7 E3 may provide an attractive therapeutic strategy to increase NF1 protein levels for treating NF1-associated diseases caused by haploinsufficiency.

EXPERIMENTAL PROCEDURES

Generation and Maintenance of ES Cell Lines with *Sag* and/or *Nf1* Disruption

Blastocysts were isolated from intercrossing of *Sag*^{+/−} mice or *Sag*^{+/−}; *Nf1*^{+/−} mice, and placed in culture on irradiated mouse embryonic feeder cells in high glucose DMEM (Invitrogen, Carlsbad, CA) supplemented with 15% FBS (Harlan, Indianapolis, IN), 0.1 mM β-mercaptoethanol (Sigma, St. Louis, MO), 10³ U/ml LIF (ESGRO, Millipore), 25 μM PD98059 (Sigma) and penicillin/streptomycin. Inner cell mass outgrowths were trypsinized and passaged until ES cell lines were established in 35 mm cell culture dishes (Hughes et al., 2007).

Whole-Mount Immunostaining on Yolk Sac and Embryos

Whole-mount CD31 immunostaining was performed on E9.5 and E10.5 yolk sacs and embryos (Shen et al., 2005). Briefly, embryos or yolk sacs were fixed in 4% PFA/PBS, dehydrated by methanol, quenched by H₂O₂, and blocked in 4% BSA. The samples were stained by incubating with anti-CD31 (rat monoclonal MEC13.3, BD Biosciences) at 4°C overnight, followed by peroxidase-conjugated secondary antibodies. The embryos were developed in 0.25% DAB with H₂O₂ in PBS, and photographed on a dissecting microscope (model S6D; Leica) with a progressive 3CCD camera (Sony).

Endothelial Differentiation of ES Cells and Whole-Mount Staining of Embryoid Bodies

Single suspended mouse ES cells were plated at density of 1 × 10⁶ cells/10 cm Petri dish containing 15% DMEM in the absence of LIF. Cells were cultured for up to 13 days with media change every other day. Embryoid bodies were first fixed in the 4% PFA, blocked with 3% milk and 0.1% Triton X-100 in PBS, and incubated with CD31 antibody overnight. After washing, the samples were incubated with secondary antibody overnight. Color was developed using DAB. The samples were then dehydrated, embedded, and sectioned. The sections were counterstained with Eosin-Y.

Immunofluorescence

Paraffin sections were deparaffinized, rehydrated, and analyzed by immunofluorescence (Wang et al., 2009; Zhu et al., 2001). Briefly, sections were incubated with primary antibodies in blocking solution overnight. The antibodies used are as follows: Ki 67 (1:500, mouse, BD Biosciences), Tuj-1 (1:500, Rabbit, Covance), Cleaved Caspase3 (1:500, Rabbit, Cell signaling), Phosphohistone H3 (1:500, Rabbit, Abcam), BrdU (1:500, Rat, Abcam), and CD31 (1:200, Mouse, Dako). The secondary antibodies were conjugates of Alexa Fluor 488 or Alexa Fluor 555 (1:500, Invitrogen). DAPI (1:1000, Invitrogen) was used as nuclear counter staining. Sections were examined under a fluorescence microscope (Olympus).

Statistical Analysis

The paired Student's t test was used for statistical analysis, using SAS software for two paired samples. A mixed model was fit to the tumor volumes (excluding mice with no tumors). Presence or absence of *Sag* knockout was included as a fixed effect. ES cell line was included as a random effect in the model to account for correlation between observations within a cell line. An F-test from the mixed model fit was used to test whether the mean value for tumors from cell lines with *Sag* knockout was the same as that for the tumors with wild-type *Sag*.

SUPPLEMENTAL INFORMATION

Supplemental Information includes six figures and Supplemental Experimental Procedures and can be found with this article online at doi:10.1016/j.devcel.2011.09.014.

ACKNOWLEDGMENTS

We thank Dr. B. Vogelstein for providing DLD-1 and HCT-116 cells with FBXW7 gene deleted and Drs. K. Nakayama and B.E. Clurman for plasmids expressing FBXW7. We also thank Dr. Matthew Schipper for his help in statistical analysis of the teratoma data. This work is supported by NCI grants CA111554, CA118762, and CA156744 to Y.S. and NS053900 and W81XWH-11-1-0251 to Y.Z.

Received: April 2, 2010

Revised: June 9, 2011

Accepted: September 26, 2011

Published online: November 23, 2011

REFERENCES

Brannan, C.I., Perkins, A.S., Vogel, K.S., Ratner, N., Nordlund, M.L., Reid, S.W., Buchberg, A.M., Jenkins, N.A., Parada, L.F., and Copeland, N.G. (1994). Targeted disruption of the neurofibromatosis type-1 gene leads to developmental abnormalities in heart and various neural crest-derived tissues. *Genes Dev.* 8, 1019–1029.

Cancer Genome Atlas Research Network. (2008). Comprehensive genomic characterization defines human glioblastoma genes and core pathways. *Nature* 455, 1061–1068.

Cichowski, K., and Jacks, T. (2001). NF1 tumor suppressor gene function: narrowing the GAP. *Cell* 104, 593–604.

Cichowski, K., Santiago, S., Jardim, M., Johnson, B.W., and Jacks, T. (2003). Dynamic regulation of the Ras pathway via proteolysis of the NF1 tumor suppressor. *Genes Dev.* 17, 449–454.

Costa, R.M., Federov, N.B., Kogan, J.H., Murphy, G.G., Stern, J., Ohno, M., Kucherlapati, R., Jacks, T., and Silva, A.J. (2002). Mechanism for the learning deficits in a mouse model of neurofibromatosis type 1. *Nature* 415, 526–530.

Cui, Y., Costa, R.M., Murphy, G.G., Elgersma, Y., Zhu, Y., Gutmann, D.H., Parada, L.F., Mody, I., and Silva, A.J. (2008). Neurofibromin regulation of ERK signaling modulates GABA release and learning. *Cell* 135, 549–560.

Deshaias, R.J., and Joazeiro, C.A. (2009). RING domain E3 ubiquitin ligases. *Annu. Rev. Biochem.* 78, 399–434.

Dhillon, A.S., Hagan, S., Rath, O., and Kolch, W. (2007a). MAP kinase signalling pathways in cancer. *Oncogene* 26, 3279–3290.

Dhillon, A.S., von Kriegsheim, A., Grindlay, J., and Kolch, W. (2007b). Phosphatase and feedback regulation of Raf-1 signaling. *Cell Cycle* 6, 3–7.

Ding, L., Getz, G., Wheeler, D.A., Mardis, E.R., McLellan, M.D., Cibulskis, K., Sougnez, C., Greulich, H., Muzny, D.M., Morgan, M.B., et al. (2008). Somatic mutations affect key pathways in lung adenocarcinoma. *Nature* 455, 1069–1075.

Donaldson, T.D., Noureddine, M.A., Reynolds, P.J., Bradford, W., and Duronio, R.J. (2004). Targeted disruption of *Drosophila* Roc1b reveals functional differences in the Roc subunit of Cullin-dependent E3 ubiquitin ligases. *Mol. Biol. Cell* 15, 4892–4903.

Duan, H., Wang, Y., Aviram, M., Swaroop, M., Loo, J.A., Bian, J., Tian, Y., Mueller, T., Bisgaier, C.L., and Sun, Y. (1999). SAG, a novel zinc RING finger protein that protects cells from apoptosis induced by redox agents. *Mol. Cell. Biol.* 19, 3145–3155.

Farkas, L.M., and Huttner, W.B. (2008). The cell biology of neural stem and progenitor cells and its significance for their proliferation versus differentiation during mammalian brain development. *Curr. Opin. Cell Biol.* 20, 707–715.

Furukawa, M., Ohta, T., and Xiong, Y. (2002). Activation of UBC5 ubiquitin-conjugating enzyme by the RING finger of ROC1 and assembly of active ubiquitin ligases by all cullins. *J. Biol. Chem.* 277, 15758–15765.

Götz, M., and Huttner, W.B. (2005). The cell biology of neurogenesis. *Nat. Rev. Mol. Cell Biol.* 6, 777–788.

Gu, Q., Tan, M., and Sun, Y. (2007a). SAG/ROC2/Rbx2 is a novel activator protein-1 target that promotes c-Jun degradation and inhibits 12-O-tetradecanoylphorbol-13-acetate-induced neoplastic transformation. *Cancer Res.* 67, 3616–3625.

Gu, Q., Bowden, G.T., Normolle, D., and Sun, Y. (2007b). SAG/ROC2 E3 ligase regulates skin carcinogenesis by stage-dependent targeting of c-Jun/AP1 and IkappaB-alpha/NF-kappaB. *J. Cell Biol.* 178, 1009–1023.

Hagan, S., Garcia, R., Dhillon, A., and Kolch, W. (2006). Raf kinase inhibitor protein regulation of raf and MAPK signaling. *Methods Enzymol.* 407, 248–259.

Henkemeyer, M., Rossi, D.J., Holmyard, D.P., Puri, M.C., Mbamalu, G., Harpal, K., Shih, T.S., Jacks, T., and Pawson, T. (1995). Vascular system defects and neuronal apoptosis in mice lacking ras GTPase-activating protein. *Nature* 377, 695–701.

Hughes, E.D., Qu, Y.Y., Genik, S.J., Lyons, R.H., Pacheco, C.D., Lieberman, A.P., Samuelson, L.C., Nasonkin, I.O., Camper, S.A., Van Keuren, M.L., and Saunders, T.L. (2007). Genetic variation in C57BL/6 ES cell lines and genetic instability in the Bruce4 C57BL/6 ES cell line. *Mamm. Genome* 18, 549–558.

Hyman, S.L., Shores, A., and North, K.N. (2005). The nature and frequency of cognitive deficits in children with neurofibromatosis type 1. *Neurology* 65, 1037–1044.

Hyman, S.L., Arthur Shores, E., and North, K.N. (2006). Learning disabilities in children with neurofibromatosis type 1: subtypes, cognitive profile, and attention-deficit-hyperactivity disorder. *Dev. Med. Child Neurol.* 48, 973–977.

Jacks, T., Shih, T.S., Schmitt, E.M., Bronson, R.T., Bernards, A., and Weinberg, R.A. (1994). Tumour predisposition in mice heterozygous for a targeted mutation in *Nf1*. *Nat. Genet.* 7, 353–361.

Jia, L., Yang, J., Hao, X., Zheng, M., He, H., Xiong, X., Xu, L., and Sun, Y. (2010). Validation of SAG/RBX2/ROC2 E3 ubiquitin ligase as an anticancer and radiosensitizing target. *Clin. Cancer Res.* 16, 814–824.

Jia, L., Bickel, J.S., Wu, J., Morgan, M.A., Li, H., Yang, J., Yu, X., Chan, R.C., and Sun, Y. (2011). RBX1 (RING box protein 1) E3 ubiquitin ligase is required for genomic integrity by modulating DNA replication licensing proteins. *J. Biol. Chem.* 286, 3379–3386.

Jin, J., Cardozo, T., Lovering, R.C., Elledge, S.J., Pagano, M., and Harper, J.W. (2004). Systematic analysis and nomenclature of mammalian F-box proteins. *Genes Dev.* 18, 2573–2580.

Kamura, T., Koepp, D.M., Conrad, M.N., Skowyra, D., Moreland, R.J., Iliopoulos, O., Lane, W.S., Kaelin, W.G., Jr., Elledge, S.J., Conaway, R.C., et al. (1999). Rbx1, a component of the VHL tumor suppressor complex and SCF ubiquitin ligase. *Science* 284, 657–661.

Kamura, T., Maenaka, K., Kotoshiba, S., Matsumoto, M., Kohda, D., Conaway, R.C., Conaway, J.W., and Nakayama, K.I. (2004). VHL-box and SOCS-box domains determine binding specificity for Cul2-Rbx1 and Cul5-Rbx2 modules of ubiquitin ligases. *Genes Dev.* 18, 3055–3065.

Karnoub, A.E., and Weinberg, R.A. (2008). Ras oncogenes: split personalities. *Nat. Rev. Mol. Cell Biol.* 9, 517–531.

Kawasaki, K., Watabe, T., Sase, H., Hirashima, M., Koide, H., Morishita, Y., Yuki, K., Sasaoka, T., Suda, T., Katsuki, M., et al. (2008). Ras signaling directs endothelial specification of VEGFR2+ vascular progenitor cells. *J. Cell Biol.* 181, 131–141.

Kimura, T., Gotoh, M., Nakamura, Y., and Arakawa, H. (2003). hCDC4b, a regulator of cyclin E, as a direct transcriptional target of p53. *Cancer Sci.* 94, 431–436.

Kolch, W. (2005). Coordinating ERK/MAPK signalling through scaffolds and inhibitors. *Nat. Rev. Mol. Cell Biol.* 6, 827–837.

Kranenburg, O., Gebbink, M.F., and Voest, E.E. (2004). Stimulation of angiogenesis by Ras proteins. *Biochim. Biophys. Acta* 1654, 23–37.

Le, L.Q., and Parada, L.F. (2007). Tumor microenvironment and neurofibromatosis type I: connecting the GAPs. *Oncogene* 26, 4609–4616.

Mao, J.H., Perez-Losada, J., Wu, D., Delrosario, R., Tsunematsu, R., Nakayama, K.I., Brown, K., Bryson, S., and Balmain, A. (2004). Fbxw7/Cdc4 is a p53-dependent, haploinsufficient tumour suppressor gene. *Nature* 432, 775–779.

Masuda, K., Ishikawa, Y., Onoyama, I., Unno, M., de Alborán, I.M., Nakayama, K.I., and Nakayama, K. (2010). Complex regulation of cell-cycle inhibitors by Fbxw7 in mouse embryonic fibroblasts. *Oncogene* 29, 1798–1809.

McGillicuddy, L.T., Fromm, J.A., Hollstein, P.E., Kubek, S., Beroukhim, R., De Raedt, T., Johnson, B.W., Williams, S.M., Nghiempuu, P., Liau, L.M., et al. (2009). Proteasomal and genetic inactivation of the NF1 tumor suppressor in gliomagenesis. *Cancer Cell* 16, 44–54.

Moore, R., and Boyd, L. (2004). Analysis of RING finger genes required for embryogenesis in *C. elegans*. *Genesis* 38, 1–12.

Nakayama, K.I., and Nakayama, K. (2006). Ubiquitin ligases: cell-cycle control and cancer. *Nat. Rev. Cancer* 6, 369–381.

Nalepa, G., Rolfe, M., and Harper, J.W. (2006). Drug discovery in the ubiquitin-proteasome system. *Nat. Rev. Drug Discov.* 5, 596–613.

Nord, A.S., Chang, P.J., Conklin, B.R., Cox, A.V., Harper, C.A., Hicks, G.G., Huang, C.C., Johns, S.J., Kawamoto, M., Liu, S., et al. (2006). The International Gene Trap Consortium Website: a portal to all publicly available gene trap cell lines in mouse. *Nucleic Acids Res.* 34 (Database issue), D642–D648.

Ohta, T., Michel, J.J., Schottelius, A.J., and Xiong, Y. (1999). ROC1, a homolog of APC11, represents a family of cullin partners with an associated ubiquitin ligase activity. *Mol. Cell* 3, 535–541.

Parsons, D.W., Jones, S., Zhang, X., Lin, J.C., Leary, R.J., Angenendt, P., Mankoo, P., Carter, H., Siu, I.M., Gallia, G.L., et al. (2008). An integrated genomic analysis of human glioblastoma multiforme. *Science* 321, 1807–1812.

Petroski, M.D., and Deshaies, R.J. (2005). Function and regulation of cullin-RING ubiquitin ligases. *Nat. Rev. Mol. Cell Biol.* 6, 9–20.

Phan, V.T., Ding, V.W., Li, F., Chalkley, R.J., Burlingame, A., and McCormick, F. (2010). The RasGAP proteins Ira2 and neurofibromin are negatively regulated by Gpb1 in yeast and ETEA in humans. *Mol. Cell. Biol.* 30, 2264–2279.

Rajagopalan, H., Jallepalli, P.V., Rago, C., Velculescu, V.E., Kinzler, K.W., Vogelstein, B., and Lengauer, C. (2004). Inactivation of hCDC4 can cause chromosomal instability. *Nature* 428, 77–81.

Reynolds, P.J., Simms, J.R., and Duronio, R.J. (2008). Identifying determinants of cullin binding specificity among the three functionally different *Drosophila melanogaster* Roc proteins via domain swapping. *PLoS ONE* 3, e2918.

Sangha, N., Wu, R., Kuick, R., Powers, S., Mu, D., Fiander, D., Yuen, K., Katauchi, H., Tashiro, H., Fearon, E.R., et al. (2008). Neurofibromin 1 (NF1) defects are common in human ovarian serous carcinomas and co-occur with TP53 mutations. *Neoplasia* 10, 1362–1372.

Sasagawa, Y., Urano, T., Kohara, Y., Takahashi, H., and Higashitani, A. (2003). *Caenorhabditis elegans* RBX1 is essential for meiosis, mitotic chromosomal condensation and segregation, and cytokinesis. *Genes Cells* 8, 857–872.

Sasaki, H., Yukie, H., Kobayashi, Y., Moriyama, S., Nakashima, Y., Kaji, M., Fukai, I., Kiriyama, M., Yamakawa, Y., and Fujii, Y. (2001). Expression of the sensitive to apoptosis gene, SAG, as a prognostic marker in nonsmall cell lung cancer. *Int. J. Cancer* 95, 375–377.

Seol, J.H., Feldman, R.M.R., Zachariae, W.Z., Shevchenko, A., Correll, C.C., Lyapina, S., Chi, Y., Galova, M., Claypool, J., Sandmeyer, S., et al. (1999). Cdc53/cullin and the essential Hrt1 RING-H2 subunit of SCF define a ubiquitin ligase module that activates the E2 enzyme Cdc34. *Genes Dev.* 13, 1614–1626.

Shen, T.L., Park, A.Y., Alcaraz, A., Peng, X., Jang, I., Koni, P., Flavell, R.A., Gu, H., and Guan, J.L. (2005). Conditional knockout of focal adhesion kinase in endothelial cells reveals its role in angiogenesis and vascular development in late embryogenesis. *J. Cell Biol.* 169, 941–952.

Sun, Y. (1999). Alterations of SAG mRNA in human cancer cell lines: requirement for the RING finger domain for apoptosis protection. *Carcinogenesis* 20, 1899–1903.

Sun, Y. (2006). E3 ubiquitin ligases as cancer targets and biomarkers. *Neoplasia* 8, 645–654.

Sun, Y., Tan, M., Duan, H., and Swaroop, M. (2001). SAG/ROC/Rbx/Hrt, a zinc RING finger gene family: molecular cloning, biochemical properties, and biological functions. *Antioxid. Redox Signal.* 3, 635–650.

Swaroop, M., Wang, Y., Miller, P., Duan, H., Jatkoe, T., Madore, S.J., and Sun, Y. (2000). Yeast homolog of human SAG/ROC2/Rbx2/Hrt2 is essential for cell growth, but not for germination: chip profiling implicates its role in cell cycle regulation. *Oncogene* 19, 2855–2866.

Tan, P., Fuchs, S.Y., Chen, A., Wu, K., Gomez, C., Ronai, Z., and Pan, Z.-Q. (1999). Recruitment of a ROC1-CUL1 ubiquitin ligase by Skp1 and HOS to catalyze the ubiquitination of I kappa B alpha. *Mol. Cell* 3, 527–533.

Tan, M., Gu, Q., He, H., Pamarthi, D., Semenza, G.L., and Sun, Y. (2008). SAG/ROC2/RBX2 is a HIF-1 target gene that promotes HIF-1 alpha ubiquitination and degradation. *Oncogene* 27, 1404–1411.

Tan, M., Davis, S.W., Saunders, T.L., Zhu, Y., and Sun, Y. (2009). RBX1/ROC1 disruption results in early embryonic lethality due to proliferation failure, partially rescued by simultaneous loss of p27. *Proc. Natl. Acad. Sci. USA* 106, 6203–6208.

Tetzlaff, M.T., Yu, W., Li, M., Zhang, P., Finegold, M., Mahon, K., Harper, J.W., Schwartz, R.J., and Elledge, S.J. (2004). Defective cardiovascular development and elevated cyclin E and Notch proteins in mice lacking the Fbw7 F-box protein. *Proc. Natl. Acad. Sci. USA* 101, 3338–3345.

Tsunematsu, R., Nakayama, K., Oike, Y., Nishiyama, M., Ishida, N., Hatakeyama, S., Bessho, Y., Kageyama, R., Suda, T., and Nakayama, K.I. (2004). Mouse Fbw7/Sel-10/Cdc4 is required for notch degradation during vascular development. *J. Biol. Chem.* 279, 9417–9423.

Wang, Y., Yang, J., Zheng, H., Tomasek, G.J., Zhang, P., McKeever, P.E., Lee, E.Y., and Zhu, Y. (2009). Expression of mutant p53 proteins implicates a lineage relationship between neural stem cells and malignant astrocytic glioma in a murine model. *Cancer Cell* 15, 514–526.

Wei, D., and Sun, Y. (2010). Small RING finger proteins RBX1 and RBX2 of SCF E3 ubiquitin ligases: the role in cancer and as cancer targets. *Genes & Cancer* 1, 700–707.

Woodruff, J.M. (1999). Pathology of tumors of the peripheral nerve sheath in type 1 neurofibromatosis. *Am. J. Med. Genet.* 89, 23–30.

Wu, K., Fuchs, S.Y., Chen, A., Tan, P., Gomez, C., Ronai, Z., and Pan, Z.Q. (2000). The SCF(HOS/beta-TRCP)-ROC1 E3 ubiquitin ligase utilizes two distinct domains within CUL1 for substrate targeting and ubiquitin ligation. *Mol. Cell. Biol.* 20, 1382–1393.

Zheng, N., Schulman, B.A., Song, L., Miller, J.J., Jeffrey, P.D., Wang, P., Chu, C., Koepf, D.M., Elledge, S.J., Pagano, M., et al. (2002). Structure of the Cul1-Rbx1-Skp1-F boxSkp2 SCF ubiquitin ligase complex. *Nature* 416, 703–709.

Zhu, Y., Romero, M.I., Ghosh, P., Ye, Z., Charnay, P., Rushing, E.J., Marth, J.D., and Parada, L.F. (2001). Ablation of NF1 function in neurons induces abnormal development of cerebral cortex and reactive gliosis in the brain. *Genes Dev.* 15, 859–876.

Zhu, Y., Guignard, F., Zhao, D., Liu, L., Burns, D.K., Mason, R.P., Messing, A., and Parada, L.F. (2005). Early inactivation of p53 tumor suppressor gene cooperating with NF1 loss induces malignant astrocytoma. *Cancer Cell* 8, 119–130.

**RAS/ERK inhibition rescues fate-specification defects of *Nf1*-deficient neural progenitors
and brain abnormalities**

Yuan Wang^{1,2}, Edward Kim^{1,2}, Xiaojing Wang^{1,2}, Bennett G. Novitch³, Kazuaki Yoshikawa⁴,
Long-Sheng Chang⁵ and Yuan Zhu^{1,2,*}

¹Division of Molecular Medicine and Genetics, Departments of Internal Medicine and ²Cell & Developmental Biology, University of Michigan Medical School, Ann Arbor, MI 48109;

³Department of Neurobiology, Eli and Edythe Broad Center of Regenerative Medicine and Stem Cell Research, David Geffen School of Medicine at University of California at Los Angeles, Los Angeles, CA 90095; ⁴Institute for Protein Research, Osaka University, Suita, Osaka 565-0871, Japan; ⁵Department of Pediatrics, Nationwide Children's Hospital and The Ohio State University, Columbus, OH 43205

Running title: The role of *Nf1* in maintaining postnatal SVZ neurogenesis

Key words: Neurofibromatosis type 1, NF1, tumor suppressor gene, neural stem cells, glial cells, subventricular zone (SVZ).

*Author for correspondence:

Yuan Zhu, Ph.D.

Phone: (734) 647-3033

Fax: (734) 763-2162

E-mail: yuanzhu@umich.edu

SUMMARY

Germline mutations in the RAS/ERK signaling pathway underlie several related developmental disorders collectively termed neuro-cardio-facial-cutaneous (NCFC) syndromes. Patients with these disorders manifest varying degrees of cognitive impairment, but the developmental basis of their brain abnormalities remains largely unknown. Among NCFC syndromes, neurofibromatosis type 1 (NF1) is an exception, as it is caused by loss-of-function heterozygous mutations. Here, we show that bi-allelic *Nf1* inactivation promotes Erk-dependent, ectopic Olig2 expression specifically in transit-amplifying progenitors, leading to increased gliogenesis at the expense of neurogenesis in neonatal and adult subventricular zone (SVZ). *Nf1*-deficient brains exhibit enlarged corpus callosum - a structural brain defect recently linked to severe learning deficits in NF1 patients. Strikingly, these NF1-associated developmental defects are rescued by transient treatment with an MEK/ERK pathway inhibitor during neonatal stages. These studies reveal a critical role for *Nf1* in maintaining postnatal SVZ-derived neurogenesis, and identify a potential therapeutic window for treating NF1-associated brain abnormalities.

INTRODUCTION

RAS genes are the key intracellular mediators that transmit signals from cell surface receptors to downstream effector pathways, regulating cell proliferation, survival and differentiation (Bos, 1989; Downward, 2003). One of the major RAS-regulated downstream effector pathways is mediated by the extracellular-signal regulated kinase (ERK) subfamily of mitogen-activated protein kinases (MAPK), which is comprised of a kinase cascade of RAF, MEK and ERK (Rubinfeld and Seger, 2005). Somatic activating mutations in RAS and RAF are among the most frequent gain-of-function alterations in human cancer, highlighting a critical role for the RAS-RAF-MEK-ERK pathway in human oncogenesis (Bos, 1989; Downward, 2003). Recent studies have revealed that germline mutations in the components of the RAS/ERK pathway are associated with a group of clinically related developmental disorders including Noonan, LEOPARD, cardio-facio-cutaneous (CFC), Costello, Legius and neurofibromatosis type 1 (NF1) syndromes, which has been collectively referred to as neuro-cardio-facio-cutaneous (NCFC) syndromes or “RASopathies” (Bentires-Alj et al., 2006; Samuels et al., 2009; Schubbert et al., 2007; Tidyman and Rauen, 2009). One of the most important unknown aspects of NCFC syndromes is the mechanism(s) underlying the substantial neurocognitive burden of these diseases. Particularly, the developmental basis of brain abnormalities in NCFC syndrome patients remains largely unknown.

Most NCFC syndromes are caused by dominant activating mutations in the RAS/ERK signaling pathway in the germline. However, NF1 is arguably an exception, as it is caused by germline recessive loss-of-function mutations in one of the two *NF1* alleles (*NF1*^{+/−}) (Bentires-Alj et al., 2006; Samuels et al., 2009; Schubbert et al., 2007; Tidyman and Rauen, 2009). The *NF1* gene encodes a RAS GTPase activating protein (GAP) neurofibromin, which promotes the conversion of an active RAS-GTP bound form to an inactive RAS-GDP form, thus functioning as a negative regulator of RAS/ERK signaling (Cichowski and Jacks, 2001). Between 30-70% of NF1 patients have learning disabilities - the most significant cause of lifetime morbidity associated with these patients (Hyman et al., 2005). Recent studies using genetically engineered mouse (GEM) models have shown that heterozygous *Nf1* inactivation (*Nf1*^{+/−}) causes behavioral abnormalities with similarities to learning disabilities in NF1 patients (Cui et al., 2008). However, *Nf1*^{+/−} mice exhibit no evidence of structural brain defects such as enlarged corpus callosum (CC), which has

been recently associated with severe learning disabilities observed in a subpopulation of NF1 patients (Moore et al., 2000; Pride et al., 2010). The CC is comprised of neuronal fibers that connect the two brain hemispheres, as well as the two primary glial cell types, oligodendrocytes that form myelin of axons and astrocytes that provide trophic and functional support for neurons (Rowitch and Kriegstein, 2010). The clinical observations that only a subpopulation of NF1 patients exhibit an enlarged CC argue that mono-allelic *NF1* inactivation (*NF1*^{+/−}) is not sufficient to induce these structural brain defects. It has recently been shown that some NF1-related non-tumor manifestations such as skin hyperpigmentation and bone abnormalities result from bi-allelic *NF1* inactivation (*NF1*^{−/−}) caused by “second-hit” mutations in the remaining wild-type *NF1* alleles of somatic cells (De Schepper et al., 2008; Stevenson et al., 2006). Accordingly, we hypothesize that the structural brain defects such as the enlarged CC observed in a subset of NF1 patients could be caused by bi-allelic *NF1* inactivation in developing neural stem cells. Compared to other cells, stem cells have greater potentials for self-renewal and consequently, one or few *NF1*^{−/−} stem cells could produce a greater number of progeny that manifest clinical symptoms (Kriegstein and Alvarez-Buylla, 2009). Therefore, NF1-associated structural brain abnormalities may provide a unique opportunity to define the timing and cellular targets of somatic “second-hit” *NF1* mutations and more importantly, the phenotypic consequences of hyperactive RAS/ERK signaling in developing stem cell lineages underlying these brain abnormalities.

Most glial cells in the CC arise from neural progenitor cells that are specified by a basic helix-loop-helix transcription factor, Olig2, in the subventricular zone (SVZ) of the lateral ventricle during perinatal stages (Marshall et al., 2005; Richardson et al., 2006; Rowitch and Kriegstein, 2010). Olig2 is both sufficient and necessary for specifying SVZ progenitors to adopt glial fates. Olig2 promotes their differentiation to both oligodendrocytes and astrocytes during neonatal stages, but only to oligodendrocytes in adulthood (Cai et al., 2007; Hack et al., 2005; Marshall et al., 2005; Menn et al., 2006). Loss of Olig2 leads to a nearly complete absence of glial cells including both oligodendrocytes and astrocytes in the postnatal CC (Cai et al., 2007). During mouse embryonic development, the SVZ initially is comprised of neuron-restricted progenitors, also known as transit-amplifying progenitors or intermediate progenitor cells (TAP/IPC), which express Tbr2 and give rise to excitatory projection neurons in the cerebral cortex from embryonic

day 14.5-17.5 (E14.5-17.5) (Molyneaux et al., 2007). When neurogenesis ceases at E17.5 in the cerebral cortex, gliogenesis ensues and persists into postnatal stages. However, one multipotent neural stem cell population with neurogenic activity in the SVZ persists into adulthood and this region forms the largest germinal zone in the adult brain (Ihrie and Alvarez-Buylla, 2011; Kriegstein and Alvarez-Buylla, 2009). The SVZ stem cell lineage is organized in a hierarchy: type B cells (SVZ-B) are multipotent stem cells expressing glial fibrillary acidic protein (GFAP), which give rise to type C cells (SVZ-C) that are multipotent TAP/IPC_s. The SVZ-C TAP/IPC_s subsequently differentiate into two lineage-restricted progenitors: (1) neuron-restricted type A neuroblasts (SVZ-A) that migrate along rostral migratory stream (RMS) and differentiate into inhibitory neurons in the olfactory bulb (OB) and (2) glia-restricted progenitors that migrate and differentiate into glial cells populating the overlying CC (Ihrie and Alvarez-Buylla, 2011; Kriegstein and Alvarez-Buylla, 2009). The cellular output of neonatal and adult SVZ stem and progenitor cells is dramatically different. While neonatal SVZ cells simultaneously produce a large number of neurons and glial cells in the OB and CC, respectively, adult SVZ cells predominately generate neurons in the OB (>90%) (Hack et al., 2005; Marshall et al., 2005; Menn et al., 2006). The mechanism(s) by which postnatal SVZ stem and progenitor cells suppress Olig2 expression and maintain high levels of neurogenesis in an otherwise gliogenic environment of the postnatal brain is not well understood.

RESULTS

Bi-allelic inactivation of *Nf1* leads to an enlarged corpus callosum

To determine whether bi-allelic inactivation of *Nf1* leads to structural brain defects observed in a subpopulation of NF1 patients, we targeted an *Nf1* conditional mutation into radial glia by using a Cre transgenic strain under the control of the human GFAP promoter (hGFAP-cre) (Zhu et al., 2001; Zhuo et al., 2001). During embryonic development, radial glia are the primary neural stem cell populations, which give rise to neurons, glia, and adult neural stem cells in the SVZ (Kriegstein and Alvarez-Buylla, 2009). The onset of hGFAP-cre expression occurs in ~95% of E12/13 radial glia in the forebrain, thus inactivating *Nf1* in both embryonic and adult neural stem cells as well as their differentiated progeny (Malatesta et al., 2003). *Nf1* conditional knockout mice with the genotypes of hGFAP-cre+;*Nf1*^{flx/flx} or hGFAP-cre+;*Nf1*^{flx/-} were referred to as *Nf1*^{hGFAP}CKO (*Nf1*^{-/-}), as both genotypes showed similar phenotypes analyzed in this study.

Germline (*Nf1*^{+/−}) or conditional (hGFAP-cre+; *Nf1*^{flox/+}) heterozygous mice exhibited no overt structural or cellular defects in the brain, indicating that mono-allelic *Nf1* inactivation is not sufficient to induce the structural brain defects observed in human NF1 patients. In contrast, *Nf1* conditional bi-allelic inactivation caused a 10-15% increase in the size of cerebral cortical surface area, a manifestation often observed in human NF1 patients (Figure 1A, B). We next measured and compared the size of the CC at three different sagittal positions along the midline to lateral hemisphere of control and *Nf1*^{hGFAP}CKO brains at 2 months of age (Figure 1C, C'). At all three positions that are directly associated with the SVZ of the lateral ventricle (P₁-P₃), *Nf1* inactivation caused a significant increase in the thickness of the CC (Figure 1D, E; S1A-C). Of note, the CC from the midline section, which is not directly associated with the SVZ, showed no increase in thickness (Figure 1E; S1D). These observations demonstrate that bi-allelic, but not heterozygous, inactivation of *Nf1* leads to an enlarged CC specifically associated with the SVZ.

To determine the mechanism underlying the enlarged CC, we first examined whether there was an increase in the number of neurons in the cerebral cortex that project their axons to the CC (Molyneaux et al., 2007; Richards et al., 2004). The number of NeuN⁺ cortical neurons, Ctip2⁺ deep- or Cux1⁺ upper-layer neurons was not significantly different between control and *Nf1*^{hGFAP}CKO brains (Figure S1E-E''). Second, we examined whether there was an increase in the number of axons in the *Nf1*^{hGFAP}CKO CC. From the coronal sections, we confirmed that the enlargement of the CC occurred specifically in the areas directly associated with the SVZ, but not in the midline (Figure 1F; S1F, F'). Compared to controls, neurofilament 200 (NF200, an axonal marker) staining revealed a more diffused and reduced expression pattern in the *Nf1*^{hGFAP}CKO CC (Figure 1F). At the ultrastructural level, only a marginal, but not statistically significant, increase in the number of axons was observed in the *Nf1*^{hGFAP}CKO CC compared to that of controls (Figure 1H-J; S1G, H). In contrast, the number of cell bodies was significantly increased on the same sections analyzed by electron microscopy (EM) (Figure 1K). Consistently, a robust increase in both the absolute number and density of cells in the SVZ-associated CC of *Nf1*^{hGFAP}CKO brains was observed on thicker sections compared to controls (Figure 1D, L; S1A-C). The increased number in GFAP⁺ and Olig2⁺ glial lineage cells appeared to be the major contributing factor for the increased cellular density (Figure 1M-O). Together, these results suggest that an increase in the number of glial cells, but not the number of axons or cortical

neurons, is mainly responsible for the enlarged SVZ-associated CC in *Nf1*^{hGFAP}CKO brains. In support of this conclusion, no CC alteration was observed in neuron-specific *Nf1* conditional knockout mice driven by Synapsin I-cre (Figure S1F") (Zhu et al., 2001). It is worth noting that despite relatively normal appearance of myelination (Figure 1G), varying degrees of tissue degeneration was observed in the CC of *Nf1*^{hGFAP}CKO brains (Figure 1I).

***Nf1*-deficient adult brain exhibits an enlarged SVZ with increased glial differentiation**

Despite a disproportionately enlarged SVZ-associated CC, one discernible structural difference between control and *Nf1*^{hGFAP}CKO forebrains was the significantly reduced size of the OB, the destination of SVZ-derived neurons (Figure 1A, A'). The opposite size alterations observed in the two brain structures related to SVZ-derived gliogenesis and neurogenesis raise the possibility that these phenotypes could result from functional impairments of *Nf1*-deficient SVZ stem and progenitor cells. We therefore analyzed the SVZ from these mice at the same three positions used for the CC studies. At each of these three positions, *Nf1*^{hGFAP}CKO SVZ exhibited a 2- to 3-fold size increase compared to controls (Figure 2Aa-b", 2B; S2A-C). To investigate the relative contribution of SVZ cells to its increased size, we determined the number of individual SVZ cell populations by using lineage markers. Compared to controls, the percentage of SVZ cells expressing glial-lineage markers including GFAP, Olig2 and NG2 was markedly increased with a concomitant reduction in Doublecortin (Dcx)-expressing neuroblasts in the *Nf1*^{hGFAP}CKO SVZ (Figure 2Ac-h', 2C). Furthermore, a greater number of GFAP⁺ cells accumulated and formed a less cellular area in the anterior-dorsal part of the *Nf1*^{hGFAP}CKO SVZ, which was not identified in the control SVZ (dotted areas in Figure 2Ab'', 2Ad,d'; S2A). These GFAP⁺ cells exhibited the features of differentiated astrocytes including the presence of multiple long cellular processes, and a lack of expression of stem/progenitor marker Nestin or Ki67 (Figure 2Ad, S3A). Together, these results demonstrate that *Nf1* inactivation leads to an enlarged SVZ with accumulation of differentiated glial cells.

***Nf1* inactivation impairs the balance of glial versus neuronal output in the adult SVZ**

Abnormally increased numbers of glial lineage cells observed in the *Nf1*^{hGFAP}CKO SVZ/CC system could result from an increase in proliferation or a reduction in apoptosis of SVZ stem and/or progenitor cells as expected from loss of *Nf1* tumor suppressor function. To investigate

this possibility, we performed an *in vivo* bromodeoxyuridine (BrdU) labeling assay and *in vitro* neurosphere assays (Figure S3 and see Supplemental text for details). These studies demonstrate that alterations in proliferation or apoptosis in adult *Nf1*^{hGFAP}CKO SVZ unlikely contribute to increased glial lineage cells in the enlarged SVZ. We next investigated whether *Nf1* inactivation altered glial versus neuronal fate-specification by examining Olig2 expression in the SVZ stem cell lineages. No Olig2 expression was observed in GFAP⁺ SVZ-B stem cells or lineage-restricted Dcx⁺ SVZ-A neuroblasts in the adult control or *Nf1*^{hGFAP}CKO SVZ (Figure S2E and data not shown). Previous studies showed that Ascl1⁺ progenitor cells in the embryonic and neonatal SVZ selectively express the Dlx1/2 homeodomain transcription factors and Olig2, directing neural stem and progenitor cells to adopt neuronal and glial fates, respectively (Marshall et al., 2005; Parras et al., 2004; Petryniak et al., 2007). Consistent with the previous studies indicating that glial output of adult SVZ stem cells is minor (5-10%) (Hack et al., 2005; Menn et al., 2006), approximately 9% of multipotent Ascl1⁺ TAP/IPC expressed Olig2 in the control adult SVZ (Figure 2D-F). Strikingly, nearly half of Ascl1⁺ TAP/IPC expressed Olig2 in the *Nf1*^{hGFAP}CKO SVZ (48.3%, Figure 2D-F). These results are most consistent with a model wherein *Nf1* inactivation promotes ectopic expression of Olig2 specifically in SVZ-C TAP/IPC that normally undergo neuronal differentiation, leading to an increased output of glial cells at the expense of neuronal differentiation. This hypothesis is supported by the observation that *Nf1* inactivation leads to an enlarged CC with a concomitant reduction in OB size.

To further test this hypothesis, we performed a long-term BrdU pulse-chase experiment on 2-month-old control and *Nf1*^{hGFAP}CKO mice. Thirty days after BrdU pulses, we analyzed the number and the identity of newly generated SVZ-derived BrdU⁺ cells in the SVZ/RMS/OB/CC system. Compared to control brains, there was a more than two-fold increase of BrdU⁺ cells in the SVZ/RMS/CC and surrounding areas of *Nf1*^{hGFAP}CKO brains (Figure 3A, B). All of the BrdU⁺ cells in the CC of both control and *Nf1*^{hGFAP}CKO brains expressed Olig2, but not other lineage markers including GFAP, Pax6 or Dcx (Figure 3C and data not shown). The rate of proliferation or apoptosis of Olig2⁺ cells was not significantly different between the control and mutant CC (Figure 3D, D' and data not shown). These results indicate that the increase of glial cells in the *Nf1*^{hGFAP}CKO CC is unlikely contributed by locally increased proliferation or reduced apoptosis in the mutant CC. Strikingly, we observed a 9-fold increase of BrdU⁺ cells in the

Nf1^{hGFAP}CKO RMS compared to controls (Figure 3E, F). While a small number of BrdU⁺ cells observed in the control RMS were Pax6- or Dcx-expressing migrating neuroblasts, over half of the BrdU⁺ populations in the *Nf1*^{hGFAP}CKO RMS expressed Olig2 or GFAP (Figure 3E-G). Consistently, a nearly 3-fold increase in Olig2- and NG2-expressing cells was observed in the *Nf1*^{hGFAP}CKO RMS, some of which expressed myelin basic protein (MBP) (Figure S4A-C). The abnormal myelination in the mutant RMS may contribute to the progressive disruption of neuronal migratory chain over time (Figure S4D). Consistently, Pax6⁺/BrdU⁺ migrating neuroblasts were accumulated and significantly increased in the *Nf1*^{hGFAP}CKO RMS compared to controls (Figure 3E, F). In contrast to a marked increase in gliogenesis in the CC and RMS, the number of BrdU⁺ cells in the OB of *Nf1*^{hGFAP}CKO mice was greatly reduced compared to controls (Figure 3A). Most of the BrdU⁺ cells in the control OB were newly generated NeuN⁺ neurons, which were reduced by 50% in the mutant OB (Figure 3H, H'). No significant difference in the BrdU⁺/NeuN⁻ populations was observed, indicating that local gliogenesis in the OB was not affected by *Nf1* inactivation. Taken together, these observations demonstrate that *Nf1* plays a critical role in regulating glial versus neuronal output in the adult SVZ stem cell niche by suppressing Olig2 expression in Ascl1⁺ SVZ-C TAP/PCPs.

Acute inactivation of *Nf1* is sufficient to induce glial/neuronal fate switch in the adult SVZ

To determine whether abnormal glial/neuronal fate-specification reflects an ongoing cell-autonomous requirement for *Nf1* function in adult SVZ progenitors or abnormal SVZ niche environment, we employed an inducible system in which Cre recombinase (Nestin-cre^{ER}) can be activated in Nestin-expressing cells by tamoxifen (TM) treatment (Figure S5) (Burns et al., 2007). To target adult SVZ cells, we established a 5-day TM induction protocol from postnatal day 26 (P26) to P30 (Figure 4A). TM-induced Nestin-cre^{ER}-mediated recombination specifically targets neural stem and progenitor cells in the SVZ as well as neuroblasts in the RMS, but not the CC or OB of the adult brain (Figure 4B). This genetic approach allowed us to perform long-term lineage-tracing analysis for SVZ-derived glial cells in the CC and neurons in the OB, as no cells in these two structures were directly targeted by this Nestin-cre^{ER} transgene (Figure 4O). We injected TM into control and *Nf1*^{NcreER}CKO mice from P26 to P30, and analyzed the distribution and identity of Nestin-cre^{ER}-targeted SVZ/RMS-derived cells one month later. At P60, the number of control and *Nf1*-deficient SVZ cells, marked by β-gal expression, was not

significantly different between TM-treated control and *Nf1*^{NcreER}CKO mice (Figure 4C, D). Moreover, the percentage of proliferating BrdU⁺ cells in the β-gal⁺ cell populations of the control and *Nf1*^{NcreER}CKO SVZ was also comparable, confirming that *Nf1* inactivation confers no growth advantage to adult SVZ cells (Figure 4E, F). However, the percentage of β-gal⁺ cells expressing Olig2 was greatly increased, indicating that acute inactivation of *Nf1* in the normal SVZ niche is sufficient to induce ectopic expression of Olig2 in adult SVZ cells (Figure 4G, H). Consistently, β-gal⁺ cells that all expressed Olig2 were dramatically increased and often formed clusters in the CC of TM-treated *Nf1*^{NcreER}CKO brains (Figure 4C, D, I, J). Together, these results demonstrate that acute *Nf1* inactivation promotes ectopic Olig2 expression in adult SVZ cells, and subsequently enhances SVZ-derived gliogenesis in the CC.

Consistent with the notion of the *Nf1*-deficiency dependent glial/neuronal fate switch, the number of β-gal⁺ cells in the RMS was significantly reduced in TM-induced *Nf1*^{NcreER}CKO brains (Figure 4D). Moreover, a subpopulation of the β-gal⁺ cells expressed Olig2 in the mutant RMS whereas all the β-gal⁺ cells in the control RMS were Dcx⁺/Olig2⁻ neuroblasts (Figure 4K, L). These results suggest that *Nf1* inactivation not only increases SVZ-derived gliogenesis in the CC, but also alters the migratory pattern of some glial progenitor cells that abnormally enter into the RMS. Since it requires about 14 days for a neuroblast to complete its migration from the SVZ to OB (Ihrie and Alvarez-Buylla, 2011), the β-gal⁺ neuroblasts observed in the RMS 30 days after TM induction would be exclusively derived from multipotent neural stem and progenitor cells in the SVZ (Figure 4K). In contrast, a considerable number of β-gal⁺ neurons in the OB were derived from Nestin-cre^{ER}-targeted neuroblasts in the RMS. Thus, a 2-fold decrease in the number of SVZ-derived neuroblasts in the mutant RMS opposed to a marginal reduction in SVZ-derived neurogenesis in the mutant OB could reflect the fact that *Nf1* has a dispensable role in neuroblast migration and differentiation (Figure 4M-O). Collectively, these observations demonstrate that acute inactivation of *Nf1* confers no proliferative advantage to adult SVZ cells, but instead alters glial/neuronal fate-specification by promoting Olig2 expression in adult SVZ progenitor cells in a cell-autonomous manner.

Nf1 suppresses Olig2 expression in neonatal SVZ progenitor cells

Despite an ongoing requirement for *Nf1* function in regulating fate-specification of adult SVZ progenitor cells, acute inactivation of *Nf1* in adult SVZ cells did not produce any of the structural defects (e.g., enlarged CC or SVZ) observed in *Nf1*^{hGFAP}CKO brains. We therefore sought to investigate the timing and mechanism(s) by which *Nf1* inactivation leads to impaired fate-specification of SVZ cells and enlarged CC during development. We measured the size and cell number of the anterior SVZ (SVZa) and posterior SVZ (SVZp), and no significant difference was identified between control and *Nf1*^{hGFAP}CKO forebrains at birth (Figure 5Aa, a'; Figure S6A, D). The overall rate of proliferation or apoptosis in the SVZ was not significantly altered (Figure S6B, C). Compared to controls, however, one striking phenotype observed was a nearly 3-fold increase in the number of cells that expressed Olig2 in the *Nf1*^{hGFAP}CKO SVZa (Figure 5Ab,b', 5B). No increase in the percentage of Ki67⁺ proliferating cells in the Olig2⁺ lineage was observed, indicating that Olig2⁺ cells were not hyperproliferative in the *Nf1*^{hGFAP}CKO SVZa (Figure 5C, D). Given no alteration in proliferation or apoptosis observed in the *Nf1*^{hGFAP}CKO SVZa, we investigated the possibility of whether *Nf1* inactivation leads to ectopic Olig2 expression in SVZa stem and progenitor cells in neonatal brains. Although the number of Ascl1⁺ cells was comparable between control and *Nf1*^{hGFAP}CKO SVZa ($p = 0.104$), the percentage of Olig2-expressing cells in Ascl1⁺ populations (Olig2^{+/}Ascl1⁺) was greatly increased from 16.7% in controls to 38.7% in mutants (Figure 5E, F). Concomitantly, the Dlx2^{+/}Ascl1⁺ progenitor populations were reduced from 82.5% to 65.3% (Figure 5E, F). Moreover, the percentage of Ascl1⁺ cells that expressed both Olig2 and Dlx2 was increased from 5.5% to 11.8% (Figure 5Eb, b', 5F). These observations suggest that similar to its role in the adult SVZ, *Nf1* inactivation promotes ectopic Olig2 expression in Ascl1⁺ SVZ progenitors in neonatal stages. Similarly, *Nf1* inactivation leads to ectopic Olig2 expression in the SVZp, which suppresses Dlx2 expression as these cells become more differentiated and migrate to the IZ, leading to overproduction of Olig2⁺ lineage cells at the expense of the Dlx2⁺ lineages (Figure 5G, H; S6E-K and see Supplemental text for details).

***Nf1*-related structural brain defects are established during neonatal development**

We observed no significant difference in the size of control and *Nf1*^{hGFAP}CKO brains including OB at P0.5 and P8 (Figure 6A-C). However, by P18, the size of the mutant OB was significantly reduced to a similar degree as that observed in the adult (Figure 6D; S8E). Notably, neuronal

clusters, which could be readily identified in the control OB, were largely absent in mutants (Figure 6E). These observations suggest that the glial/neuronal fate-specification defect caused by *Nf1* inactivation is largely established during postnatal stages from P8 to P18. To test this, we pulsed control and *Nf1*^{hGFAP}CKO mice with BrdU at P8, and analyzed the BrdU-treated mice at P18. SVZ-derived newborn neurons labeled by BrdU and NeuN (BrdU⁺/NeuN⁺) were markedly reduced in the *Nf1*^{hGFAP}CKO OB compared to controls (Figure 6E-G). It is worth noting that the number of BrdU⁺ cells coexpressing the neuronal-lineage marker Pax6 was not significantly different between the control and *Nf1*^{hGFAP}CKO RMS (Figure S7A, B). This observation suggests that in contrast to adulthood, the reduced neurogenesis in the neonatal mutant OB is unlikely contributed by migratory defects in the RMS. Compared to controls, the number of BrdU⁺ cells was increased by more than 3-fold in the *Nf1*^{hGFAP}CKO RMS and CC, where most of the BrdU⁺ cells expressed glial markers, GFAP and Olig2 (Figure 6H-J; S7B-D). These observations demonstrate that *Nf1* inactivation leads to increased gliogenesis at the expense of neurogenesis in the neonatal SVZ/RMS/OB/CC system. Interestingly, the ratio of newly generated GFAP⁺/BrdU⁺ astrocytes and Olig2⁺/BrdU⁺ oligodendrocytes was not significantly different in the CC of control and *Nf1*^{hGFAP}CKO brains, indicating that *Nf1* inactivation only promotes overproduction of Olig2⁺ progenitors, but does not alter the potential of these Olig2⁺ progenitors to differentiate into astrocytes or oligodendrocytes (Figure 6K) (Cai et al., 2007; Marshall et al., 2005). It is worth noting that the size and cell number of *Nf1*^{hGFAP}CKO SVZ was already significantly enlarged at P8, and this was accompanied by a transient increase in proliferation of GFAP⁺ stem cells, but not Olig2⁺ cells (Figure 6L-R and see Supplemental text for details). Taken together, these results demonstrate that ectopic expression of Olig2 in Ascl1⁺ progenitors caused by *Nf1* inactivation manifests during neonatal stages (Figure 6R), leading to increased gliogenesis in the CC at the expense of neurogenesis in the OB. Consequently, Nf1-related structural brain defects including enlarged CC and reduced OB are both established during early postnatal stages.

Neonatal Erk pathway inhibition rescues structural brain defects caused by *Nf1* inactivation

To investigate the molecular mechanism underlying ectopic Olig2 expression in *Nf1*-deficient SVZ progenitors, we performed a series of in vitro and in vivo experiments. We showed that activation of Erk signaling pathway, but not phosphatidylinositol 3-kinase (PI3K)/Akt or

mammalian target of rapamycin complex 1 (mTORC1), was associated with ectopic Olig2 expression in Ascl1⁺ TAP/IPCs (Figure S8A-C and see Supplemental text for details). These results suggest that *Nf1*-mediated negative regulation of Erk signaling suppresses Olig2 expression and consequently, glial fates in neurogenic Ascl1⁺ TAP/IPCs. To test this model, we treated mice from P0.5-P18 with a potent MEK/ERK pathway inhibitor (MEKi), PD0325901 (Sebolt-Leopold and Herrera, 2004). Despite relatively normal at birth, *Nf1*^{hGFAP}CKO mice became hunched, scruffy and exhibited growth retardation within a week. Consequently, *Nf1*^{hGFAP}CKO mice can be readily identified from control littermates from P8 on, and weighed only half as much as control littermates by P18 (Figure 7A, B). Strikingly, this P0.5-P18 treatment protocol completely rescued these phenotypes. For example, the appearance of the MEKi-treated *Nf1*^{hGFAP}CKO mice was indistinguishable from control littermates at P18 (Figure 7A). In the brain, the level of Erk activation in MEKi-treated *Nf1*^{hGFAP}CKO mice at P18 was reduced to the level of control SVZ and more importantly, the number of Olig2⁺ cells in the mutant SVZ was rescued to the level of vehicle-treated controls (Figure 7C-C’). For the Ascl1⁺ progenitors, the percentage of Olig2⁺ cells in MEKi-treated *Nf1*^{hGFAP}CKO SVZ was also reduced to control levels (Figure 7C’). In the CC, the density of Olig2⁺ cells and GFAP⁺ cells in MEKi-treated *Nf1*^{hGFAP}CKO brains, albeit not completely rescued, was reduced to nearly the levels of vehicle-treated controls (Figure 7D-D’). Most importantly, the enlarged CC phenotype was completely rescued in the MEKi-treated *Nf1*^{hGFAP}CKO brains (Figure 7D, D’). Conversely, neuronal density and the size of the OB were significantly increased in mutants after MEKi treatment, particularly evidenced by the reappearance of neuronal clusters that were only observed in the control OB (Figure 7E, E’; S8E-E’). These MEKi treatment experiments demonstrate a potential therapeutic window for preventing and treating NF1-associated structural brain defects.

DISCUSSION

Given the well-documented role of ERK activity in synaptic transmission and memory formation, pharmacological intervention of RAS/ERK signaling could provide an attractive therapeutic strategy to ameliorate the substantial neurocognitive burden associated with the NCFC syndromes (Davis and Laroche, 2006; Samuels et al., 2009). However, it is unclear to what degree development-related structural brain abnormalities contribute to the cognitive

deficits in NCFC syndrome patients. Recent studies have revealed that the structural brain abnormalities, particularly, an enlarged CC, are identified in a subpopulation of NF1 patients with severe learning disabilities (Moore et al., 2000; Payne et al., 2010; Pride et al., 2010). These observations provide strong support for the hypothesis that these structural brain abnormalities could be responsible for the severe forms of cognitive impairment observed in a subset of NCFC patients. Thus, our study elucidates the timing, cellular and molecular mechanism(s) by which hyperactive RAS/ERK signaling leads to the development-related structural brain defects caused by bi-allelic *Nf1* inactivation. More importantly, we demonstrate the neonatal stage(s) as a critical therapeutic window for treating these brain abnormalities.

Bi-allelic inactivation as an NF1-related non-tumor disease mechanism

The mechanism underlying the extremely high level of variability in disease manifestation among NF1 patients, even for those with the same germline heterozygous mutations, is poorly understood (Riccardi, 1992). Our study demonstrates that bi-allelic, but not heterozygous, inactivation of *Nf1* leads to structural brain defects including enlarged CC. Moreover, our study shows that bi-allelic inactivation of *Nf1* in developing, but not adult, neural stem cells, results in an enlarged CC. The results are consistent with the observations that (1) most glial cells in the CC are generated by SVZ stem cells during perinatal stages, and (2) only a minor population of the progeny derived from adult SVZ stem cells contribute to glial cells in the CC (Marshall et al., 2005; Richardson et al., 2006; Rowitch and Kriegstein, 2010). Therefore, these observations suggest that the timing and cellular target(s) of somatic “second-hit” events could profoundly impact on the severity of disease manifestations, thus providing a potential mechanism underlying high levels of disease variability observed among NF1 patients. It has been well established that benign and malignant tumors arising in NF1 patients result from bi-allelic inactivation of *NF1* (Cichowski and Jacks, 2001). *NF1*^{-/-} tumor cells exhibit growth advantage, leading to clonal expansion and thus clinically identifiable diseases in NF1 patients. Similarly, because of the substantial self-renewal capacities possessed by developing stem and progenitor cell populations, a relatively small number of somatic “second-hit” events in these cells could produce a greater number of *NF1*^{-/-} progeny, leading to more severe phenotypic consequences than those with the “second-hit” events in differentiated cells. It would be of particular interest to determine whether somatic “second-hit” *NF1* mutations indeed occur in cells within the enlarged

CC from human specimens, as previously demonstrated in other NF1-related non-tumor lesions including skin hyperpigmentation and bone abnormalities (De Schepper et al., 2008; Stevenson et al., 2006). Alternatively, a subset of *NF1*^{+/−} cells could phenotypically behave like *NF1*^{−/−} cells when they have aberrantly high activity of a recently identified ubiquitin-mediated NF1 degradation machinery (Tan et al., 2011).

The role *Nf1* in SVZ stem and progenitor cells in the brain

During embryonic development, neurogenesis and gliogenesis are temporally regulated and occur sequentially in the developing VZ and SVZ (Kriegstein and Alvarez-Buylla, 2009; Molyneaux et al., 2007). Recent studies using the same hGFAP-cre driver show that Erk1 and Erk2 double knockout mice exhibit a significantly thinner VZ and SVZ and a reduction in the size of the CC, and Erk2 loss results in reduced proliferation of SVZ TAP/IPC s during embryonic cortical development (Samuels et al., 2008; Satoh et al., 2011). These mouse genetic studies support the notion that ERK/Erk signaling pathway has an essential role in both human and mouse embryonic cortical development. However, our study shows that *Nf1* has a dispensable role in embryonic cortical development. Specifically, the number of deep- and upper-layer neurons as well as laminar organization of the cerebral cortex appears to be relatively normal in *Nf1*^{hGFAP}CKO brains. In the neonatal and adult SVZ, neurogenesis and gliogenesis occur simultaneously (Kriegstein and Alvarez-Buylla, 2009). Our study indicates that the percentage of Ascl1⁺ TAP/IPC s expressing Olig2 is highly correlated with the glial output of neonatal and adult SVZ stem cell niches, ~20% and ~9%, respectively. This observation is consistent with previous studies showing that the regulation of Olig2 expression in the Ascl1⁺ TAP/IPC compartment appears to be a critical mechanism controlling the balance between gliogenesis and neurogenesis in the postnatal SVZ stem cell niche (Cai et al., 2007; Hack et al., 2005; Marshall et al., 2005; Menn et al., 2006). Although Olig2 expression is activated by sonic hedgehog (Shh) signaling in developing ventral spinal cord and forebrain, the signaling pathway(s) regulating Olig2 is relatively less understood in the dorsal forebrain (Lagace et al., 2007; Lu et al., 2000; Zhou et al., 2000). In cultured neural precursor cells, fibroblast growth factor 2 (FGF2) promotes Olig2 expression in an Erk-dependent, but Shh-independent manner (Bilican et al., 2008; Chandran et al., 2003; Kessaris et al., 2004). In light of these in vitro studies, our study provides compelling in vivo evidence supporting that *Nf1*-regulated Erk

signaling plays a critical role in regulating Olig2 in both neonatal and adult SVZ cells. Based on these observations, we propose that FGF-mediated Ras/Erk signaling pathway induces Olig2 expression, triggering the transition from neurogenesis to gliogenesis at the end of cortical development. The critical role of Nf1 is to inhibit Ras/Erk activity and in turn suppress Olig2 expression in a subset of Ascl1⁺ TAP/IPCs, thereby ensuring persistent neurogenesis in otherwise gliogenic environment of the perinatal and adult brain (Figure 7F). This model is supported by the observations that hyperactivative Erk signaling and ectopic Olig2 expression in *Nfl*^{hGFAP}CKO brains are almost exclusively observed in SVZ-C Ascl1⁺ TAP/IPCs, but not in any other SVZ lineage cells. Thus, our study demonstrates that the regulation of Erk signaling pathway by Nf1 mainly occurs at the stages of SVZ TAP/IPC cells. It is worth noting that Nf1 has functions that are critical for glia and neurons in the other regions of the brain (Hegedus et al., 2007; Lee da et al., 2010; Zhu et al., 2005). Together, these studies suggest that individual ERK pathway components (e.g. NF1) may be rate-limiting only in specific cell types and/or during specific developmental stages, and this could contribute to phenotypic heterogeneity among NCFC syndromes.

Clinical implication – a therapeutic window of opportunity

The most striking finding of this study is the robust therapeutic response when an 18-day MEKi treatment protocol was delivered to neonatal *Nfl*^{hGFAP}CKO mice, which suffer from structural brain defects (e.g., enlarged CC and reduced OB), weight loss to deteriorating health. Remarkably, this MEKi treatment protocol not only rescues SVZ-associated glial versus neuronal fate-specification defects and the size abnormalities observed in the CC and OB, but also dramatically improve the overall health of *Nfl*^{hGFAP}CKO mice (Figure 7A). These observations suggest that Nf1-related brain pathologies are mainly caused by hyperactivation of the Erk/MAPK signaling pathway, but not other Ras-mediated signaling pathways (e.g., PI3K/Akt). Furthermore, clinical studies indicate that optic nerve gliomas only develop in younger NF1 children (<6 years) and that nearly half of plexiform neurofibromas are identified in NF1 children younger than 5 years (Listernick et al., 1999; Waggoner et al., 2000). Taken together, we propose that this transient MEKi treatment protocol during early postnatal stages might represent an exciting opportunity to prevent and treat various NF1-associated tumor and non-tumor manifestations including structural brain defects, which are associated with severe

learning disabilities and are previously thought to be “irreversible” due to their hypothetical origin during embryonic development.

EXPERIMENTAL PROCEDURES

Control and Mutant Mice

The control mice used in this study are a pool of phenotypically indistinguishable mice with genotypes of hGFAP-cre-;*Nf1*^{flox/flox}, hGFAP-cre-;*Nf1*^{flox/+}, hGFAP-cre+;*Nf1*^{flox/+} and hGFAP-cre±;*Nf1*^{KO/+}. The mutant mice (*Nf1*^{hGFAP}CKO) used were of the genotypes, hGFAP-cre+;*Nf1*^{flox/KO} and hGFAP-cre+;*Nf1*^{flox/flox}. For inducible experiments, Nestin-cre^{ER}+;*Nf1*^{flox/+} (tamoxifen+) mice were used as controls while Nestin-cre^{ER}+;*Nf1*^{flox/flox} (tamoxifen+) mice were used as mutants (*Nf1*^{NcreER}CKO). Both of inducible strains carry R26^{LacZR} allele as a reporter. *Nf1*^{hGFAP}CKO and control mice were maintained in the mixed backgrounds of C57Bl6, 129Svj and FVB, which improve overall health and lifespan of the mutant mice. Nestin-cre^{ER}+;*Nf1*^{flox/flox} and control mice were maintained on the mixed C57Bl6 and 129Svj backgrounds. Age- and littermate-matched control and mutant mice were used for analysis to minimize the impact of modifier genes. All mice in this study were cared for according to the guidelines that were approved by the Animal Care and Use Committees of the University of Michigan at Ann Arbor.

MEK Inhibitor Treatment

MEK inhibitor (PD0325901, Sigma) was dissolved in DMSO at a concentration of 25mg/ml and resuspended in vehicle (0.5% hydroxypropyl methyl-cellulose with 0.2% Tween80, Sigma) at a concentration of 1mg/ml. The solution was administered by oral gavage at the dosage of 5 mg/kg (body weight) daily to lactating females for the treatment of P0.5-P18 mice. MEK inhibitor treated mice were collected and compared to littermate control and *Nf1*^{hGFAP}CKO mice treated with vehicle.

Histological, Molecular and Statistical Analyses

Detailed descriptions for the experimental procedures are provided in the Supplemental Experimental Procedures.

ACKNOWLEDGEMENTS

We thank M. Best, L. Cregan and G. Tomasek for technical assistance; members of the Zhu lab for support; J. Harrison, D. Sorenson, S. Meshinchi at the MIL core facility for EM analysis; A. Messing for providing hGFAP-cre mice; and Dr. H. Song, D. Wellik, K.S. O'Shea, J. Sebolt-Leopold, E. Fearon for critically reading the manuscript. This work is supported by grants from the NIH (1R01 NS053900) and DOD (W81XWH-11-1-0251) (Y.Z.).

REFERENCES

Bentires-Alj, M., Kontaridis, M.I., and Neel, B.G. (2006). Stops along the RAS pathway in human genetic disease. *Nature medicine* 12, 283-285.

Bilican, B., Fiore-Heriche, C., Compston, A., Allen, N.D., and Chandran, S. (2008). Induction of Olig2 precursors by FGF involves BMP signalling blockade at the Smad level. *PLoS One* 3, e2863.

Bos, J.L. (1989). ras oncogenes in human cancer: a review [published erratum appears in Cancer Res 1990 Feb 15;50(4):1352]. *Cancer Res* 49, 4682-4689.

Burns, K.A., Ayoub, A.E., Breunig, J.J., Adhami, F., Weng, W.L., Colbert, M.C., Rakic, P., and Kuan, C.Y. (2007). Nestin-CreER mice reveal DNA synthesis by nonapoptotic neurons following cerebral ischemia hypoxia. *Cereb Cortex* 17, 2585-2592.

Cai, J., Chen, Y., Cai, W.H., Hurlock, E.C., Wu, H., Kernie, S.G., Parada, L.F., and Lu, Q.R. (2007). A crucial role for Olig2 in white matter astrocyte development. *Development* 134, 1887-1899.

Chandran, S., Kato, H., Gerrelis, D., Compston, A., Svendsen, C.N., and Allen, N.D. (2003). FGF-dependent generation of oligodendrocytes by a hedgehog-independent pathway. *Development* 130, 6599-6609.

Cichowski, K., and Jacks, T. (2001). NF1 tumor suppressor gene function: narrowing the GAP. *Cell* 104, 593-604.

Cui, Y., Costa, R.M., Murphy, G.G., Elgersma, Y., Zhu, Y., Gutmann, D.H., Parada, L.F., Mody, I., and Silva, A.J. (2008). Neurofibromin regulation of ERK signaling modulates GABA release and learning. *Cell* 135, 549-560.

Davis, S., and Laroche, S. (2006). Mitogen-activated protein kinase/extracellular regulated kinase signalling and memory stabilization: a review. *Genes, brain, and behavior* 5 Suppl 2, 61-72.

De Schepper, S., Maertens, O., Callens, T., Naeyaert, J.M., Lambert, J., and Messiaen, L. (2008). Somatic mutation analysis in NF1 cafe au lait spots reveals two NF1 hits in the melanocytes. *J Invest Dermatol* 128, 1050-1053.

Downward, J. (2003). Targeting RAS signalling pathways in cancer therapy. *Nat Rev Cancer* 3, 11-22.

Hack, M.A., Saghatelyan, A., de Chevigny, A., Pfeifer, A., Ashery-Padan, R., Lledo, P.M., and Gotz, M. (2005). Neuronal fate determinants of adult olfactory bulb neurogenesis. *Nat Neurosci* 8, 865-872.

Hegedus, B., Dasgupta, B., Shin, J.E., Emnett, R.J., Hart-Mahon, E.K., Elghazi, L., Bernal-Mizrachi, E., and Gutmann, D.H. (2007). Neurofibromatosis-1 regulates neuronal and glial cell differentiation from neuroglial progenitors in vivo by both cAMP- and Ras-dependent mechanisms. *Cell stem cell* 1, 443-457.

Hyman, S.L., Shores, A., and North, K.N. (2005). The nature and frequency of cognitive deficits in children with neurofibromatosis type 1. *Neurology* 65, 1037-1044.

Ihrie, R.A., and Alvarez-Buylla, A. (2011). Lake-front property: a unique germinal niche by the lateral ventricles of the adult brain. *Neuron* 70, 674-686.

Kessaris, N., Jamen, F., Rubin, L.L., and Richardson, W.D. (2004). Cooperation between sonic hedgehog and fibroblast growth factor/MAPK signalling pathways in neocortical precursors. *Development* 131, 1289-1298.

Kriegstein, A., and Alvarez-Buylla, A. (2009). The glial nature of embryonic and adult neural stem cells. *Annu Rev Neurosci* 32, 149-184.

Lagace, D.C., Whitman, M.C., Noonan, M.A., Ables, J.L., DeCarolis, N.A., Arguello, A.A., Donovan, M.H., Fischer, S.J., Farnbauch, L.A., Beech, R.D., *et al.* (2007). Dynamic contribution of nestin-expressing stem cells to adult neurogenesis. *J Neurosci* 27, 12623-12629.

Lee da, Y., Yeh, T.H., Emnett, R.J., White, C.R., and Gutmann, D.H. (2010). Neurofibromatosis-1 regulates neuroglial progenitor proliferation and glial differentiation in a brain region-specific manner. *Genes & Development* 24, 2317-2329.

Listernick, R., Charrow, J., and Gutmann, D.H. (1999). Intracranial gliomas in neurofibromatosis type 1. *Am J Med Genet* 89, 38-44.

Lu, Q.R., Yuk, D., Alberta, J.A., Zhu, Z., Pawlitzky, I., Chan, J., McMahon, A.P., Stiles, C.D., and Rowitch, D.H. (2000). Sonic hedgehog-regulated oligodendrocyte lineage genes encoding bHLH proteins in the mammalian central nervous system. *Neuron* 25, 317-329.

Malatesta, P., Hack, M.A., Hartfuss, E., Kettenmann, H., Klinkert, W., Kirchhoff, F., and Gotz, M. (2003). Neuronal or glial progeny: regional differences in radial glia fate. *Neuron* 37, 751-764.

Marshall, C.A., Novitch, B.G., and Goldman, J.E. (2005). Olig2 directs astrocyte and oligodendrocyte formation in postnatal subventricular zone cells. *J Neurosci* 25, 7289-7298.

Menn, B., Garcia-Verdugo, J.M., Yaschine, C., Gonzalez-Perez, O., Rowitch, D., and Alvarez-Buylla, A. (2006). Origin of oligodendrocytes in the subventricular zone of the adult brain. *J Neurosci* 26, 7907-7918.

Molyneaux, B.J., Arlotta, P., Menezes, J.R., and Macklis, J.D. (2007). Neuronal subtype specification in the cerebral cortex. *Nature reviews Neuroscience* 8, 427-437.

Moore, B.D., 3rd, Slopis, J.M., Jackson, E.F., De Winter, A.E., and Leeds, N.E. (2000). Brain volume in children with neurofibromatosis type 1: relation to neuropsychological status. *Neurology* 54, 914-920.

Parras, C.M., Galli, R., Britz, O., Soares, S., Galichet, C., Battiste, J., Johnson, J.E., Nakafuku, M., Vescovi, A., and Guillemot, F. (2004). Mash1 specifies neurons and oligodendrocytes in the postnatal brain. *The EMBO journal* 23, 4495-4505.

Payne, J.M., Moharir, M.D., Webster, R., and North, K.N. (2010). Brain structure and function in neurofibromatosis type 1: current concepts and future directions. *Journal of neurology, neurosurgery, and psychiatry* 81, 304-309.

Petryniak, M.A., Potter, G.B., Rowitch, D.H., and Rubenstein, J.L. (2007). Dlx1 and Dlx2 control neuronal versus oligodendroglial cell fate acquisition in the developing forebrain. *Neuron* 55, 417-433.

Pride, N., Payne, J.M., Webster, R., Shores, E.A., Rae, C., and North, K.N. (2010). Corpus callosum morphology and its relationship to cognitive function in neurofibromatosis type 1. *J Child Neurol* 25, 834-841.

Riccardi, V.M. (1992). Neurofibromatosis: Phenotype, Natural History, and Pathogenesis, Second Edition edn (Baltimore and London, Johns Hopkins University Press).

Richards, L.J., Plachez, C., and Ren, T. (2004). Mechanisms regulating the development of the corpus callosum and its agenesis in mouse and human. *Clinical genetics* 66, 276-289.

Richardson, W.D., Kessaris, N., and Pringle, N. (2006). Oligodendrocyte wars. *Nature reviews Neuroscience* 7, 11-18.

Rowitch, D.H., and Kriegstein, A.R. (2010). Developmental genetics of vertebrate glial-cell specification. *Nature* 468, 214-222.

Rubinfeld, H., and Seger, R. (2005). The ERK cascade: a prototype of MAPK signaling. *Mol Biotechnol* 31, 151-174.

Samuels, I.S., Karlo, J.C., Faruzzi, A.N., Pickering, K., Herrup, K., Sweatt, J.D., Saitta, S.C., and Landreth, G.E. (2008). Deletion of ERK2 mitogen-activated protein kinase identifies its key roles in cortical neurogenesis and cognitive function. *J Neurosci* 28, 6983-6995.

Samuels, I.S., Saitta, S.C., and Landreth, G.E. (2009). MAP'ing CNS development and cognition: an ERKsome process. *Neuron* 61, 160-167.

Satoh, Y., Kobayashi, Y., Takeuchi, A., Pages, G., Pouyssegur, J., and Kazama, T. (2011). Deletion of ERK1 and ERK2 in the CNS causes cortical abnormalities and neonatal lethality: Erk1 deficiency enhances the impairment of neurogenesis in Erk2-deficient mice. *The Journal of neuroscience : the official journal of the Society for Neuroscience* 31, 1149-1155.

Schubbert, S., Shannon, K., and Bollag, G. (2007). Hyperactive Ras in developmental disorders and cancer. *Nature reviews Cancer* 7, 295-308.

Sebolt-Leopold, J.S., and Herrera, R. (2004). Targeting the mitogen-activated protein kinase cascade to treat cancer. *Nature reviews Cancer* 4, 937-947.

Stevenson, D.A., Zhou, H., Ashrafi, S., Messiaen, L.M., Carey, J.C., D'Astous, J.L., Santora, S.D., and Viskochil, D.H. (2006). Double inactivation of NF1 in tibial pseudarthrosis. *American journal of human genetics* 79, 143-148.

Tan, M., Zhao, Y., Kim, S.J., Liu, M., Jia, L., Saunders, T.L., Zhu, Y., and Sun, Y. (2011). SAG/RBX2/ROC2 E3 Ubiquitin Ligase Is Essential for Vascular and Neural Development by Targeting NF1 for Degradation. *Developmental cell* 21, 1062-1076.

Tidyman, W.E., and Rauen, K.A. (2009). The RASopathies: developmental syndromes of Ras/MAPK pathway dysregulation. *Current opinion in genetics & development* 19, 230-236.

Waggoner, D.J., Towbin, J., Gottesman, G., and Gutmann, D.H. (2000). Clinic-based study of plexiform neurofibromas in neurofibromatosis 1. *Am J Med Genet* 92, 132-135.

Zhou, Q., Wang, S., and Anderson, D.J. (2000). Identification of a novel family of oligodendrocyte lineage-specific basic helix-loop-helix transcription factors. *Neuron* 25, 331-343.

Zhu, Y., Harada, T., Liu, L., Lush, M.E., Guignard, F., Harada, C., Burns, D.K., Bajenaru, M.L., Gutmann, D.H., and Parada, L.F. (2005). Inactivation of NF1 in CNS causes increased glial progenitor proliferation and optic glioma formation. *Development* 132, 5577-5588.

Zhu, Y., Romero, M.I., Ghosh, P., Ye, Z., Charnay, P., Rushing, E.J., Marth, J.D., and Parada, L.F. (2001). Ablation of NF1 function in neurons induces abnormal development of cerebral cortex and reactive gliosis in the brain. *Genes Dev* 15, 859-876.

Zhuo, L., Theis, M., Alvarez-Maya, I., Brenner, M., Willecke, K., and Messing, A. (2001). hGFAP-cre transgenic mice for manipulation of glial and neuronal function in vivo. *Genesis* 31, 85-94.

FIGURE LEGENDS

Figure 1. *Nf1*-deficient adult brain exhibits enlarged corpus callosum and reduced olfactory bulb. (A, A'), B) Whole-mount images and size quantification of control and *Nf1*^{hGFAP}CKO brains and OB. (C, C') Schematic demonstration of different histological planes used for analysis and the SVZ/RMS/CC/OB system and the orientation of brains analyzed (A, anterior; P, posterior; D, dorsal; V, ventral). (D) Sagittal sections from control and *Nf1*^{hGFAP}CKO brains at 2 months were analyzed at P₂ position, stained with hematoxylin & eosin (H&E) and imaged at 3 increasingly higher magnifications. The cells that form chain-like structures (arrowheads) were exclusively observed in the mutant CC. (E) The thickness of the control and mutant CC was quantified. (F, G) Coronal sections from control and mutant brains were stained with NF200/Olig2 and MBP/Olig2. Lower panels in (F) are the high magnification view of delineated CC areas in the upper panels. (H, I) Ultrathin sections were subjected to EM analysis from dorsal to ventral CC. Representative EM images from two histological planes are shown in (H) and (I). * indicates degenerating tissues only observed in the mutant CC. (J, K) Two sets of EM images covering the entire thickness of the CC at two parallel positions (column 1 and column 2) at comparable histological planes were analyzed. The total number of axons (J) and cell bodies (K) in each column from 3 controls and 3 mutants were quantified. (L) Total cell density in the CC was quantified and compared at P₁, P₂, P₃ and M positions based on H&E-stained sections. (M) Control and mutant CC were stained for GFAP/Olig2, and their density was quantified in (N). The number of cells expressing both GFAP and Olig2 (arrows, M) was significantly increased in mutant CC (O). Dashed lines delineate the border of the CC. All the quantification data are presented as mean ± SEM. LV, *, lateral ventricle. Scale bars: 50 μm except for (H) and (I) at 2 μm. See also Figure S1.

Figure 2. *Nf1*^{hGFAP}CKO SVZ shows increased glial differentiation and ectopic Olig2 expression in Ascl1⁺TAP/IPC s.

(A) Representative sections of the control and mutant SVZ at P₂ position were stained with H&E and imaged at 3 magnifications (a-b''). The high magnification views of the boxed area in (a) and (b) are shown in (a', a'') and (b', b''), respectively. Adjacent sections were stained for Nestin/GFAP (c, d), Olig2/NG2 (e, f) and GFAP/Dcx (g, h). Arrows identify Olig2⁺/NG2⁺ cells and arrowheads mark Olig2⁺/NG2⁻ cells (e-f'). (B) The number of cells per unit length of LV at

P₁-P₃ was quantified. (C) The percentage of SVZ cells expressing different lineage markers (Ach') was quantified. (D, E) Olig2/Dlx2/Ascl1 triple immunofluorescence labeling was performed on sections from control and mutant brains. In the ventral (D) and dorsal (E) SVZa, Olig2⁺/Dlx2⁺/Ascl1⁺ triple-positive cells (white) and Olig2⁺/Dlx2⁻/Ascl1⁺ double-positive cells (pink) are marked by arrows and arrowheads, respectively. (F) The percentage of Ascl1⁺ cells expressing Olig2 and/or Dlx2 was quantified and compared between the control and mutant SVZ. All the quantification data are presented as mean ± SEM. LV and *, lateral ventricle. St, striatum. Scale bars: 50 μm. See also Figures S2 and S3.

Figure 3. *Nf1* inactivation leads to increased gliogenesis in the CC at the expense of neurogenesis in the OB.

A BrdU pulse-chase assay from P60-P90 was performed to label newly differentiated neurons and glia. (A) Low magnification view and (B) the quantification of the overall distribution of BrdU⁺ cells in P90 control and mutant brains. Arrows identify BrdU⁺ cells in the CC and arrowheads mark the abnormal increase of BrdU⁺ cells in the mutant RMS. The dashed line marks the border of the OB and the forebrain. (C) Increased Olig2⁺/BrdU⁺ cells (arrows) were observed in the mutant CC compared to controls. (D, D') A short-term BrdU proliferation assay was performed on P60 mice. (E) 30 days after BrdU pulse, the identity of BrdU⁺ cells in the RMS was revealed by triple or double labeling of BrdU with Pax6/GFAP (a, b), Dcx/GFAP (c, d), or Olig2 (e, f). Arrows and arrowheads: BrdU double- and single-labeling cells. (F, G) The number and ratio of BrdU⁺ cells that coexpressed Pax6, GFAP or Olig2 in the control and mutant RMS was quantified. (H) Sections of the control and mutant OB were stained for BrdU, NeuN and DAPI. The number of BrdU⁺/NeuN⁺ (arrows) and BrdU⁺/NeuN⁻ cells per OB surface area was quantified in (H'). All the quantification data are presented as mean ± SEM. *, lateral ventricle. Scale bars: 50 μm. See also Figure S4.

Figure 4. Acute inactivation of *Nf1* induces a glia/neuron fate switch in the adult SVZ.

(A) The summary of the genotypes of inducible mouse models and the time frame of tamoxifen (TM) induction and analysis. (B) Young adult mice were induced by TM from P26-P30 and analyzed at P31. The cells undergoing Cre-mediated recombination revealed by X-gal staining were restrictedly distributed in the SVZ and RMS. (C-N) Control and mutant brains induced by

TM from P26-P30 were analyzed at P60. (C) X-gal staining of the SVZ/RMS/CC system shows the cluster of β -gal⁺ cells (dashed lines) exclusively identified in the mutant CC. Arrowheads identify individual β -gal⁺ cells in the CC. (D) The number of β -gal⁺ cells in the control and mutant SVZ/RMS/CC was quantified. (E, F) The proliferation rate of β -gal⁺ cells marked by BrdU staining was not significantly different between the control and mutant SVZ. (G-L) The β -gal⁺ cells coexpressing Olig2 in the control and mutant SVZ (G, H), CC (I, J) and RMS (K, L) are identified by arrows and quantified. Arrowheads label non-colocalizing cells. The inset in (K) shows the coexpression of β -gal and Dcx in the control RMS. Dashed lines delineate the SVZ and/or RMS region. (M) The OB from TM-induced control and *NfI*^{NcreER}CKO brains was stained with X-gal and compared. The number of β -gal⁺ cells was quantified (N). (O) An illustration summarizes the cell lineages targeted by Nestin-cre^{ER} and their respective derivatives. All the quantification data are presented as mean \pm SEM. LV, lateral ventricle. Scale bars: 50 μ m. See also Figure S5.

Figure 5. *NfI* inactivation leads to ectopic expression of Olig2 in neural stem/progenitor cells in neonatal brains.

(A) Sections from P0.5 control and *NfI*^{hGFAP}CKO brains were stained with H&E (a, a') and Olig2 (b, b'). (B) The percentage of Olig2⁺ cells in the anterior SVZ (SVZa) was quantified. (C, D) The proliferation rate of Olig2⁺ cells was not significantly different between the control and mutant SVZa. Arrows and arrowheads: Olig2⁺/Ki67⁺ and Olig2⁺/Ki67⁻ cells. (E, F) The percentage of Ascl1⁺ cells coexpressing Olig2 and/or Dlx2 in the control and mutant SVZa was analyzed and quantified. Arrows and arrowheads: Olig2⁺/Dlx2⁺/Ascl1⁺ triple-positive cells and Olig2⁺/Dlx2⁻/Ascl1⁺ double-positive cells. (G, H) The expression of Olig2 and Dlx2 in the posterior control and mutant VZ/SVZ and IZ was analyzed and quantified. Dashed lines demarcate the SVZa (A, C, E) or VZ/SVZ regions from the IZ (G). All the quantification data are presented as mean \pm SEM. LV and *, lateral ventricle. IZ, intermediate zone. Scale bars: 50 μ m. See also Figure S6.

Figure 6. Reduced neurogenesis is accompanied by increased gliogenesis in *NfI*^{hGFAP}CKO brains during neonatal SVZ development.

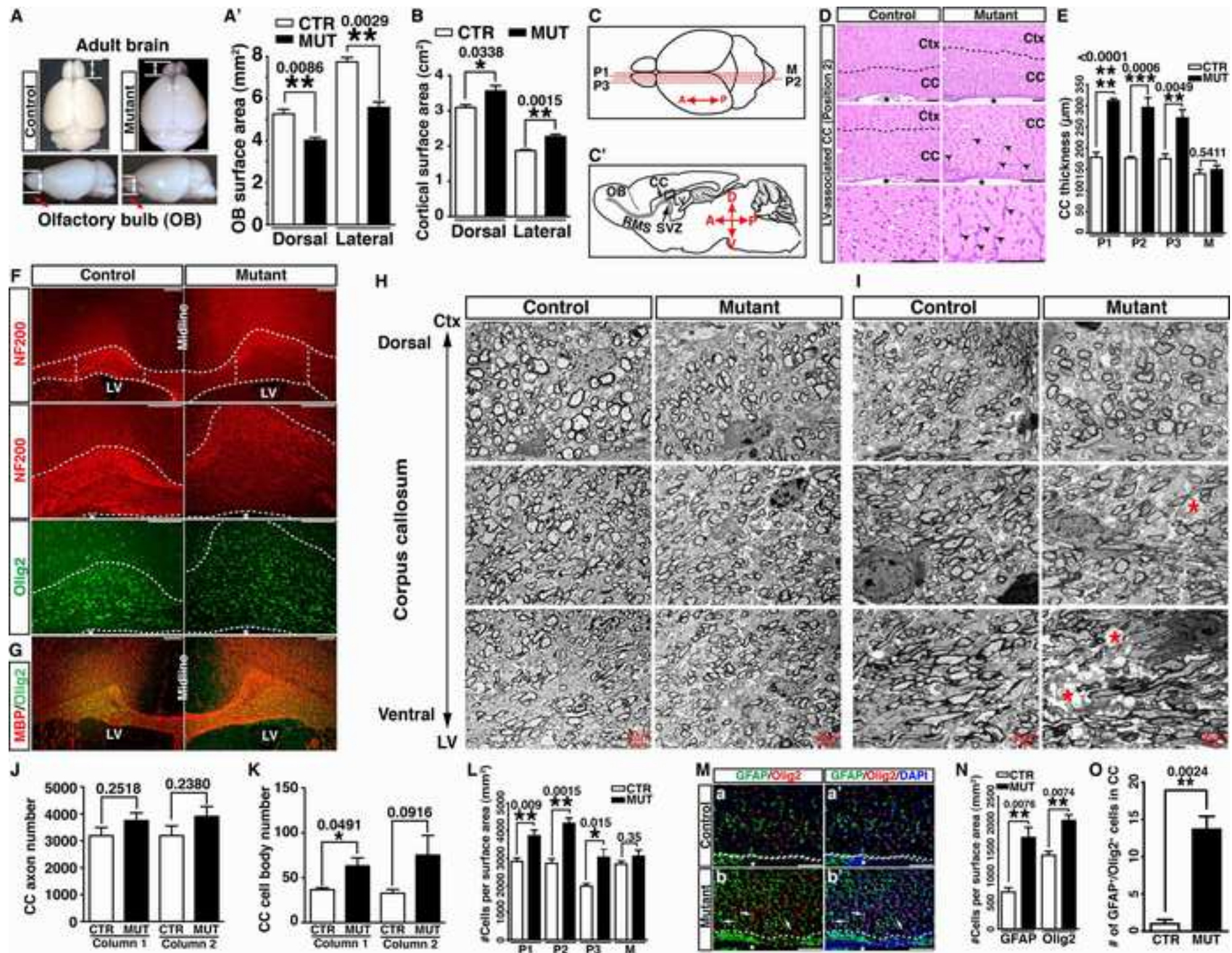
(A-C) The size of P0.5 (A) and P8 (B) control and mutant OB was measured and quantified from the dorsal view and the lateral view. (D) The size of P18 control and *Nfl*^{hGFAP}CKO OB was quantified. (E-K) Control and *Nfl*^{hGFAP}CKO mice were pulsed with BrdU at P8 and analyzed at P18. (E, F) SVZ-derived neurogenesis was analyzed and quantified by BrdU/NeuN double labeling (arrows) in the granule cell layer (GCL) and periglomerular layer (PGL) of the OB. (G) The density of NeuN⁺ cells in the OB was quantified. (H-K) The number of newly generated astrocytes (BrdU⁺/GFAP⁺) and oligodendrocytes (BrdU⁺/Olig2⁺) in the control and mutant CC are illustrated (H, I, arrows) and quantified (J). Arrowheads label non-colocalizing cells. (K) Quantification of the proportion of GFAP⁺ versus Olig2⁺ cells in the total BrdU⁺ cell population in the control and mutant CC. (L, M) Proliferating GFAP⁺ cells are shown (arrows) and quantified in the control and mutant SVZa at P8. (N, O) The quantification of total cells and the percentage of Ki67⁺ proliferating cells are shown for P8 control and mutant SVZ. (P, Q) proliferating Olig2⁺ (Olig2⁺/Ki67⁺, arrows) and differentiated Olig2⁺/Ki67⁻ (arrowheads) cells were shown and quantified in control and mutant P8 SVZa. Dashed lines demarcate the SVZ/RMS. (R) Quantification and characterization of Ascl1⁺ cells in P8 SVZa based on their expression of Olig2 and/or Dlx2. All the quantification data are presented as mean ± SEM. *, lateral ventricle. Scale bars: 1 mm (A, B); 50 μm (E-P). See also Figure S7.

Figure 7. Neonatal MEKi treatment rescues brain abnormalities caused by *Nfl* inactivation.
(A) Control and *Nfl*^{hGFAP}CKO mice were treated with vehicle and MEKi from P0.5-P18 and analyzed at P18. (B) The body weight of treated control and mutant mice was quantified. (C) Triple labeling of p-Erk/Olig2/Ascl1 was performed on brain sections of vehicle-treated control and *Nfl*^{hGFAP}CKO as well as MEKi-treated *Nfl*^{hGFAP}CKO mice. Arrows and arrowheads: Olig2⁺/Ascl1⁺ and Olig2⁺/Ascl1⁻ cells. Of note, p-Erk⁺/Olig2⁺/Ascl1⁺ cells were only identified in vehicle-treated mutants. (C', C'') The number of p-Erk⁺ cells and the percentage of Olig2⁺ cells among total SVZ Ascl1⁺ cells were quantified among vehicle and MEKi-treated control and mutant mice. (D) GFAP/Olig2 double-labeling of the CC from treated control and mutant mice was performed. Dashed lines mark the border between the CC and cerebral cortex (Ctx). (D', D'') The thickness of the CC and the density of GFAP⁺ and Olig2⁺ cells in the CC of treated control and mutant mice were quantified. NeuN staining in the treated control and mutant OB is shown (E) and quantified (E'). Bottom panels in (E) are the higher magnification view of the

boxed areas in the top panels. (F) Proposed model for the mechanism by which Nf1-regulated Erk signaling pathway regulates neuronal/glial fate specification of SVZ progenitors. SVZ progenitor cells most affected by *Nf1* inactivation are labeled as red (see main text). All the quantification data are presented as mean \pm SEM. Scale bars: 50 μ m. See also Figure S8.

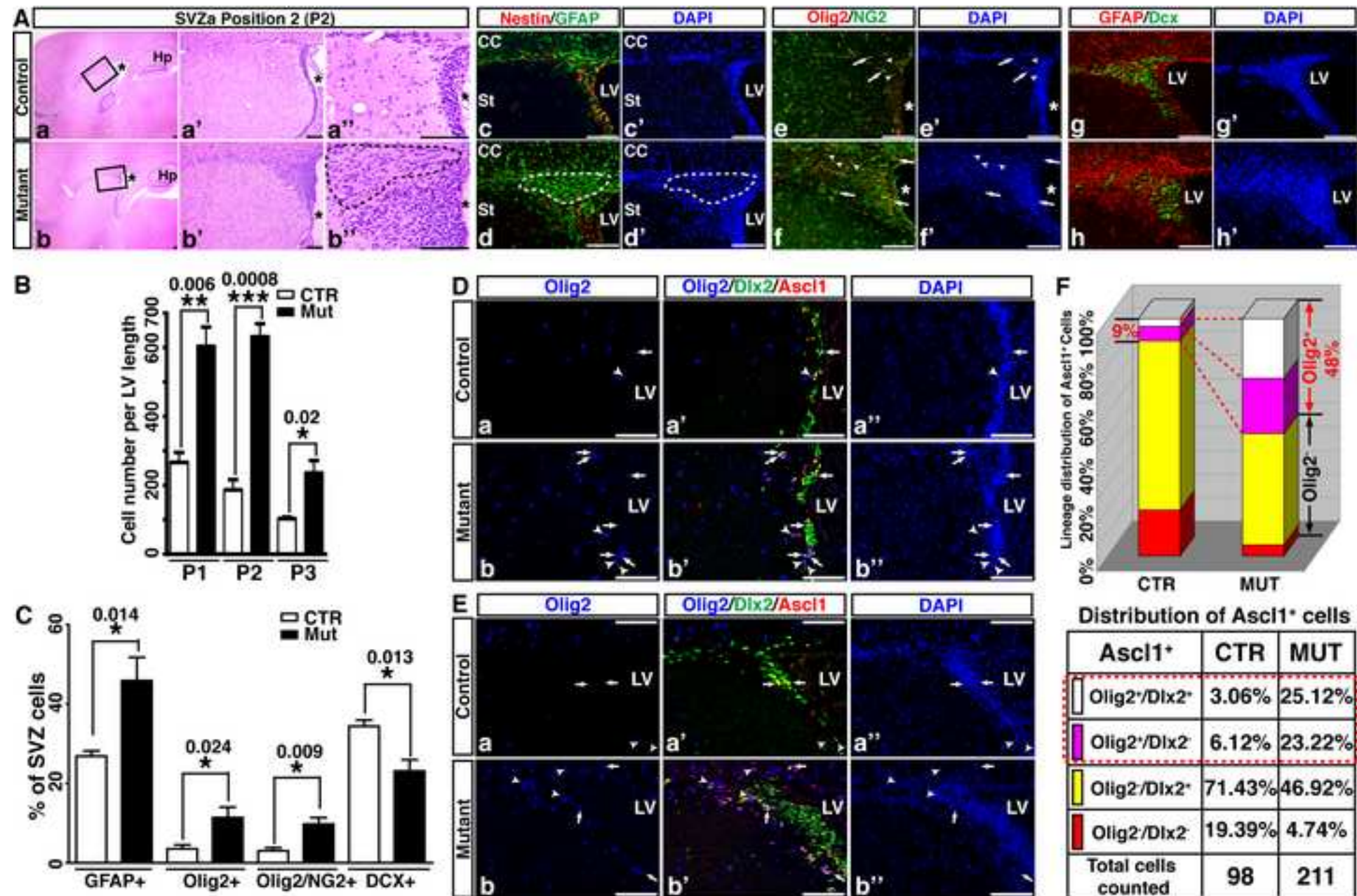
Figure

[Click here to download high resolution image](#)



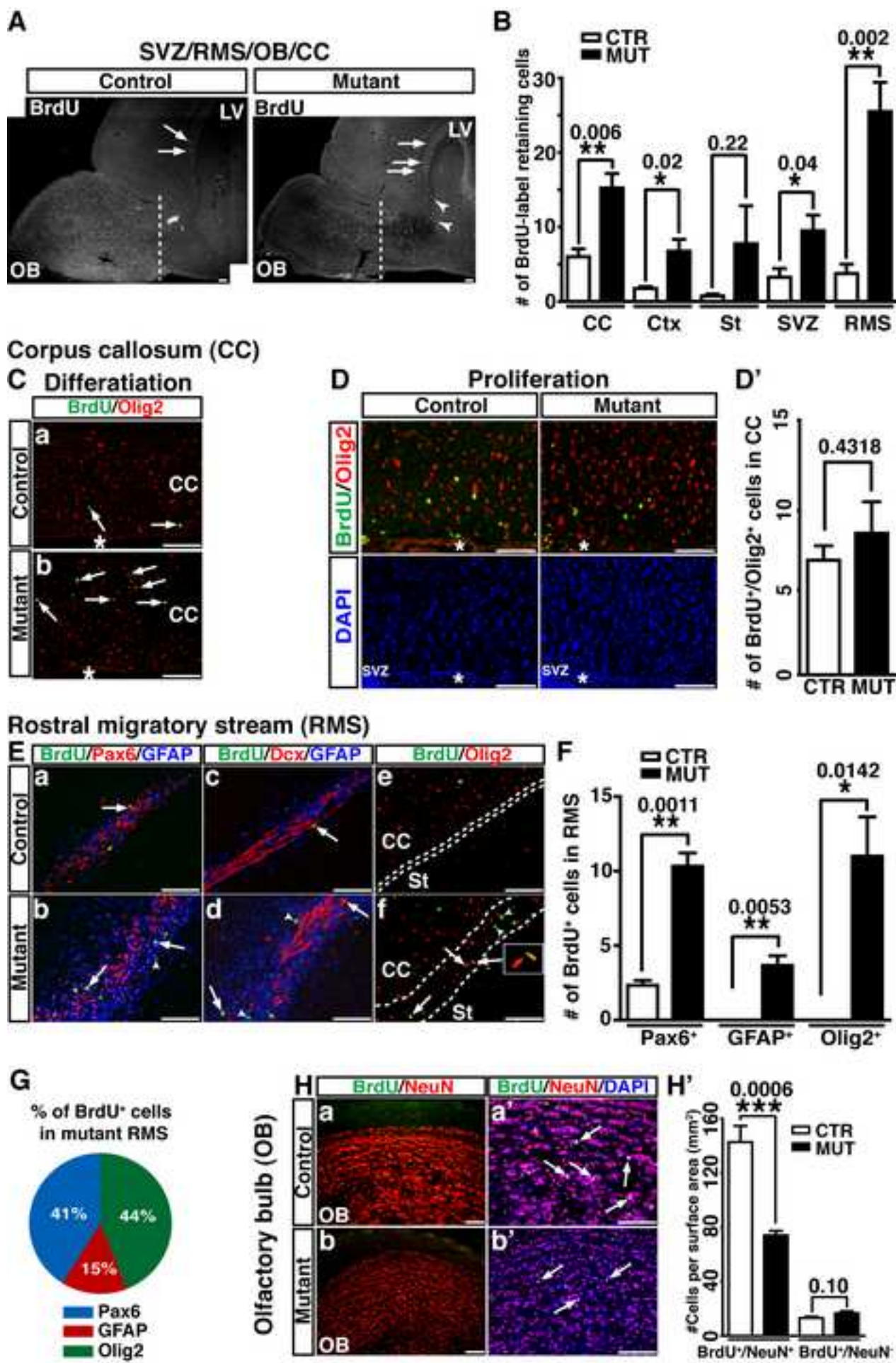
Figure

[Click here to download high resolution image](#)



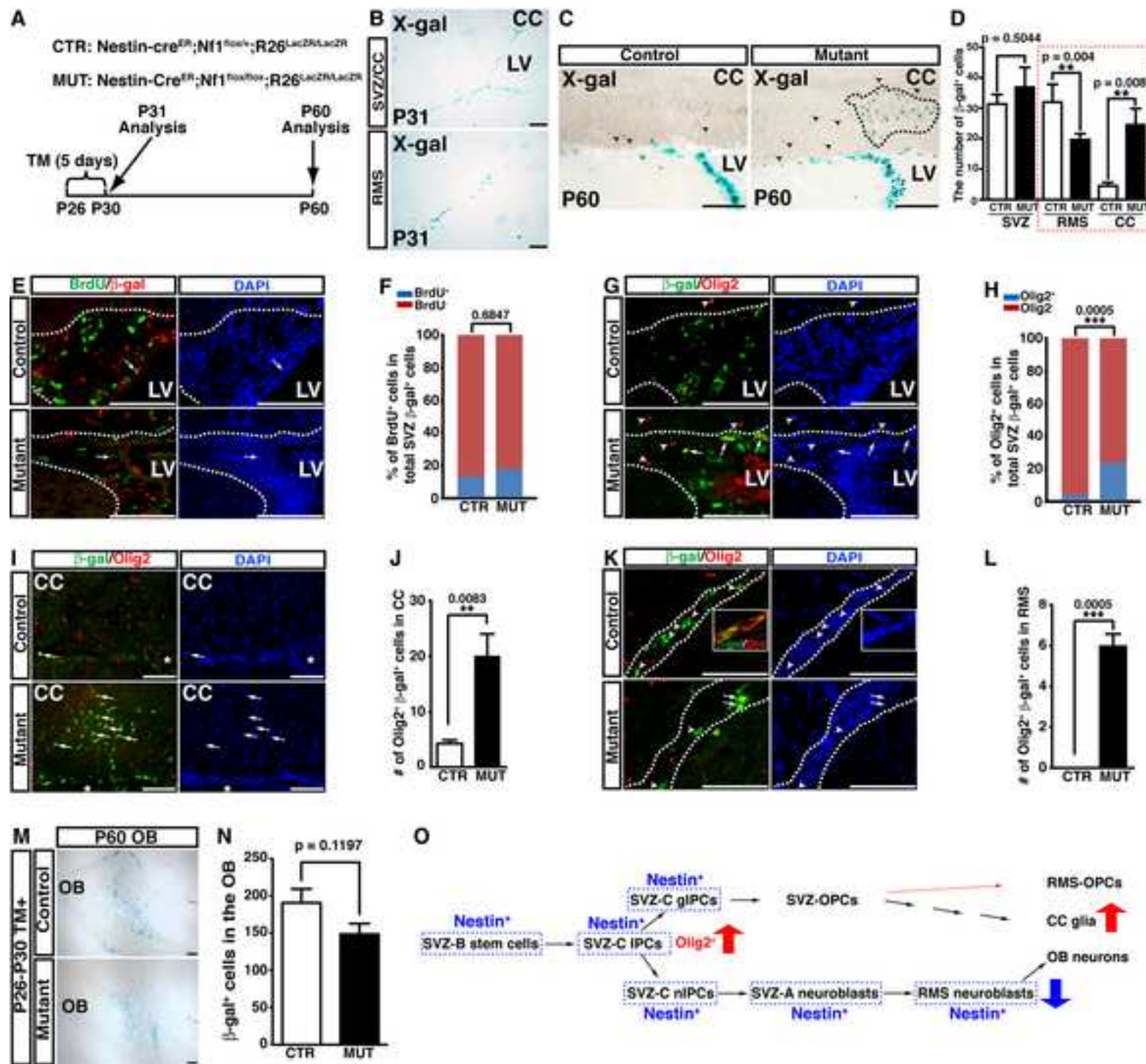
Figure

[Click here to download high resolution image](#)



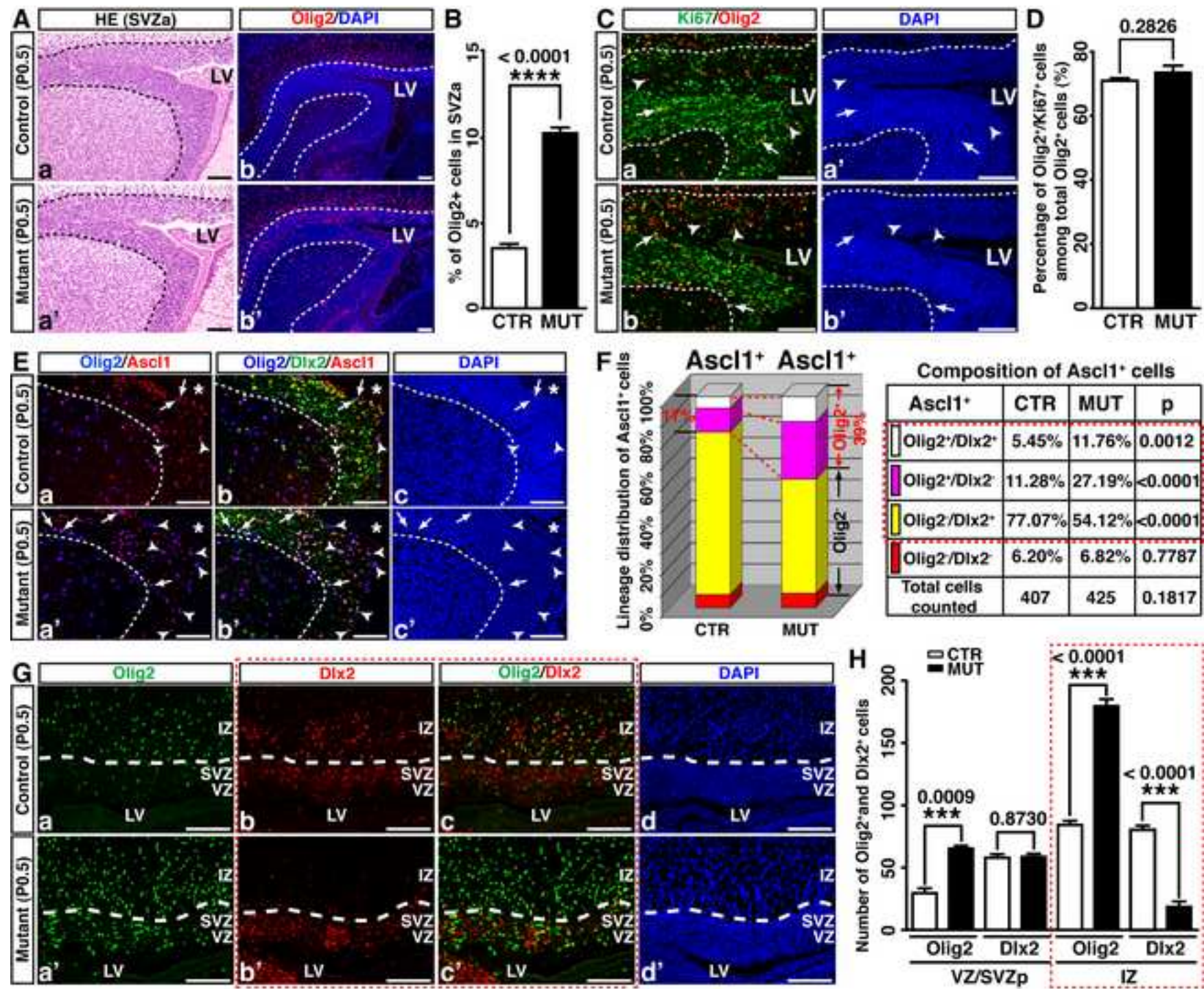
Figure

[Click here to download high resolution image](#)



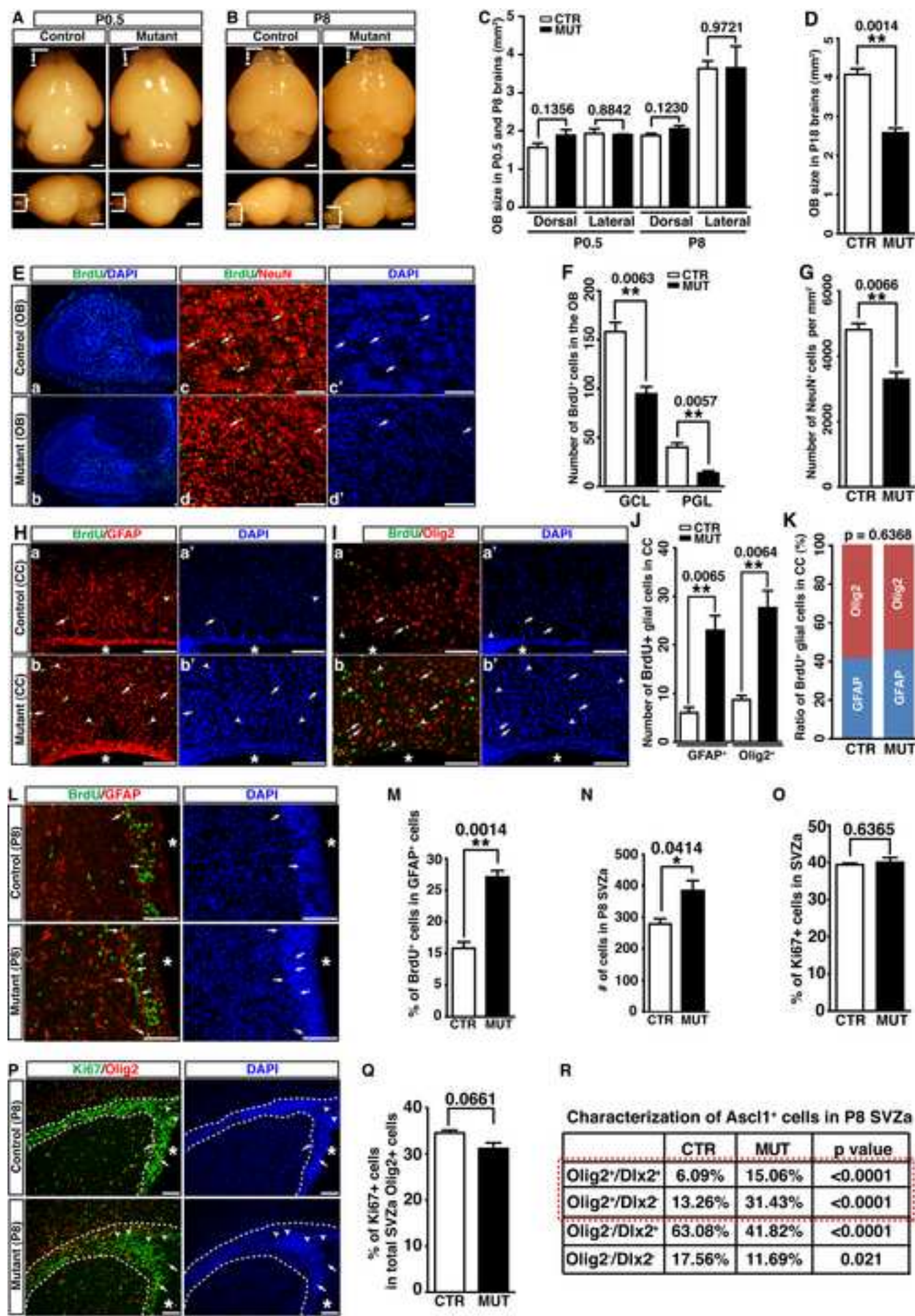
Figure

[Click here to download high resolution image](#)



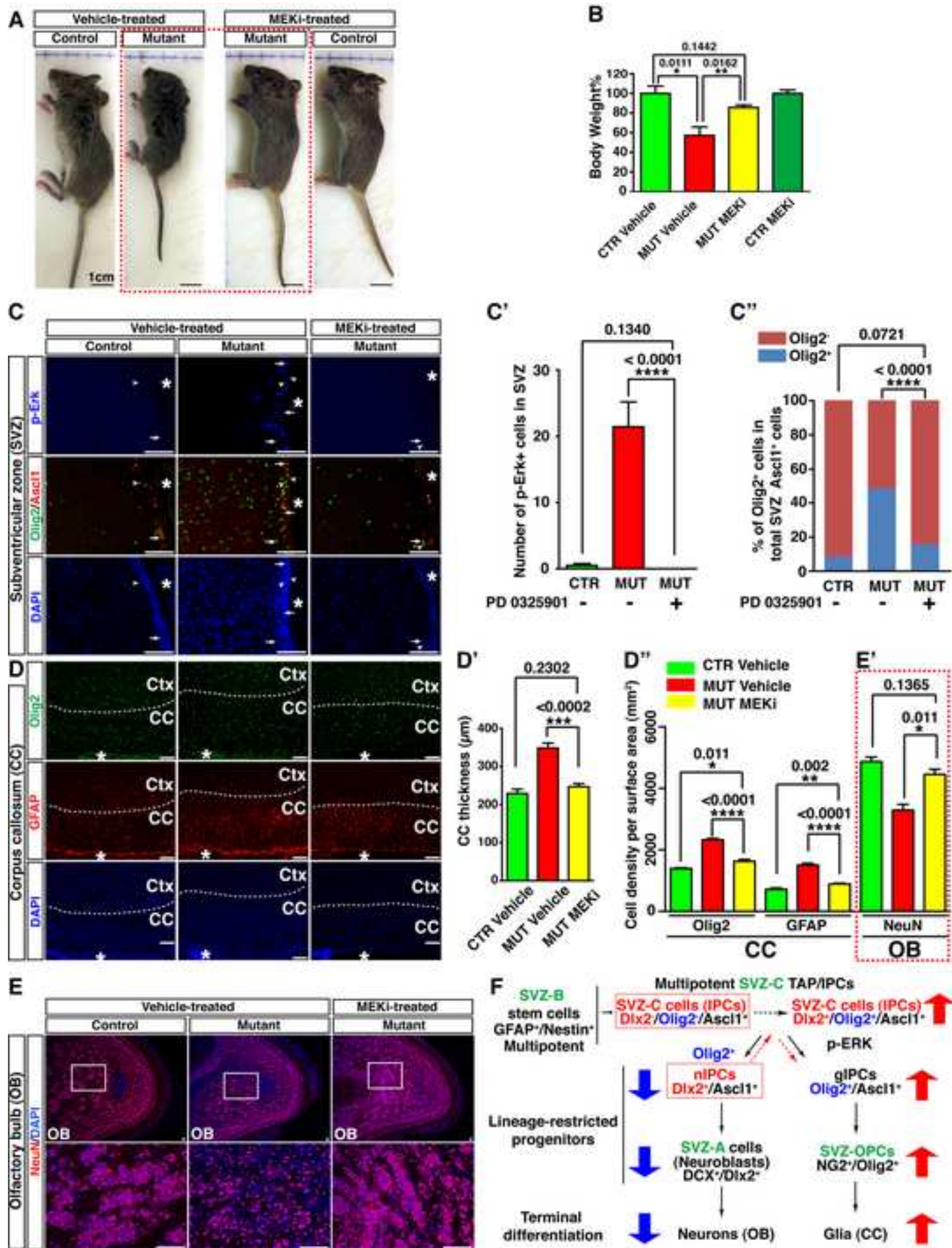
Figure

[Click here to download high resolution image](#)



Figure

[Click here to download high resolution image](#)



SUPPLEMENTAL INFORMATION INVENTORY

1. Supplemental figures

Figure S1. *Nf1*^{hGFAP}CKO brains exhibit enlarged corpus callosum with no alteration in the number of cortical neurons and axons. Related to Figure 1.

Figure S2. *Nf1*^{hGFAP}CKO brains exhibit enlarged SVZ. Related to Figure 2.

Figure S3. *Nf1* inactivation provides no significant growth advantage to different SVZ progenitor populations in adult brain. Related to Figure 2.

Figure S4. Characterization of adult RMS in control and *Nf1*^{hGFAP}CKO brains. Related to Figure 3.

Figure S5. Characterization of the Nestin-cre^{ER} inducible models in neonatal stages. Related to Figure 4.

Figure S6. Characterization of P0.5 SVZa and VZ/SVZ/IZ in control and *Nf1*^{hGFAP}CKO brains. Related to Figure 5.

Figure S7. Characterization of BrdU label retaining cells in control and *Nf1*^{hGFAP}CKO RMS at neonatal stages. Related to Figure 6.

Figure S8. Ectopic Olig2 expression is associated with Erk activation in *Nf1*-deficient Ascl1⁺ progenitors, and MEKi-treatment rescues the overall OB size defect in *Nf1*^{hGFAP}CKO mice. Related to Figure 7.

2. Supplemental figure legends

3. Supplemental text

4. Supplemental experimental procedures

5. Supplemental references.

SUPPLEMENTAL INFORMATION INVENTORY

1. Supplemental figures

Figure S1. *NfI*^{hGFAP}CKO brains exhibit enlarged corpus callosum with no alteration in the number of cortical neurons and axons. Related to Figure 1.

Figure S2. *NfI*^{hGFAP}CKO brains exhibit enlarged SVZ. Related to Figure 2.

Figure S3. *NfI* inactivation provides no significant growth advantage to different SVZ progenitor populations in adult brain. Related to Figure 2.

Figure S4. Characterization of adult RMS in control and *NfI*^{hGFAP}CKO brains. Related to Figure 3.

Figure S5. Characterization of the Nestin-cre^{ER} inducible models in neonatal stages. Related to Figure 4.

Figure S6. Characterization of P0.5 SVZa and VZ/SVZ/IZ in control and *NfI*^{hGFAP}CKO brains. Related to Figure 5.

Figure S7. Characterization of BrdU label retaining cells in control and *NfI*^{hGFAP}CKO RMS at neonatal stages. Related to Figure 6.

Figure S8. Ectopic Olig2 expression is associated with Erk activation in *NfI*-deficient Ascl1⁺ progenitors, and MEKi-treatment rescues the overall OB size defect in *NfI*^{hGFAP}CKO mice. Related to Figure 7.

2. Supplemental figure legends

3. Supplemental text

4. Supplemental experimental procedures

5. Supplemental references.

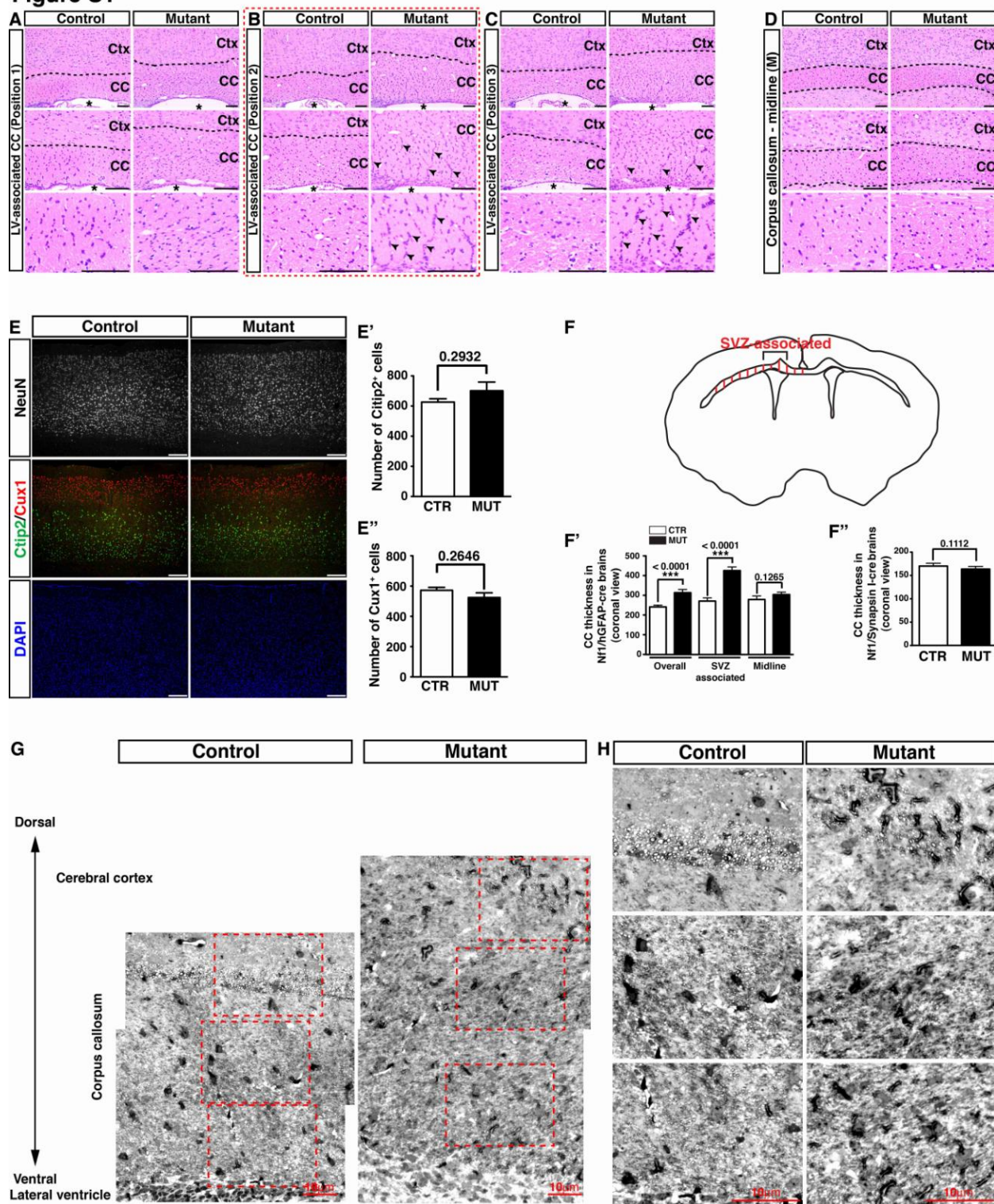
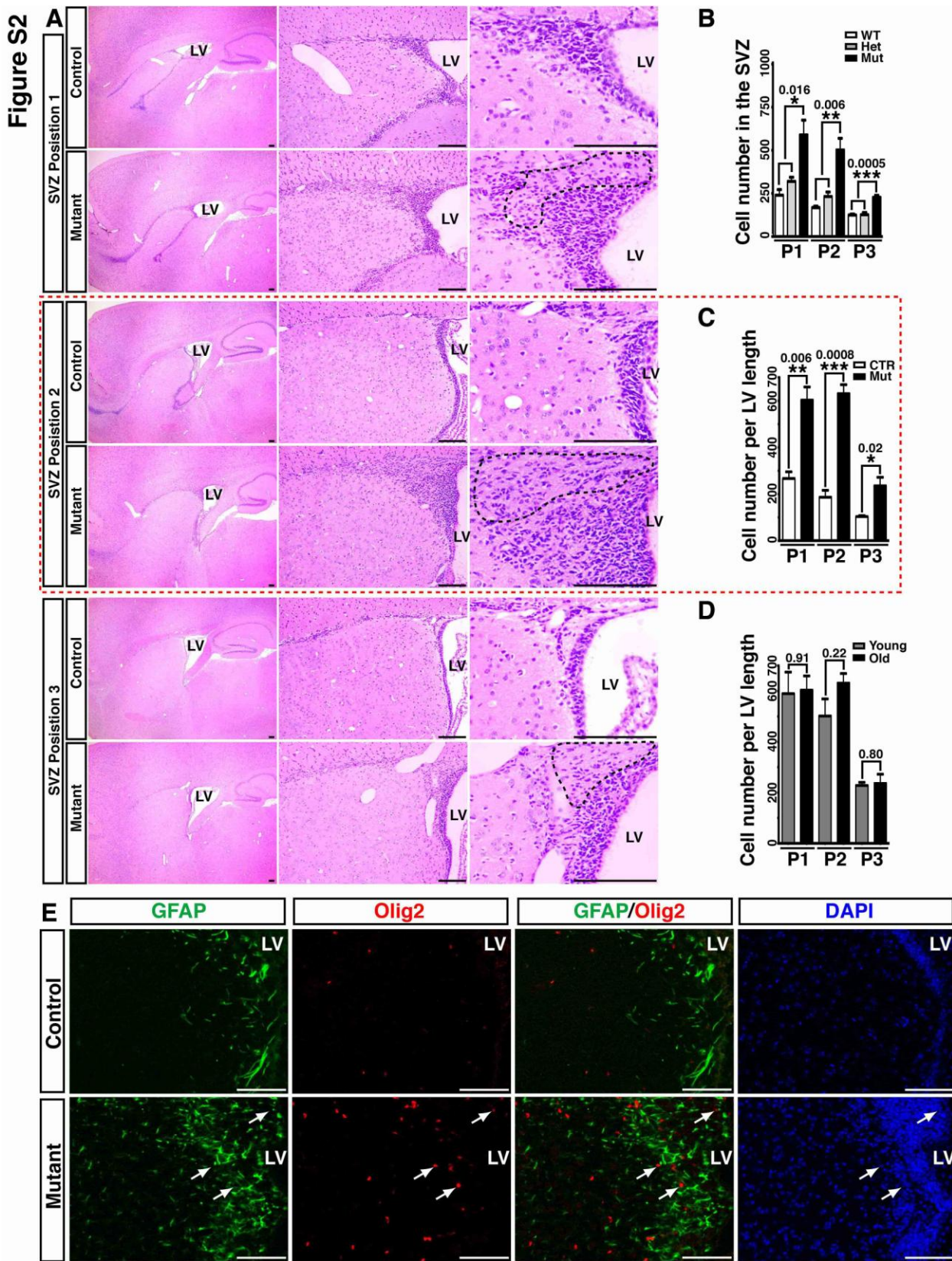
Figure S1

Figure S2

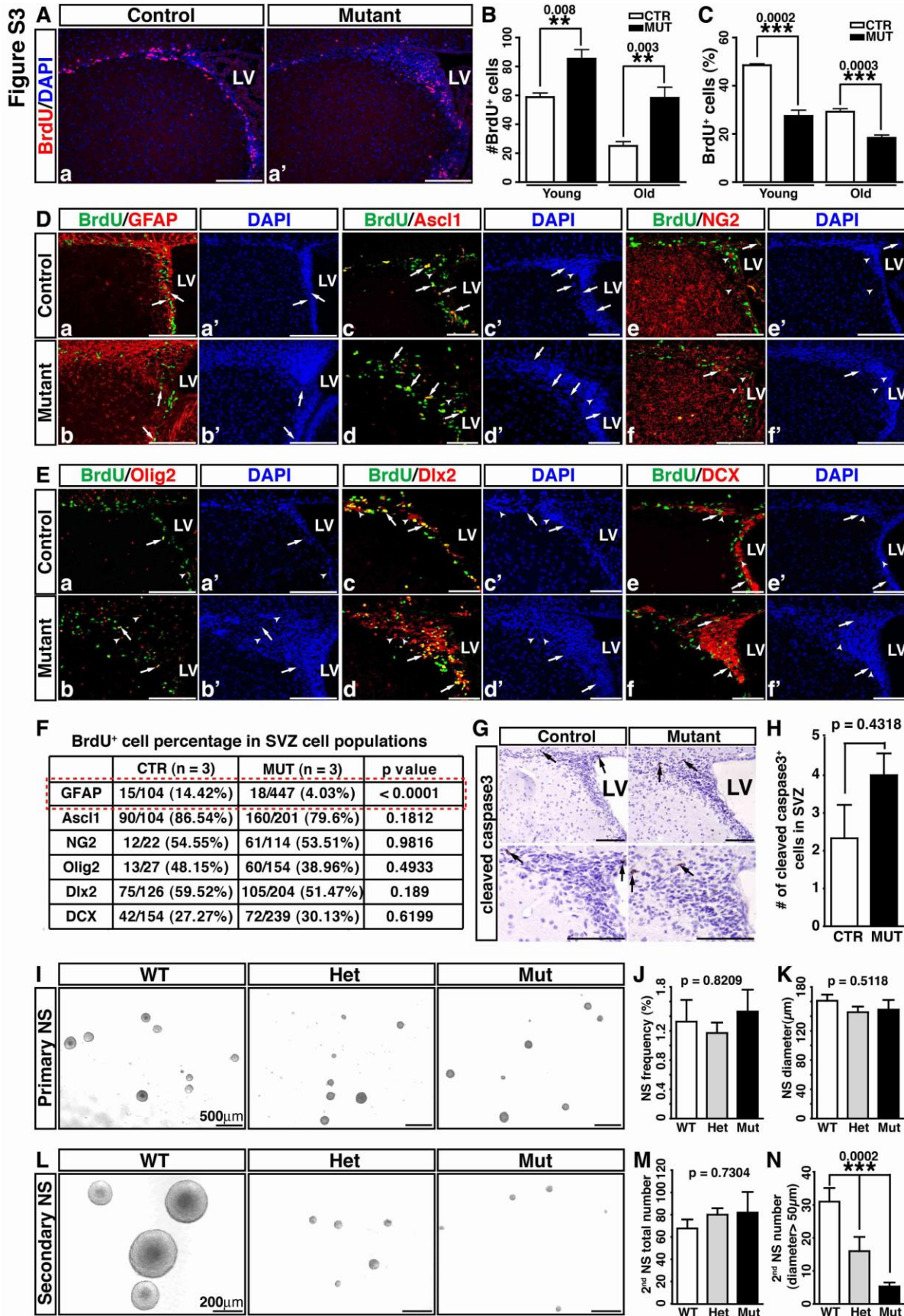


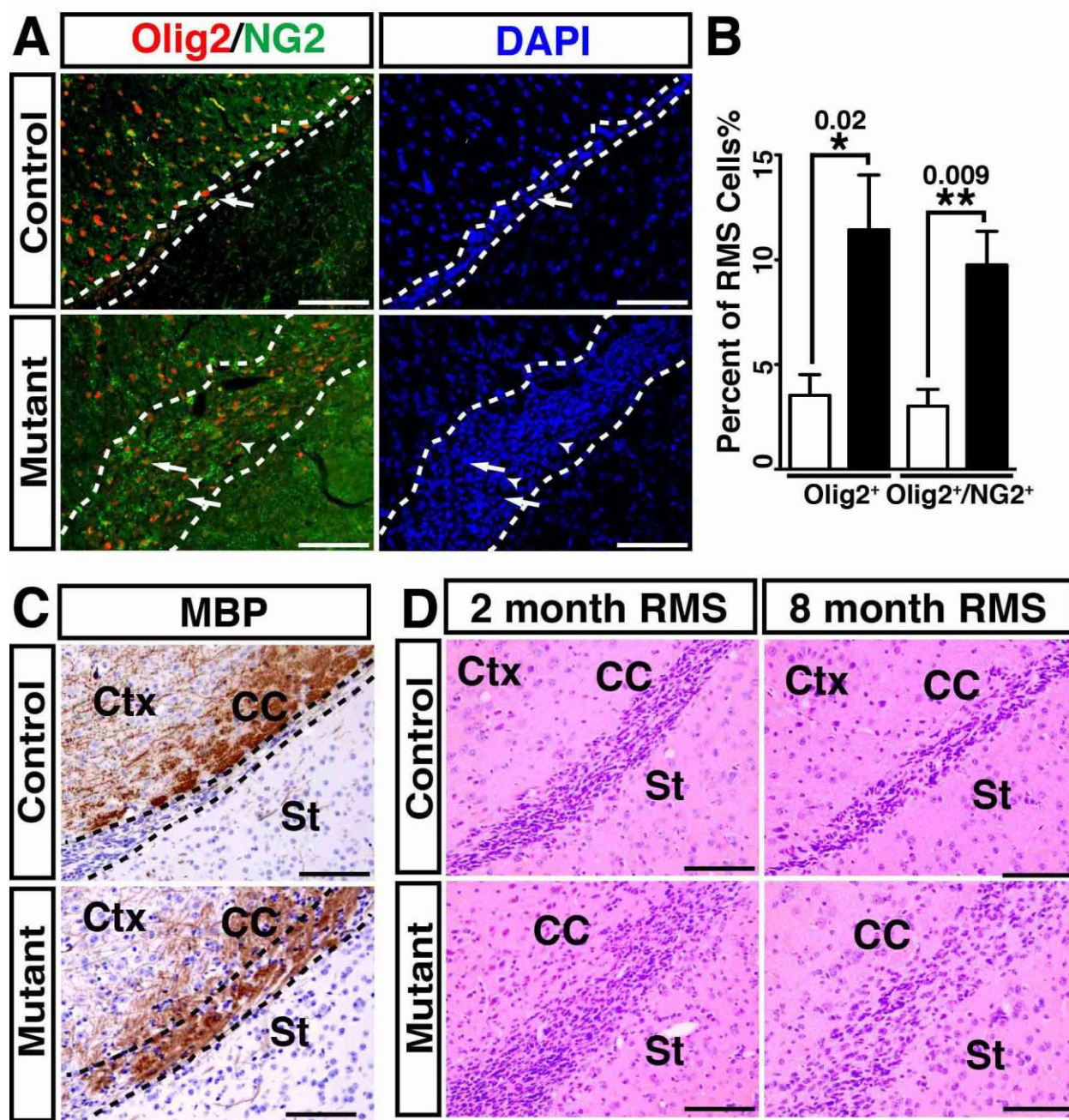
Figure S4

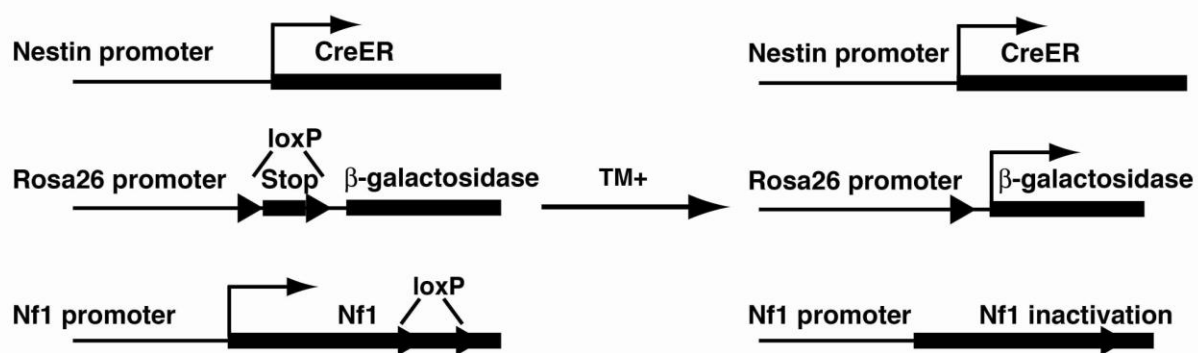
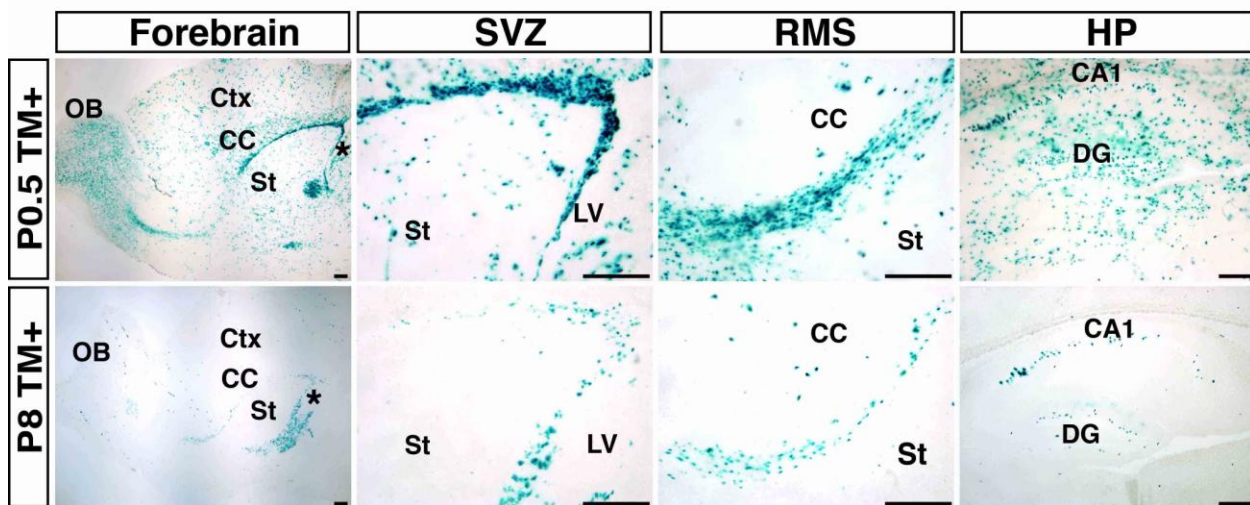
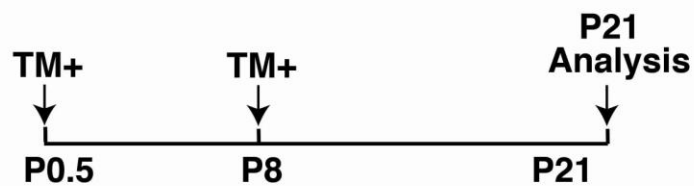
Figure S5**A****B**

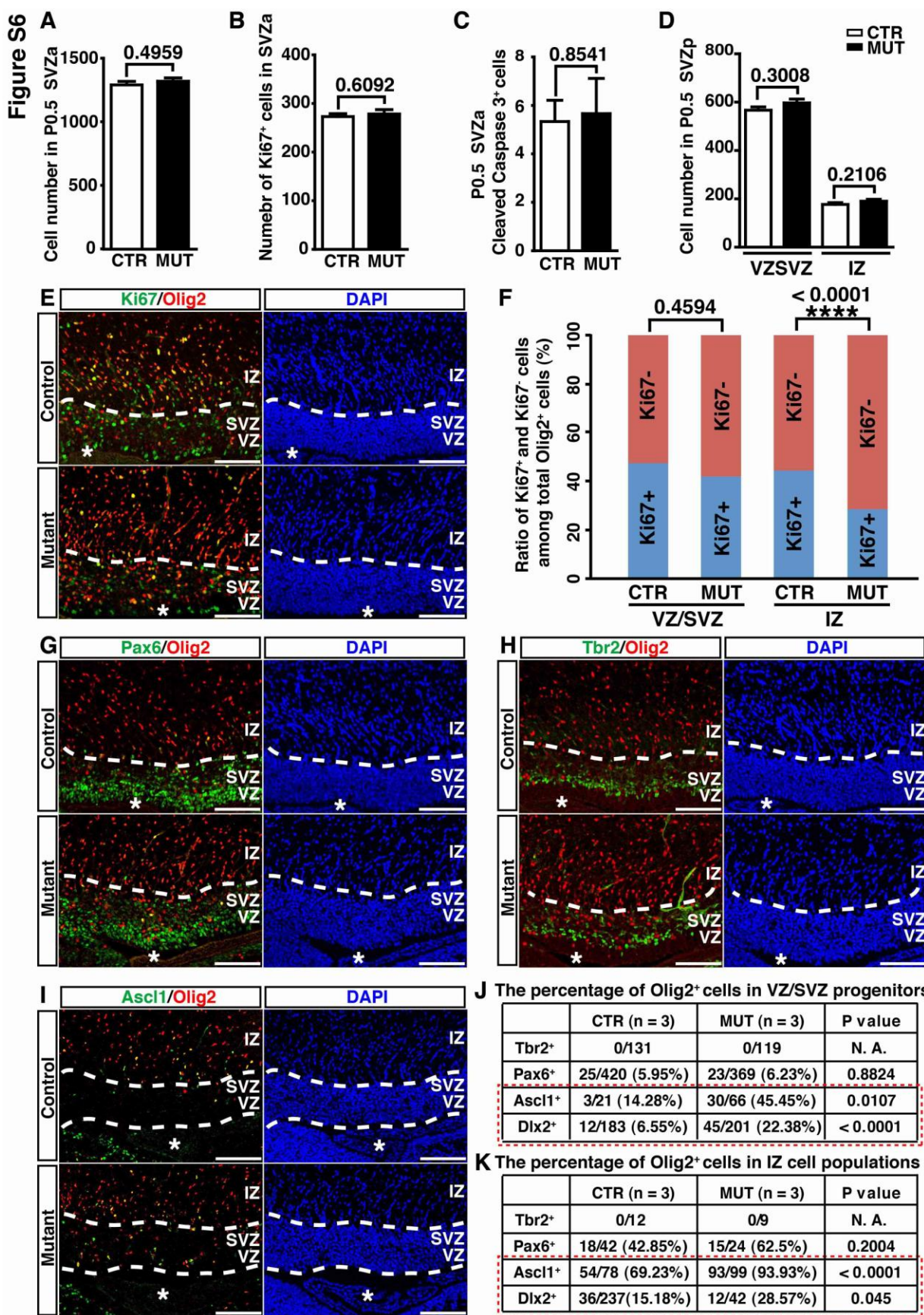
Figure S6

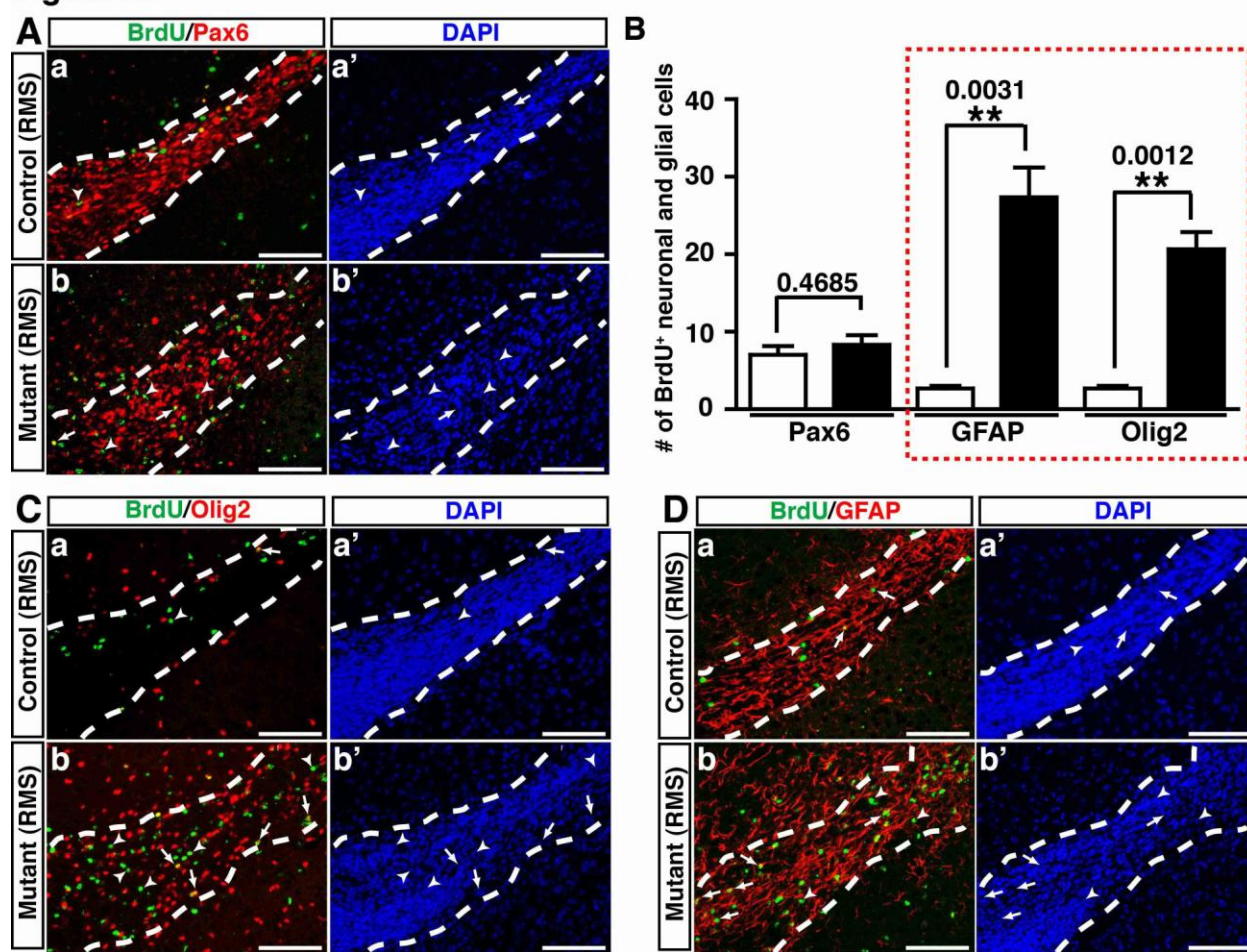
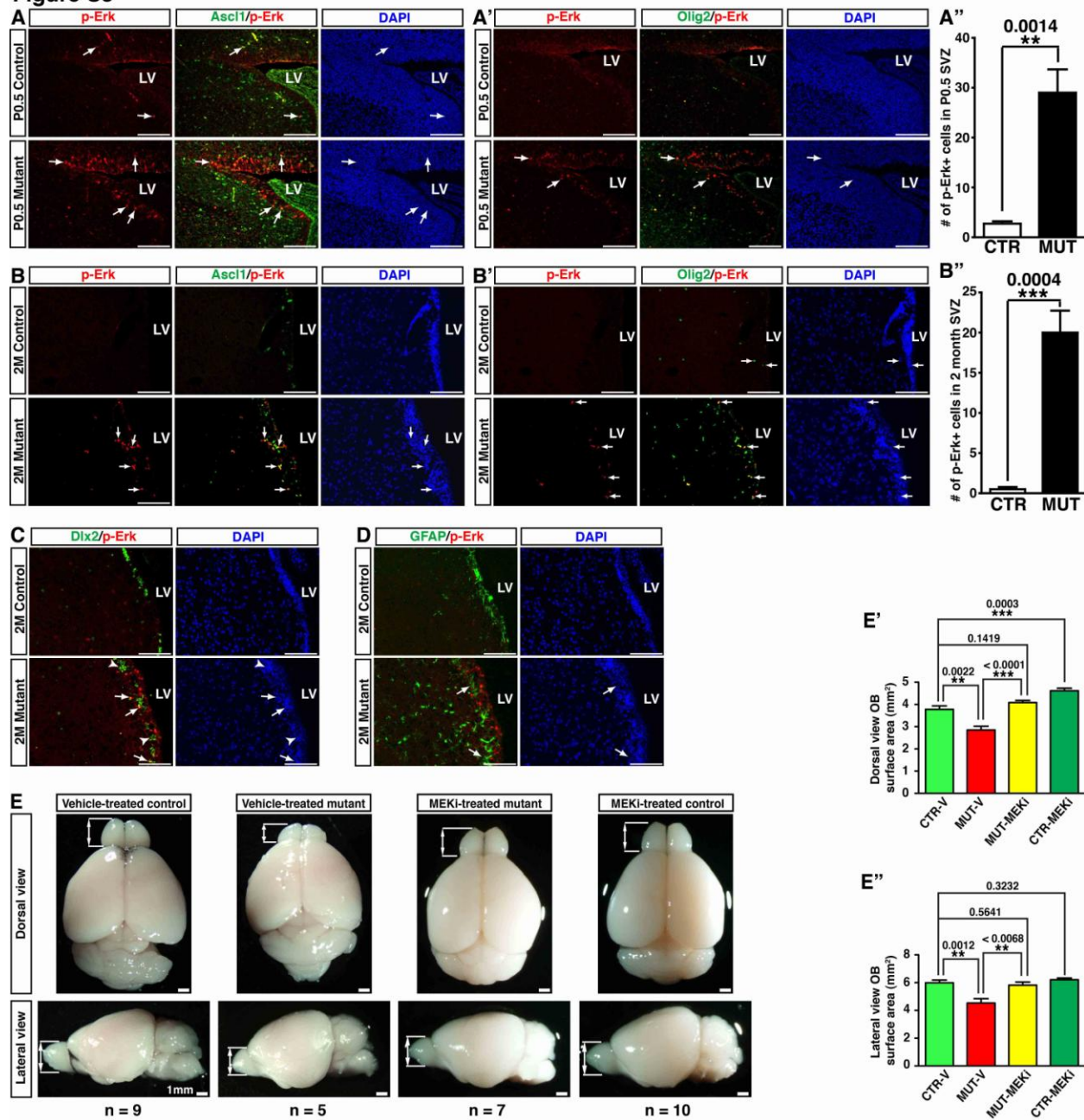
Figure S7

Figure S8

SUPPLEMENTARY INFORMATION**SUPPLEMENTAL FIGURE LEGENDS**

Figure S1. *Nf1*^{hGFAP}CKO brains exhibit an enlarged corpus callosum with no alteration in the number of cortical neurons and axons. Related to Figure 1.

(A-D) Representative H&E stained images of 2-month-old control and *Nf1*^{hGFAP}CKO CC are shown at positions 1-3 and midline position M. Dashed lines mark the border between the CC and cerebral cortex (Ctx). Panel B is also shown in Figure 1. (E-E'') NeuN, Ctip2 and Cux1 staining of the cerebral cortex in control and mutant brains. The number of Ctip2⁺ and Cux1⁺ cells were quantified in E' and E''. (F) A schematic representation of how the CC thickness was measured at 12 positions from the midline to lateral brain, as well as the definition of SVZ-associated CC in coronal sections. (F'-F'') Quantification of the CC thickness on coronal sections from control, *Nf1*^{hGFAP}CKO (F') and *Nf1*^{SynapsinI}CKO (F'') brains. (G) 0.5 μm semi-thin coronal sections from control and mutant brains were stained with toluidine blue. Representative high-magnification images were merged to cover the entire CC area between the lateral ventricle and cerebral cortex. (H) Higher magnification view of boxed regions in (G). DAPI labels nuclei. All the quantification data are presented as mean ± SEM. Scale bars: 10 μm for (G) and (H); 50 μm for all other panels.

Figure S2. *Nf1*^{hGFAP}CKO brains exhibit an enlarged SVZ. Related to Figure 2.

(A) Representative H&E stained images of 2-month-old control and *Nf1*^{hGFAP}CKO SVZ are shown at positions 1-3 (P₁₋₃). Dashed lines highlight the less cellular area exclusively identified in the *Nf1*^{hGFAP}CKO SVZ. Boxed panels are the enlarged version of Figure 2Aa-b'' and 2B. (B, C) Quantification of the absolute number of SVZ cells and the number of cells per unit length of LV at P_{1-P3} positions. (D) Comparison of SVZ cell number per LV length between 2-month-old (Young) and 8-month-old (Old) mutants. (E) Olig2/GFAP double-labeling experiments demonstrated that ectopic Olig2 expression (arrows) was not present in GFAP⁺ SVZ-B cells. DAPI labels nuclei. All the quantification data are presented as mean ± SEM. Scale bars: 50 μm.

Figure S3. *Nf1* inactivation provides no significant growth advantage to different SVZ progenitor populations in the adult brain. Related to Figure 2.

2-month-old mice were pulsed with BrdU 5 times a day and brains were collected, sectioned and stained for BrdU. (A) BrdU/DAPI labeling for the control and *Nf1*^{hGFAP}CKO SVZ. (B, C) Quantification for the absolute number (B) and percentage (C) of BrdU⁺ proliferating cells in the control and *Nf1*^{hGFAP}CKO SVZ at 2 months (Young) or 8 months (Old) of age. (D, E) BrdU⁺ cells were co-labeled with different lineage markers to determine the mitotic index in different SVZ progenitor populations. With the exceptions of GFAP⁺ cells (Da-b'), no significant difference in proliferation was found in Ascl1⁺ SVZ-C cells (Dc-d'), NG2⁺ SVZ-OPCs (De-f'), Olig2⁺ cells (Ea-b'), neurogenic Dlx2⁺ progenitors (Ec-d'), or Dcx⁺ SVZ-A neuroblasts (Ee-f'). Arrows and arrowheads identify the BrdU⁺ cells with or without coexpression of lineage markers, respectively. DAPI labels nuclei. (F) The ratio of BrdU⁺ proliferating cells in each of SVZ cell populations was quantified and summarized. (G, H) The number of cleaved caspase3-positive cells (arrows) in the control and *Nf1*^{hGFAP}CKO SVZ was analyzed and quantified. (I-K) In vitro neurosphere (NS) assays assess the frequency of neurosphere-forming activity, the size of primary neurospheres of *Nf1* wild-type, heterozygous and *Nf1*^{hGFAP}CKO neural stem and progenitor cells. (L) Primary neurospheres were further passaged to assess the secondary neurosphere-forming capacity between three *Nf1* genotypes. (M) The total number of multipotent secondary neurospheres generated from each primary neurosphere was quantified. (N) The quantification of the number of secondary neurospheres with diameters greater than 50 μm. All the quantification data are presented as mean ± SEM. Scale bars: 50 μm (A-G); 500 μm (I); 200 μm (L).

Figure S4. Characterization of the RMS in adult control and *Nf1*^{hGFAP}CKO brains. Related to Figure 3.

(A, B) On 2-month-old brain sections, Olig2/NG2 double-labeling analysis reveals the presence of a significantly greater number of Olig2⁺/NG2⁺ cells (arrows) and Olig2⁺/NG2⁻ (arrowheads) in the *Nf1*^{hGFAP}CKO RMS than controls. (C) Immunohistochemical staining demonstrates that the mutant, but not control RMS, exhibits a detectable level of myelin basic protein (MBP) expression. (D) Comparison between 2-month and 8-month-old control and mutant RMS by H&E staining shows progressively impaired cellular organization in the mutant RMS over time. Dashed lines mark the boundary of RMS and surrounding brain regions. DAPI labels nuclei. Scale bars: 50 μm.

Figure S5. Characterization of the Nestin-cre^{ER} inducible model during neonatal stages. Related to Figure 4.

(A) A summary of genetic configuration of the inducible mouse models and the scheme of tamoxifen (TM) induction experiments. (B) Control mice were induced with TM at P0.5 (upper panel) or P8 (lower panel) and analyzed at P21. X-gal staining was performed on brain sections to label recombined cells. Compared to TM induction at P0.5, the Nestin-cre^{ER}-targeted cell populations at P8 were mostly restricted to the SVZ/RMS/OB/CC system and hippocampal DG, validating the efficacy and specificity of the Nestin-cre^{ER} transgene in neural stem and progenitor cells. OB, olfactory bulb; CC, corpus callosum; CTX, cortex; ST, striatum; DG, dentate gyrus. LV and *, lateral ventricle. Scale bars: 50 μ m.

Figure S6. Characterization of P0.5 SVZa and VZ/SVZ/I_Z in control and *NfI*^{hGFAP}CKO brains. Related to Figure 5.

(A-D) The cell number (A), Ki67⁺ cell number (B), cleaved caspase3⁺ cell number (C) in the P0.5 SVZa and the cell number of P0.5 VZ/SVZ/I_Z (D) were quantified and are presented as mean \pm SEM. (E, F) The percentage of Ki67⁺ proliferating cells in Olig2⁺ cell populations in the VZ/SVZ and I_Z was analyzed and quantified. (G-K) The expression of Olig2⁺ in different cell populations was analyzed and summarized in (J, K). Dashed lines define the border of the VZ/SVZ and I_Z. DAPI labels nuclei. *, lateral ventricle. I_Z, intermediate zone. Scale bars: 50 μ m.

Figure S7. Characterization of BrdU-label retaining cells in the control and *NfI*^{hGFAP}CKO RMS during neonatal stages. Related to Figure 6.

Control and *NfI*^{hGFAP}CKO mice were pulsed with BrdU at P8 and analyzed at P18. (A, C, D) BrdU⁺ cells in the control and *NfI*^{hGFAP}CKO RMS were characterized by coexpression with lineage markers Pax6, Olig2 and GFAP. Arrows identify the colocalizing cells and arrowheads indicate the non-colocalizing cells. (B) The number of BrdU⁺ cells that coexpress these markers was quantified, presented as mean \pm SEM. DAPI labels nuclei. Scale bars: 50 μ m

Figure S8. Ectopic Olig2 expression is associated with Erk activation in *Nf1*-deficient Ascl1⁺ progenitors and MEKi-treatment rescues the overall OB size defect in *Nf1*^{hGFAP}CKO mice. Related to Figure 7.

(A, A') P0.5 control and mutant brain sections were stained for Ascl1/p-Erk (A) and Olig2/p-Erk (A'). Arrows identify double-labeling cells. (B, B') 2-month-old control and mutant brain sections were stained for Ascl1/p-Erk (B) and Olig2/p-Erk (B'). Arrows identify co-labeled cells. (A'', B'') The number of p-Erk⁺ cells in the P0.5 and 2 month-old SVZ was quantified. (C, D) Brain sections from 2-month-old control and mutant mice were stained for Dlx2/p-Erk and GFAP/p-Erk. Arrows and arrowheads label p-Erk⁺/Dlx2⁺ double-positive cells and p-Erk⁻/Dlx2⁺ cells, respectively (C). Arrows point to p-Erk⁺/GFAP⁻ cells (D). (E-E'') Control and *Nf1*^{hGFAP}CKO mice were treated with vehicle or MEKi from P0.5-P18 and P18 brains were collected for analysis. (E) Whole-mount brain images from vehicle and MEKi-treated control and *Nf1*^{hGFAP}CKO mice were compared. The size of the OB from treated control and mutant mice was measured from the dorsal view and the lateral view, and quantified in (E') and (E''), respectively. DAPI labels nuclei. All the quantification data are presented as mean ± SEM. Scale bars: (A-D), 50 μm; (E), 1mm.

SUPPLEMENTAL TEXT***Nf1* inactivation provides no significant growth advantage to adult SVZ cell populations (detailed text for Figure S3)**

Abnormally increased numbers of glial lineage cells observed in the *Nf1*^{hGFAP}CKO SVZ/CC system could result from an increase in proliferation or a reduction in apoptosis of SVZ stem and/or progenitor cells as expected from loss of *Nf1* tumor suppressor function. To investigate this possibility, we first determined the overall proliferation rate in the control and *Nf1*^{hGFAP}CKO SVZ using a bromodeoxyuridine (BrdU) assay. Although the absolute number of BrdU⁺ cells was increased in the enlarged *Nf1*^{hGFAP}CKO SVZ, the percentage of BrdU⁺ cells was significantly reduced compared to controls (Figure S3A-C). Importantly, the differences in the number and percentage of BrdU⁺ cells remained relatively stable between control and *Nf1*^{hGFAP}CKO SVZ as these mice aged from 2 to 8 months (Figure S3B, C). Together with the observation that these mice exhibited no evidence of tumor formation in the brain, these results indicate that *Nf1*-deficient SVZ cells are not hyperproliferative or tumorigenic, but rather maintain homeostasis during adulthood (Figure S2D). Second, we measured the percentage of BrdU⁺ cells in individual SVZ cell populations. No significant difference in proliferation was observed between the following control and *Nf1*^{hGFAP}CKO SVZ cell populations: Ascl1⁺ (also known as Mash1) SVZ-C TAP/IPC^s, Olig2⁺/NG2⁺ oligodendrocyte precursor cells (SVZ-OPCs), Dlx2⁺ neurogenic progenitors or Dcx⁺ SVZ-A neuroblasts (Figure S3D-F). Of note, due to the presence of a large number of differentiated astrocytes in the mutant SVZ, the percentage of BrdU⁺ cells in GFAP⁺ cell populations was significantly reduced (Figure S3Da-b', S3F). Third, using cleaved caspase3 immunohistochemical staining, we found no significant difference in apoptotic rate between control and *Nf1*^{hGFAP}CKO SVZ (Figure S3G, H). Finally, we performed in vitro neurosphere assays to compare growth properties of multipotent control and *Nf1*^{hGFAP}CKO SVZ stem and progenitor cells. No significant difference was found in the frequency of neurosphere-forming activity and the size of primary neurospheres derived from control and *Nf1*^{hGFAP}CKO SVZ (Figure S3I-K). Furthermore, we performed the self-renewal assay for SVZ stem and progenitor cells by measuring the ratio of the number of secondary neurospheres to primary neurospheres that exhibited multipotency. Although the number of multipotent secondary neurospheres generated by each primary neurosphere was comparable between control and *Nf1*^{hGFAP}CKO SVZ cells, the size of secondary neurospheres from *Nf1*^{hGFAP}CKO SVZ cells

was dramatically reduced compared with that of control cells (Figure S3L-N). These results indicate that *Nf1*-deficient SVZ stem and progenitor cells from adult brains retain the ability to undergo multilineage differentiation, but their growth properties were significantly impaired under in vitro culture conditions. Taken together, these results support the conclusion that alterations in proliferation or apoptosis in adult *Nf1*^{hGFAP}CKO SVZ are unlikely to contribute to increased glial lineage cells in the enlarged SVZ.

The characterization of the control and *Nf1*^{hGFAP}CKO neonatal SVZp (detailed text for Figure 5G, H and S6E-K)

Unlike the SVZa, neural stem/progenitor cells and more differentiated cells in the SVZp areas are spatially separated in the VZ/SVZp and overlying intermediate zone (IZ), respectively (Figure 5G). In the *Nf1*^{hGFAP}CKO VZ/SVZp, we observed a greater than 2-fold increase in the number of Olig2⁺ cells whereas the number of Dlx2⁺ cells was not significantly changed (Figure 5G, H). Similar to the SVZa, the increased Olig2 expression in the VZ/SVZp was also not caused by increased proliferation (Figure S6E, F), but instead was caused by ectopic Olig2 expression in Ascl1⁺ and Dlx2⁺ progenitors (Figure S6F, I, J). Of note, Olig2 expression was not expanded in Pax6⁺ VZ and Tbr2⁺ SVZ progenitor cells (Figure S6G, H). In the IZ, the expression of Olig2 and Dlx2 is almost mutually exclusive, suggesting that once cells become more differentiated, they selectively express only one of these two transcription factors. Strikingly, *Nf1*^{hGFAP}CKO IZ cells exhibited a substantial loss of Dlx2 expression with a concomitant increase of Olig2-expressing cells (Figure 5G, H). This observation suggests that ectopic Olig2 expression suppresses Dlx2 expression as these cells become more differentiated and migrate to the IZ, leading to overproduction of Olig2⁺ lineage cells at the expense of the Dlx2⁺ lineages.

The characterization of the control and *Nf1*^{hGFAP}CKO P8 SVZa (detailed text for Figure 6L-R)

It is worth noting that the size and cell number of *Nf1*^{hGFAP}CKO SVZ was already significantly enlarged at P8, and this was accompanied by an increase in proliferation of GFAP⁺ stem cells (Figure 6L-N). Since *Nf1* inactivation confers no growth advantage to adult SVZ cells, this observation suggests that Nf1 is only transiently required for regulating SVZ stem cell proliferation in the early postnatal brain. However, the overall proliferation rate in *Nf1*^{hGFAP}CKO

SVZ was not significantly altered, which was at least partially attributed to a slightly reduced proliferation of Olig2⁺ cells (Figure 6O-Q) (Lee da et al., 2010). Most of the differentiated Olig2⁺ cells, which were negative for Ki67 expression, accumulated in the anterior-dorsal parts of the SVZ (arrows, Figure 6P), an area where an excessive number of differentiated astrocytes were observed in the adult *Nf1*^{hGFAP}CKO SVZ (Figure 2A). Taken together, these results demonstrate that ectopic expression of Olig2 in Ascl1⁺ progenitors caused by *Nf1* inactivation manifests during neonatal stages (Figure 6R), leading to increased gliogenesis in the CC at the expense of neurogenesis in the OB. Consequently, Nf1-related structural brain defects including enlarged CC and reduced OB are both established during early postnatal stages.

Ectopic Olig2 expression in TAP/IPCs is associated with Erk pathway activation (detailed text for Figure S8A-C)

We investigated the molecular mechanism underlying ectopic Olig2 expression in SVZ progenitors caused by *Nf1* inactivation. Since Nf1 functions as a negative regulator of Ras-mediated signaling pathways, we analyzed three major downstream effectors of Ras signaling pathways: Erk/MAPK, phosphatidylinositol 3-kinase (PI3K)/Akt and mammalian target of rapamycin complex 1 (mTORC1). Specifically, we used phospho-specific antibodies of Erk (p-Erk), Akt (p-Akt) and S6 (p-S6) kinases to evaluate the activation status of these pathways in control and *Nf1*^{hGFAP}CKO brains. We found no evidence that the alteration of PI3K/Akt or mTORC1 signaling pathways contributes to ectopic Olig2 expression in *Nf1*-deficient TAP/IPCs (data not shown). We therefore focused on the Erk signaling pathway. In paraffin-embedded brain sections, robust p-Erk staining was only identified in a small number of SVZ cells in control neonatal brains and was reduced to a minimal level in the control adult SVZ (Figure S8A-F), which is correlated with the diminished gliogenic output in the adult SVZ. In contrast, p-Erk⁺ cells were readily detected and greatly increased in both neonatal and adult SVZ of *Nf1*^{hGFAP}CKO brains (Figure S8A-B'). Importantly, consistent with the finding that *Nf1* inactivation causes ectopic Olig2 expression specifically in Ascl1⁺ TAP/IPCs, p-Erk expression was restricted to Ascl1⁺ and Olig2⁺ cells in the SVZ of both neonatal and adult *Nf1*^{hGFAP}CKO brains (Figure S8A-D). Specifically, over 80% and 90% of p-Erk⁺ cells in the adult *Nf1*^{hGFAP}CKO SVZ expressed Ascl1 and Olig2, respectively. These observations suggest that a large proportion of *Nf1*-deficient p-Erk⁺ cells expressed both Ascl1 and Olig2. Consistently, only

a subset of neurogenic $Dlx2^+$ cells, but never $GFAP^+$ stem cells, expressed a detectable level of p-Erk in the Nfl^{hGFAP} CKO SVZ (Figure S8C, D). Together, these results are most consistent with the model wherein Nfl -mediated negative regulation of Erk signaling suppresses Olig2 expression and consequently, glial fates in neurogenic $Ascl1^+$ TAP/PCPs.

EXPERIMENTAL PROCEDURES (Detailed methods)

Tissue preparation

For histological analysis, we utilized both paraffin and frozen sections. Control and mutant littermates at various time points were perfused with 4% paraformaldehyde (PFA). Brains were divided into two hemispheres along the midline and each hemisphere was processed for either paraffin-embedded or frozen sections. For paraffin sections, brains were dissected and post-fixed in 4% PFA overnight at 4 °C. For frozen sections, brains were dissected, post-fixed in PFA for 2 hours at 4 °C, and transferred to 30% sucrose overnight at 4 °C. Brains were then embedded in O.C.T. compound (Tissue-Tek) and frozen on dry ice.

Histological analysis

Serial sections were sagittally prepared at 5 µm for paraffin sections. Slides from histologically comparable positions were stained by H&E. For adult brains in particular, at least three independent positions (position 1-3, Figure S1) that contain the SVZ/RMS were selected for quantification. Each position is approximately 100 µm apart at sagittal planes along the midline to lateral direction and was determined by histological criteria (P1: oval lateral ventricle with intact RMS; P2: triangular lateral ventricle with intact RMS; P3: triangular lateral ventricle with non-intact RMS). Midline position (M) was also analyzed for corpus callosum comparisons.

Immunohistochemistry and immunofluorescence

Immunohistochemistry was performed on paraffin sections. The visualization of primary antibodies was performed with the avidin-biotin horseradish peroxidase system (Vectastain ABC kit, Vector). The dilutions of primary antibodies used on paraffin sections in this study were: MBP (1:500, rat, Chemicon) and cleaved caspase3 (1:500, rabbit, Cell signaling). Immunofluorescence was performed on both paraffin and frozen sections. Visualization of primary antibodies was performed by using Cy2 (or Alexa 488), Cy3 (or Alexa 555) and Cy5 (Alexa 647)-conjugated secondary antibodies (1:200, Cy2/Cy3/Cy5, Jackson Immunoresearch; 1:400, Alexa 488/555/647, Invitrogen). The dilutions of primary antibodies used in this study were as follows: NF200 (1:500, rabbit, Sigma), Cux1 (1: 100, rabbit, Sigma), Ctip2 (1:500, rat, Abcam), Nestin (1:100, mouse, Chemicon), GFAP (1:2000, mouse, BD Pharmingen), GFAP (1:2000, mouse, DAKO), Ascl1 (Mash1, 1:200, mouse, BD Pharmingen), Dlx2 (1:2000, guinea

pig, K. Yoshikawa), Dcx (1:2000, rabbit, Abcam), Dcx (1:2000, guinea pig, Chemicon), Pax6 (1:500, rabbit, Covance), PSA-NCAM (1:1000, mouse, Chemicon), NeuN (1:400, mouse, Chemicon), Olig2 (1:2000, rabbit, Millipore), Olig2 (1:10000, guinea pig, B. Novitch), NG2 (1:200, mouse, Millipore), BrdU (1:1000, rat, Abcam), Ki-67 (1:500, mouse, BD Pharmingen), β -gal (1:1000, rabbit, 5 prime-3 prime), β -gal (1:1000, goat, AbD Serotec), p-ERK (1:100, rabbit, Cell Signaling), p-S6 (1:1000, rabbit, Cell Signaling), Tbr2 (1:1000, rabbit, Abcam). Sections were examined under a fluorescence microscope (Olympus).

Electron microscopy analysis

Mice were perfused and dissected. Brains were fixed in 4% PFA and 2.5% gluteraldehyde for 1 h and coronally sectioned at 100- μ m thickness with a vibratome. From each mouse, one brain slice at comparable positions with structures including lateral ventricle and corpus callosum was post-fixed in 4% PFA and 2.5% gluteraldehyde overnight at 4°C. Tissues were then fixed in OsO4 for 1 hour and embedded in epoxy resin. Semithin sections were cut with a glass knife at 0.5 μ m and stained with toluidine blue for visualization. Ultrathin sections were cut with a diamond knife at 75 nm and visualized using transmission electron microscope (TEM). Multiple images that cover the entire corpus callosum area between the lateral ventricle and cerebral cortex at 2 parallel positions (column 1 and column 2) were taken for histological evaluation and quantification.

β -gal staining

The R26^{LacZR} allele was introduced to the control and *Nfl*^{NcreER}CKO mice as a reporter to monitor Cre-mediated recombination. Dissected brains were prepared for frozen sections as mentioned in Tissue Preparation. Frozen sections were cut at 10-14 μ m and subjected to X-gal staining for 1 hour to overnight depending on the signal intensity. X-gal staining was performed as described previously (Zhu et al., 1998; Zhu et al., 2001). Co-localization of β -gal expressing cells with BrdU and other lineage markers was obtained by double immunofluorescence labeling.

Tamoxifen administration in Nestin-cre^{ER} inducible system

Tamoxifen was dissolved in corn oil (Sigma) at a concentration of 20mg/ml and stored at -20°C. Mice carrying the Nestin-cre^{ER} transgene were administered with tamoxifen through intraperitoneal (IP) injection at a dosage of 5mg per 40g body weight. Induction at P0.5 or P8

only required a single tamoxifen injection, while induction in young adult required daily tamoxifen injections for 5 constitutive days from P26-P30.

BrdU assay

Adult mice were pulsed with 50 μ g/g (gram, body weight) of BrdU five times daily at 2-hour intervals. Neonatal mice only received a single injection of BrdU with same dosage. For proliferation assay, mice were perfused with 4% PFA 2 hours after the last pulse. For BrdU differentiation assay, mice were sacrificed 30 days (adult) or 10 days (neonatal) after the initial pulse. In both assays, brains were dissected and processed for either paraffin-embedded or cryostat sections. BrdU immunofluorescence was performed as described previously (Wang et al., 2009).

Neurosphere cell culture

SVZ cells were dissected and dissociated from adult brains and were cultured in self-renewal medium based on previously published protocol (Molofsky et al., 2003). Cell density was quantified on a cell-counter plate and 2000 cells/well were plated to 6-well ultra-low binding plates for primary neurosphere culture. Cultured neurospheres were grown for 10 days before analysis. The number and size of neurospheres were compared and quantified. To determine the percentage of multipotent neurospheres, 8 neurospheres from each 10-day-old colony were replated and cultured adherently in differentiation medium for 12 days. The differentiated progeny were triple-labeled by O4 (1:500, mouse IgG1, Millipore), Tuj1 (1:500, mouse IgG2a, Covance) and GFAP (1:2000, rabbit, Dako) through immunocytochemical staining to determine the number of oligodendrocytes, neurons and astrocytes, respectively. Neurosphere colonies that contain all three primary brain cell types were considered multipotent. The percentage of multipotent neurospheres of total neurospheres analyzed was not significantly different from the control and *NfI*^{hGFAP}CKO SVZ of adult brains (>90%). To self-renew neurospheres, individual 10-day-old neurospheres were picked by pipette, centrifuged, and then mechanically dissociated and replated. 10 days into the secondary culture, we quantified the self-renewal capacity as the number of multipotent secondary neurospheres generated per primary neurosphere (2°NS/1°NS). All the data presented in this study were based on multipotent primary and secondary neurospheres.

Western blot analysis

Snap-frozen tissues were homogenized in 1X SDS loading buffer [50 mM Tris-HCL (pH 6.8), 2% SDS, 0.05% bromophenol blue, 10% glycerol, 100mM β -mercaptoethanol]. Samples were analyzed by SDS-PAGE and transferred onto PVDF membranes (Millipore). The blots were then blocked in 5% non-fat milk in TBST, followed by incubation of primary antibodies at 4°C overnight. After washing, the blots were incubated in horseradish peroxidase (HRP)-conjugated secondary antibodies at room temperature for 1 hour. Signals were detected using ECL or ECL plus (GE healthcare) followed by film development. The primary antibodies used were as follows: p-Erk (1:1000, Cell Signaling), Erk (1:1000, Cell Signaling).

Quantification and statistical analysis

Anatomically comparable sections from control and mutant brains were visualized under 40X magnification using an Olympus BX51 microscope. Images were captured and subjected to double-blinded analysis. Lengths, areas and the number of cells were quantified using the ImageJ software package. Statistical analysis was carried out using two-tailed Student's t-test. $p < 0.05$ was considered to be statistically significant. Comparisons between more than two groups (i.e. wild-type, heterozygous and homozygous) were based on Anova test. To compare the proportions of certain types of cells from two independent cell populations (i.e. percentage of Olig2 $^{+}$ cells in Ascl1 $^{+}$ cells in control and mutant SVZ) and to determine if they are statistically different from one another, the number of specific cell types was quantified and subjected to Chi-Square and/or Fisher's exact test. At least three animals from each group were used for quantification. Data were presented as mean \pm Standard Error Mean (SEM). $p < 0.05$ was considered to be statistically significant.

REFERENCES

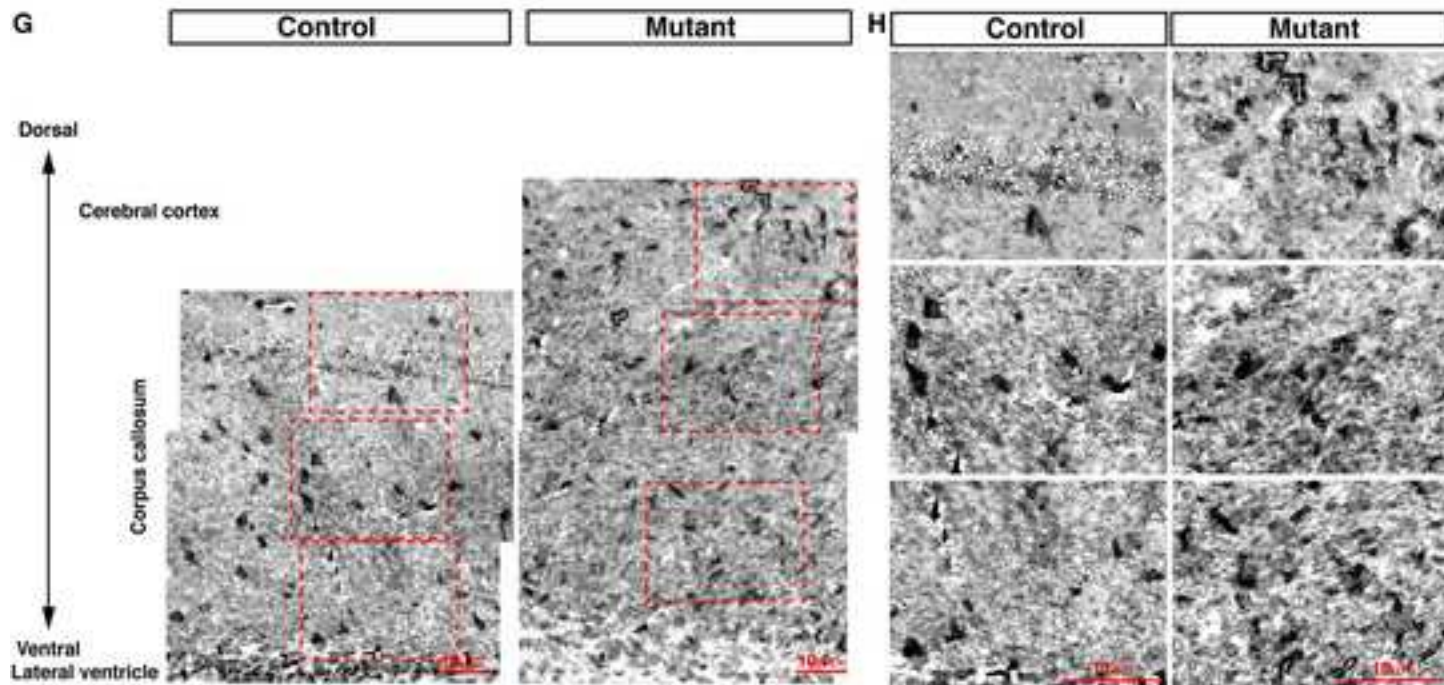
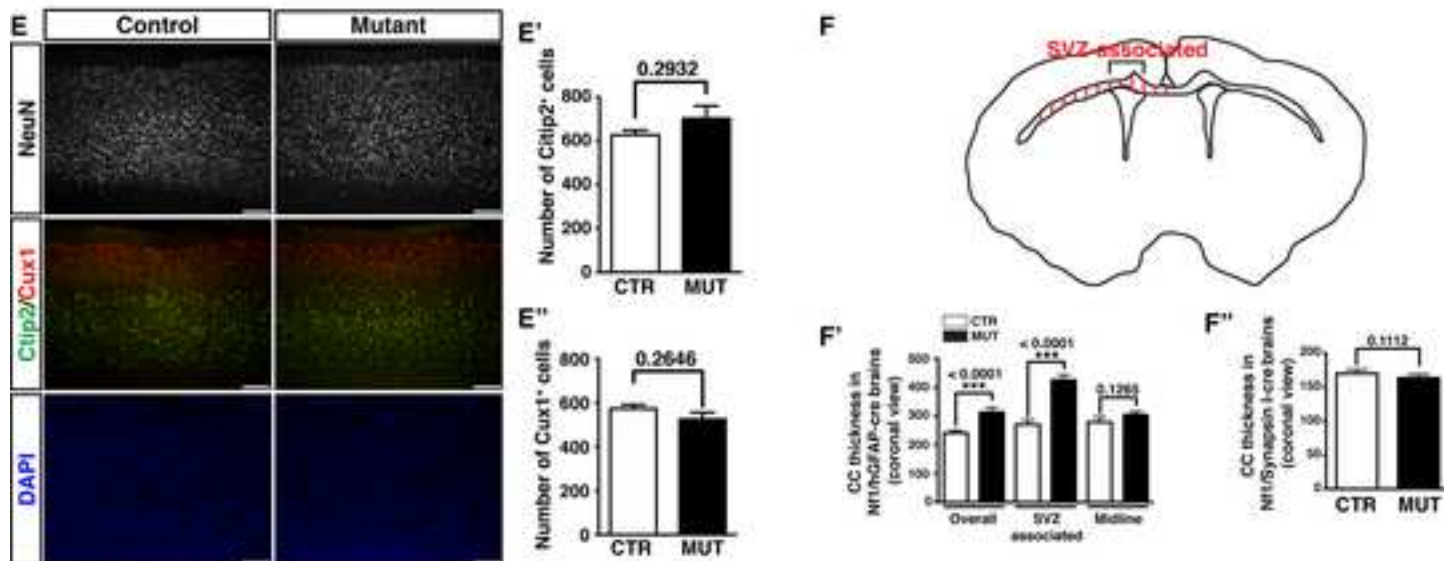
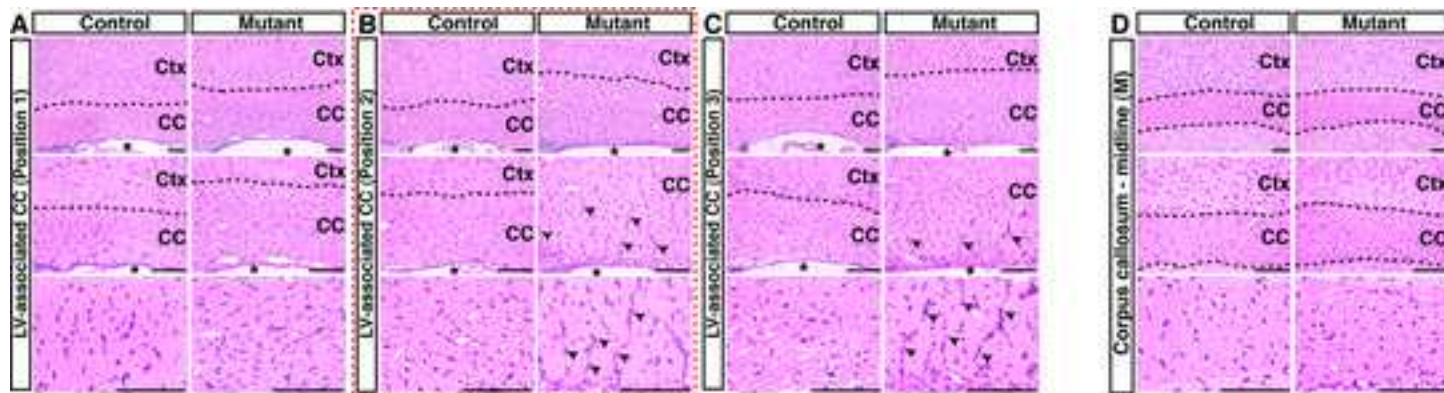
Lee da, Y., Yeh, T. H., Emnett, R. J., White, C. R., and Gutmann, D. H. (2010). Neurofibromatosis-1 regulates neuroglial progenitor proliferation and glial differentiation in a brain region-specific manner. *Genes & Development* *24*, 2317-2329.

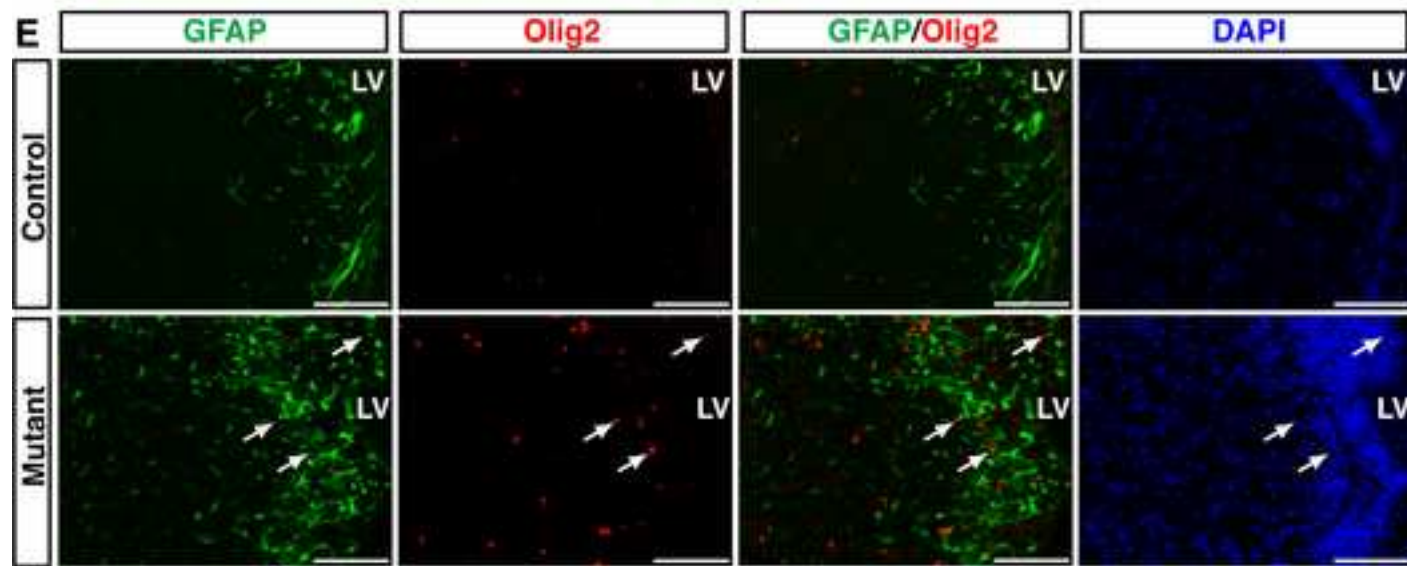
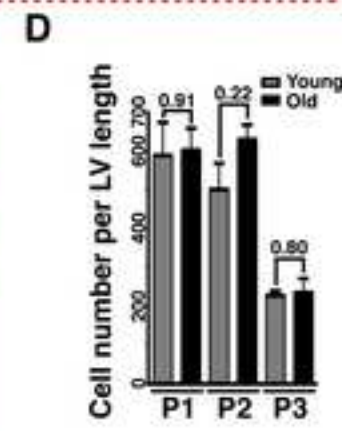
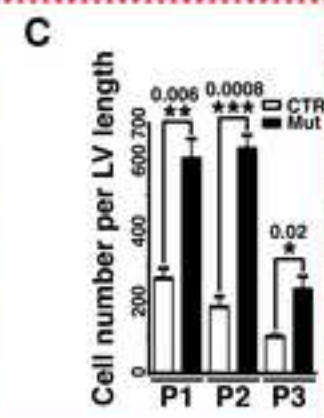
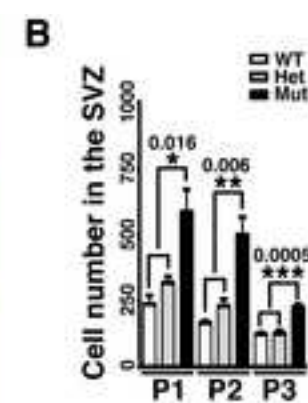
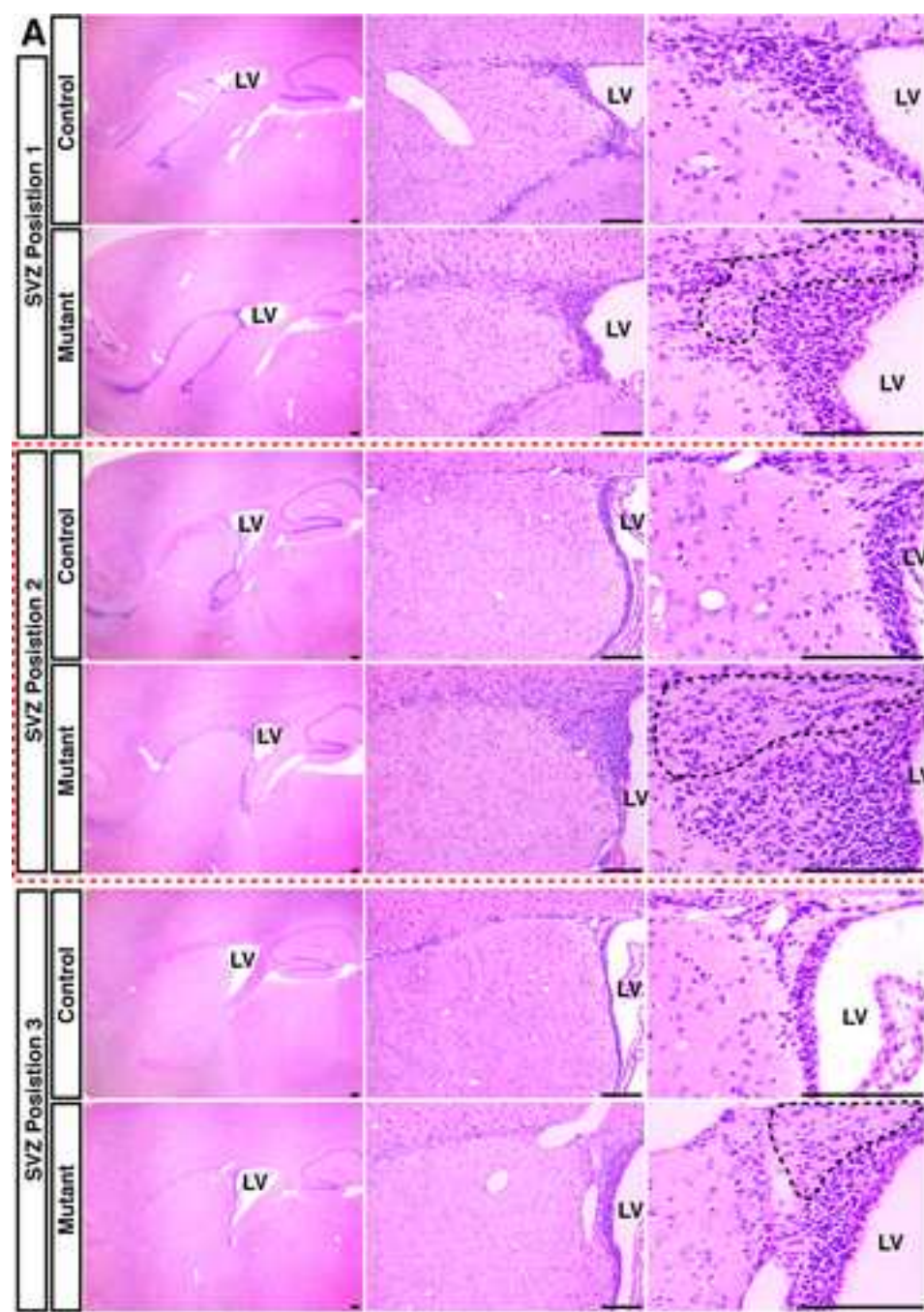
Molofsky, A. V., Pardal, R., Iwashita, T., Park, I. K., Clarke, M. F., and Morrison, S. J. (2003). Bmi-1 dependence distinguishes neural stem cell self-renewal from progenitor proliferation. *Nature* *425*, 962-967.

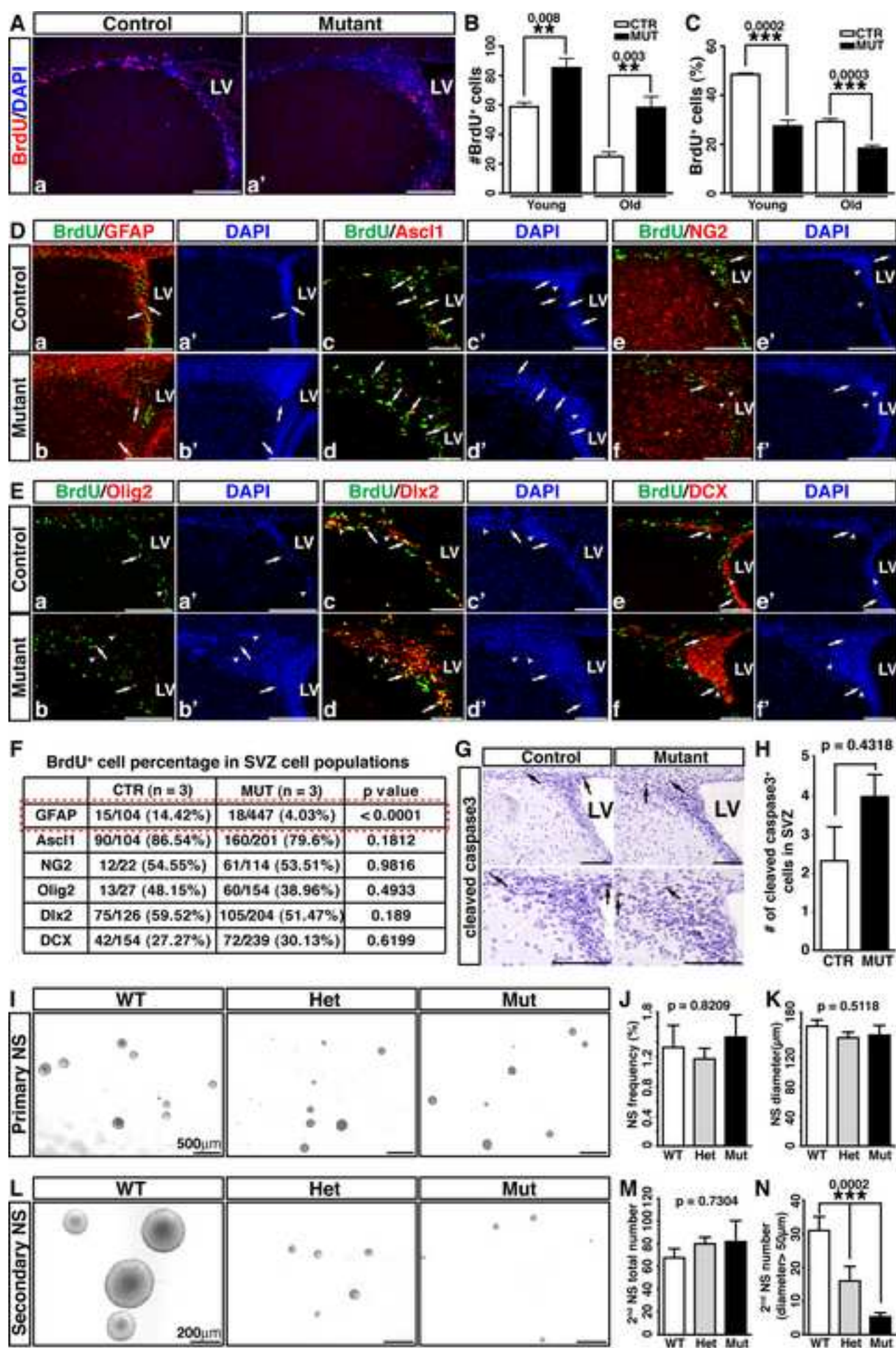
Wang, Y., Yang, J., Zheng, H., Tomasek, G. J., Zhang, P., McKeever, P. E., Lee, E. Y., and Zhu, Y. (2009). Expression of mutant p53 proteins implicates a lineage relationship between neural stem cells and malignant astrocytic glioma in a murine model. *Cancer Cell* *15*, 514-526.

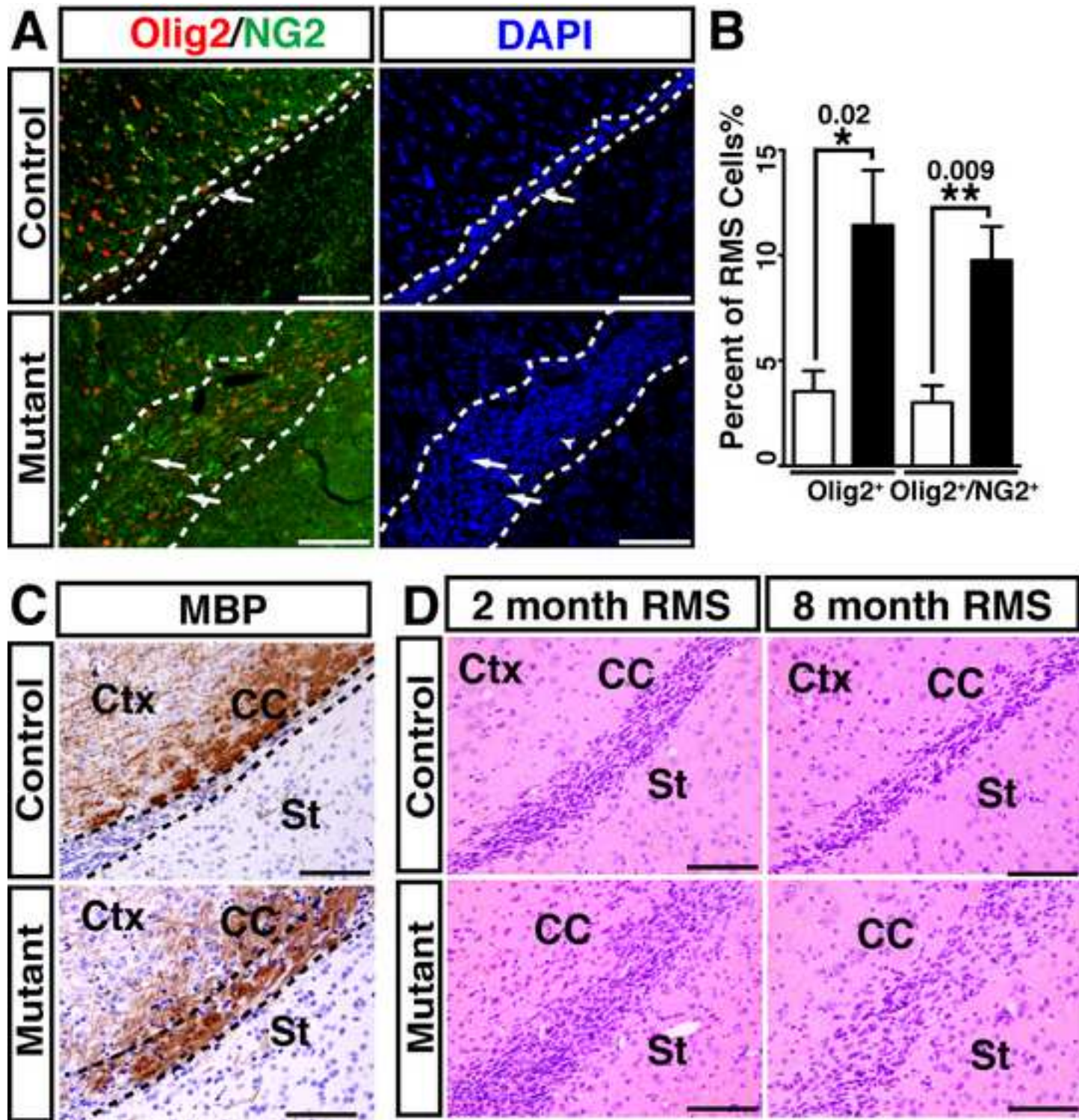
Zhu, Y., Richardson, J. A., Parada, L. F., and Graff, J. M. (1998). Smad3 mutant mice develop metastatic colorectal cancer. *Cell* *94*, 703-714.

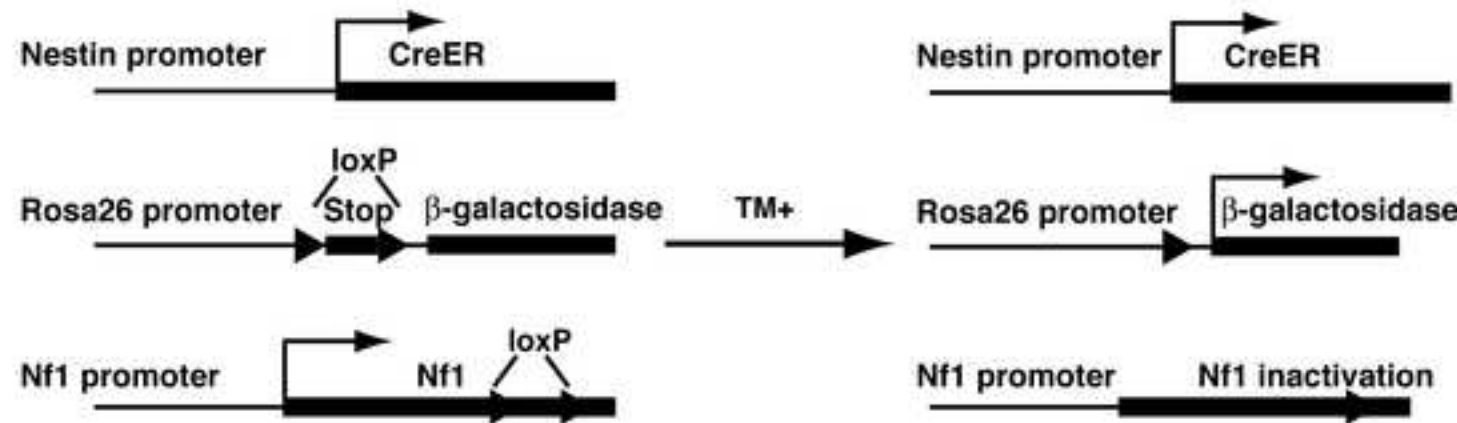
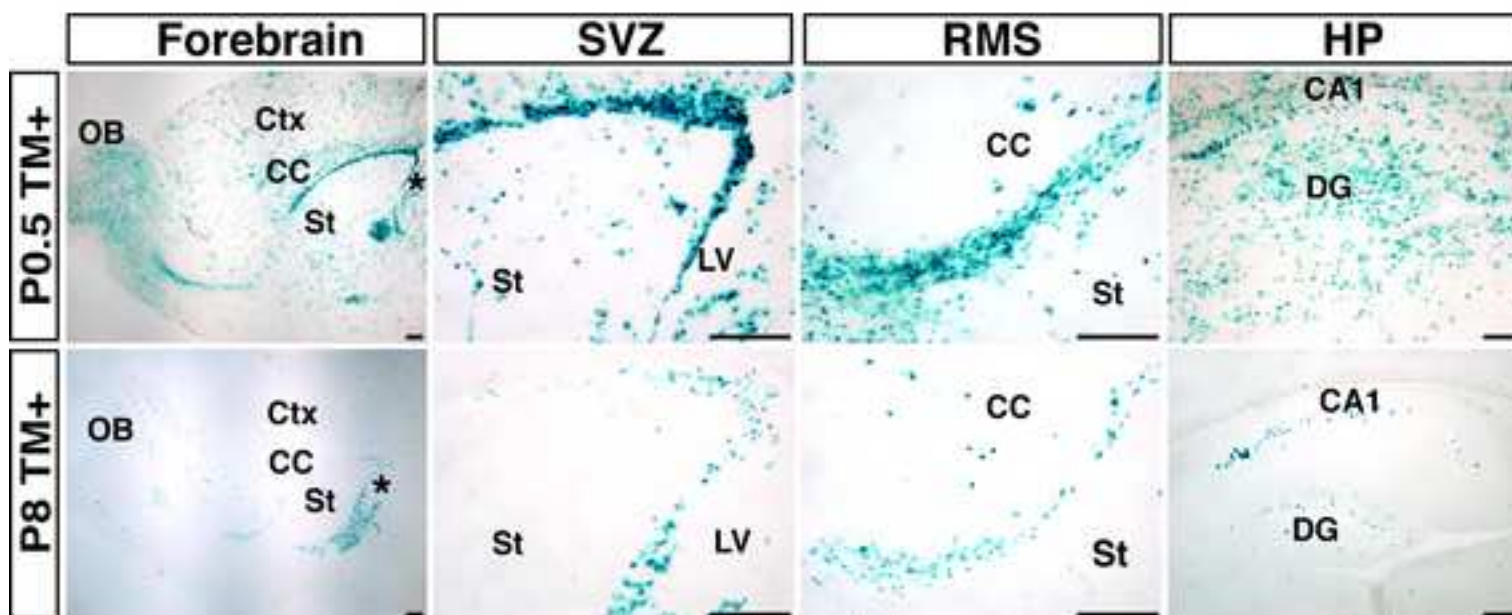
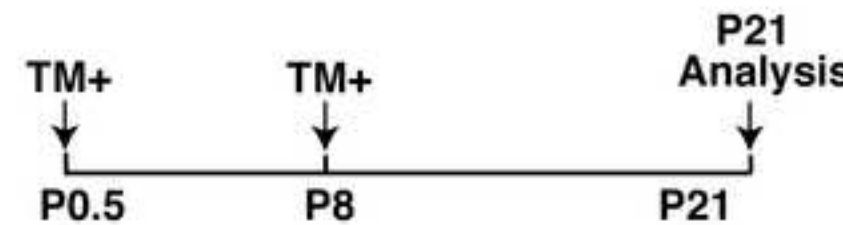
Zhu, Y., Romero, M. I., Ghosh, P., Ye, Z., Charnay, P., Rushing, E. J., Marth, J. D., and Parada, L. F. (2001). Ablation of NF1 function in neurons induces abnormal development of cerebral cortex and reactive gliosis in the brain. *Genes Dev* *15*, 859-876.

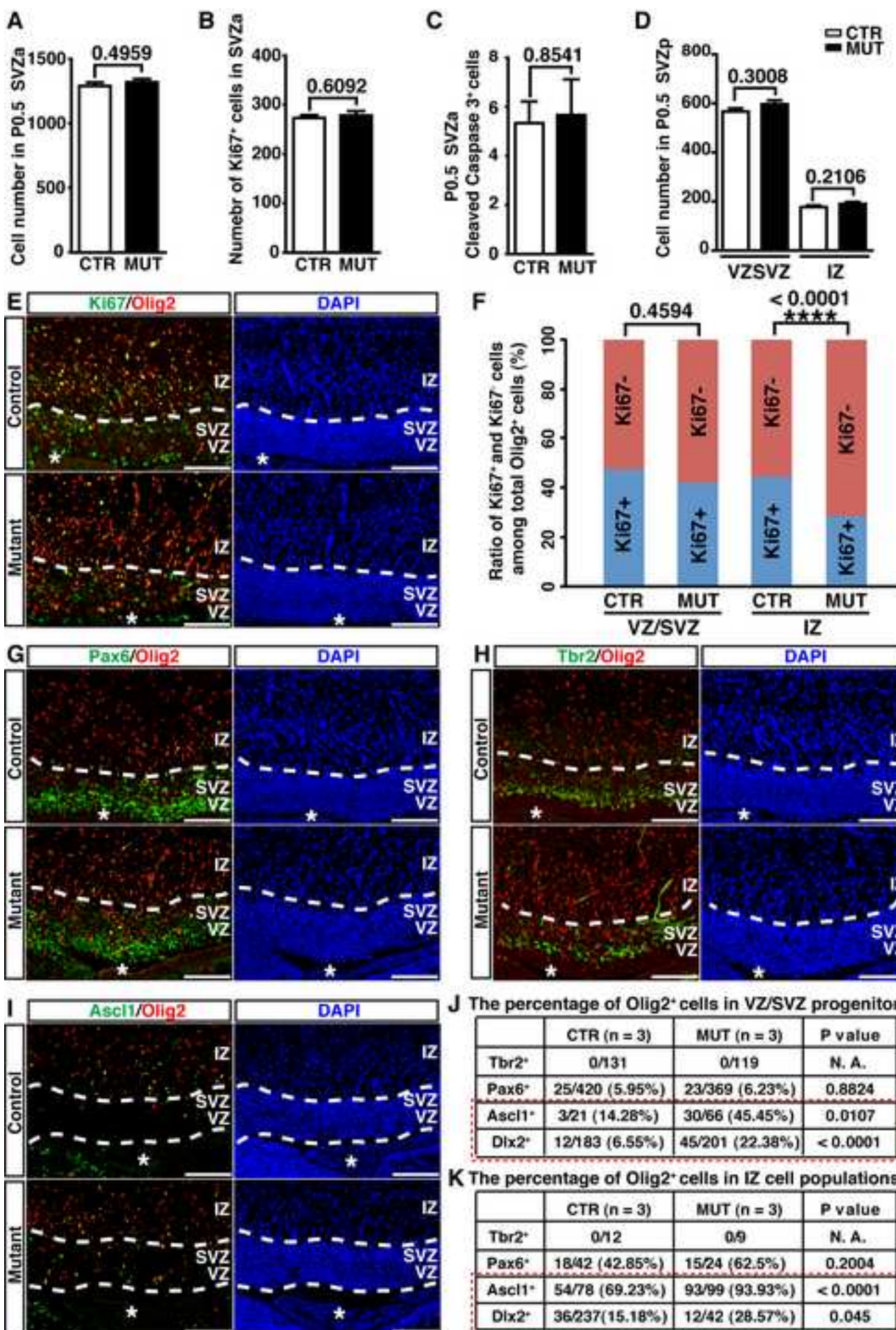
Supplemental Figure[Click here to download high resolution image](#)

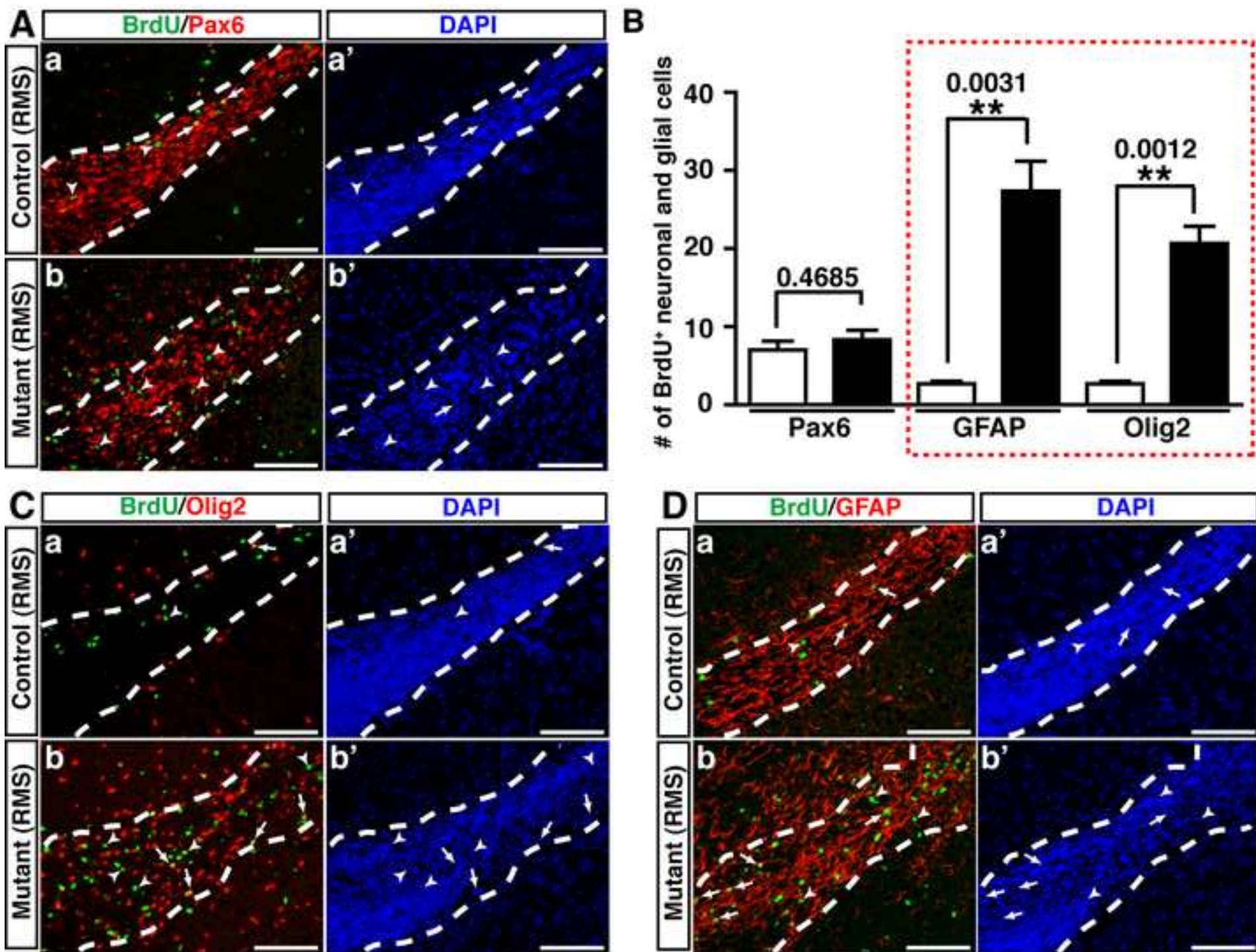






A**B**





Supplemental Figure[Click here to download high resolution image](#)